UNIVERSITY OF BIRMINGHAM

DEVELOPMENT AND OPTIMIZATION OF OPTICALLY PUMPED MAGNETOMETERS FOR BRAIN IMAGING

by

YULIA BEZSUDNOVA

A thesis submitted to the University of Birmingham for the degree of

DOCTOR OF PHILOSOPHY

Cold Atoms Research Group

School of Physics and Astronomy

College of Engineering and Physical Sciences

University of Birmingham

September 2023

Abstract

Portable and compact optically pumped magnetometers (OPMs) offer new research possibilities that are not achievable with conventional systems (SQUIDs) for brain recordings based on magnetoencephalography (MEG). The most compelling advantage of OPMs is that they can be placed directly onto the subject's head. This improves the accuracy and resolution of electrophysiological measurements, offering deeper insights into the human brain. While OPM-MEG systems are already commercially available, there is still scope for improvement. This thesis focuses on optimizing different aspects of OPM systems to enhance their performance for human MEG. First, we enhance the OPM sensor's noise resilience using nonlinear magneto-optical rotation. In the future, OPM sensors based on this principle can be combined with transcranial magnetic stimulation to study brain connectivity. Next, a mathematical model of the OPM-MEG system is developed to optimize sensor parameters, for example, vapour cell volume, to increase system sensitivity under specific environmental conditions. The model can serve as a guide to design OPM-MEG systems tailored to specific research needs. In the final part of this thesis, the foundation is laid for an experiment to test our hypothesis that the OPM-MEG system can offer significant advantages in experiments designed for multivariate pattern analysis (MVPA), a frequently employed technique in cognitive neuroscience. MVPA is based on comparing the spatial distribution of brain signals under different experimental conditions conditions and therefore holds a strong promise when applied to OPM-MEG data.

Acknowledgements

This work would not have been possible without the help and support of the incredible and inspiring people in my life. Despite global disasters and surreal circumstances, you were always there for me, and I am forever grateful.

First of all, I would like to thank my supervisors Ole Jensen and Giovanni Barontini. I couldn't have asked for better supervisors to learn the ropes of being a scientist in the messy world of academia. Thank you, Ole, for always being kind and supportive. You have shown me that being positive and enthusiastic helps not only yourself but everyone around. Your spirit and love for your work are very inspiring. Thank you, Giovanni, for your rigorous science and your ability to find clarity in our chaotic reports.

This work would never have happened without my unofficial supervisor Anna Kowalczyk. I am profoundly thankful to you for your guidance and friendship, and your help with everything from settling into the UK to sawing metal sheets in the lab. We have been side by side through the hardest and the happiest times together throughout this journey, thank you for being there.

I would like to extend my appreciation to the Centre for Human Brain Health team and all my lab colleagues and friends for their tremendous support, assistance, shared meals, movie nights, and outings at the pub. Additionally, a big thank you goes out to all the participants who contributed to my research.

I cannot express my gratitude for my family; my mom, my dad, and my sister as they have been my main support. Thank you for teaching me to be brave, persistent and joyful. Your belief in me and constant presence by my side mean the world to me. I have chosen a path that will keep me away from home but I miss you every day with all my heart.

I would like to say a big thank you to the people that I lived with throughout these years. Thank you again Ania for giving me a place for the first half year in the UK, and enormous thanks to Yali Pan who gave me a room during the lockdown and made it enjoyable with movie nights and Chinese cooking. I do not know what I would have done without you. Great thanks to Anna and Ulysses for opening up their home, which is truly the home of my dreams in every sense, your support and kind words were always timeless.

And finally, I would like to thank my future husband, Calum. Thank you for being my inspiration, for giving me my home, and for all the daily small things like getting me on the 20-minute walks not to grow one with the laptop.

Contents

List of Figures

List of Abbreviations

AEF Auditory Evoked Field.

AM Amplitude modulation.

AOM Acousto-optic modulator.

ATL Anterior temporal lobe.

AUC Area under the curve.

CAPE Cross-Axis Projection Error.

ECDs Equivalent current dipoles.

EEG Electroencephalography.

EOG Electrooculography.

ERF Event-related field.

FID Free-Induction Decay regime.

FM Amplitude modulation.

fMRI functional Magnetic Resonance Imaging.

HPI Head-position indicator coils.

ICA Independent component analyse.

MEG Magnetoencephalography.

MEMS Micro-Electromechanical systems.

MSR Magnetic Shielding Room.

MVPA Multivariate Pattern Analysis.

NMOR Nonlinear Magneto-Optical Rotation.

OP Optical pumping.

OPM Optically Pumped Magnetometer.

PLL Phase-locked loop.

PM Polarization-maintaining.

RMS Root mean square.

SERF Spin-Exchange Relaxation-Free regime.

SNR Signal-to-noise ratio.

SQUID Superconducting Quantum Interference Device.

SSP Signal-Space Projection.

SSS Signal-Space Separation.

TMS Transcranial Magnetic Stimulation.

List of Publications

- Kowalczyk, A. U., **Bezsudnova, Y.**, Jensen, O., & Barontini, G. (2021). Detection of human auditory evoked brain signals with a resilient nonlinear optically pumped magnetometer. NeuroImage, 226, 117497.
- Brickwedde, M., **Bezsudnova, Y.**, Kowalczyk, A., Jensen, O., & Zhigalov, A. (2022). Application of rapid invisible frequency tagging for brain computer interfaces. Journal of Neuroscience Methods, 382, 109726.
- **Bezsudnova, Y.**, Koponen, L. M., Barontini, G., Jensen, O., & Kowalczyk, A. U. (2022). Optimising the sensing volume of OPM sensors for MEG source reconstruction. NeuroImage, 264, 119747.
- **Bezsudnova Y.**, Jensen, O. (2023). Optimizing magnetometers arrays and pre-processing pipelines for multivariate pattern analysis. bioRxiv.
- **Bezsudnova Y.**, Quinn, A.J., Jensen, O. (2023). Spatiotemporal properties of common semantic categories for words and pictures. bioRxiv.

Chapter 1

Introduction

1.1 Advantages and challenges of OPM-MEG - an overview

Ionic currents flowing within the dendrites of neurons generate magnetic fields with an amplitude typically around 10^{-12} T at the scalp's surface. Until recently, arrays of superconducting quantum interference devices (SQUIDs) were the only sensors used to measure brain magnetic signals. SQUID-based magnetoencephalography (MEG) has millisecond temporal resolution and 3-5 mm spatial resolution [1] which makes it advantageous over other functional imaging modalities like electroencephalography (EEG) that suffer from low spatial resolution or functional magnetic resonance imaging (fMRI) that has low temporal resolution [2]. As a result, SQUID-MEG has emerged as an established noninvasive imaging tool in neuroscience [3]. However, conventional SQUID-MEG systems face certain practical drawbacks [4]. SQUIDs are superconducting coils containing Josephson junctions. A cryogenic dewar is necessary to support the operation of these sensors, which function at temperatures 4 K [5]. Therefore, a vacuum has to be maintained between the sensors and the subject scalp, for thermal insulation, resulting in sensors being at least 2-3 cm away from the scalp. Consequently, this separation leads to an average five-fold reduction in the measured signal strength compared to an on-scalp sensors placement [6–8]. It's important to consider that the Earth's magnetic field ($\approx$ 5x10^{-5} T) is significantly stronger than the brain signal. As such, any loss in the amplitude of the brain signal due to this distance

makes its measurement considerably more challenging. Furthermore, the sensors are typically mounted within a standard-sized helmet-shaped device at fixed positions. As a result of this rigid design, the system allows scanning a limited range of subjects without compromising data collection accuracy, for instance, the standard helmet does not accommodate smaller head sizes, such as children's. During the experiment, the subject has to sit still without moving their head, which can be uncomfortable and unnatural for extended periods of time. Finally, the system's reliance on cryogenics makes MEG systems expensive to purchase and maintain, requiring either a supply of liquid helium or a local helium liquefier.

The publication [9] in 2006 marked the advent of optically pumped magnetometers (OPM) in the field of magnetoencephalography, presenting the pioneering use of these new sensors for brain recordings. OPMs measure changes in the magnetic field by measuring alterations in laser light properties (intensity or polarization) as it passes through an alkali atom gas, where synchronized precession of magnetic moments of electrons, atoms, or atomic nuclei is induced. The sensor output is a product of the magnetic field intensity multiplied by atomic constants. At this stage, OPM sensors offer similar or slightly lower sensitivity (7-10 $\mathrm{fT}/\sqrt{\mathrm{Hz}}$) compared to SQUID-MEG systems (2-5 $\mathrm{fT}/\sqrt{\mathrm{Hz}}$) [4, 10], however, in theory, their sensitivity can reach levels lower than 1 $\mathrm{fT}/\sqrt{\mathrm{Hz}}$ [11]. During the late 2000s, it was recognized that OPMs had the potential to overcome several limitations of conventional MEG systems. Although the initial OPMs were relatively large (tens of centimetres), extensive work on improving sensor design was done in the 2010s, leading to the development of a system with microfabricated sensors $\approx 1\ \mathrm{cm}^3$ in size [12]. Now, a decade later, there are ongoing studies focused on making the OPM-MEG a standard tool for cognitive neuroscience research and integrating it into clinical settings.

Compact OPM sensors have gathered significant attention and interest in the MEG community primarily because they can be fixed directly on the subject's scalp. Simulations demonstrate that using an array of OPM sensors on the scalp yields a 4-5 times stronger signal from cortical areas compared to the SQUID system, and approximately 2 times stronger signal from deeper regions [7, 8]. Moreover, by optimizing the placement of sensors according to an individual's

head shape and experimental needs, it is possible to achieve better brain coverage and, hence more precise data collection. The use of low noise on-scalp dense sensor array potentially leads to enhanced spatial sensitivity and improved source reconstruction accuracy [10, 13–15]. Notably, a recent study [10] demonstrated the theoretical ability of a dense OPM array to resolve multiple independent sources to a degree currently achievable only using an invasive technique such as electrocorticography. Additionally, OPMs can be designed as a scalar magnetometer measuring the absolute amplitude of magnetic field or vector magnetometers, enabling separate measurements of magnetic field components in three directions using a single sensor (tri-axial) [16, 17]. In contrast to SQUID systems that do not capture these field projections, the utilization of tri-axial OPMs offers new insights, enhancing cortical coverage [18]. In general, an improvement in spatial resolution offered by OPMs is a significant advancement in the field of brain imaging.

Another advantage that comes from the compact and mobile design of OPM sensors is that OPM-MEG can accommodate helmets of various sizes suitable for infants, young individuals, as well as adults [4, 19]. Helmets with slots for OPM sensors customized using MRI scan perfectly fit individual head shapes [20]. Therefore, an OPM-MEG system is a cost-effective option for conducting longitudinal studies on brain development, as it only requires replacing the helmet as an individual grows. Moreover, OPM-MEG, a wearable system with sensors attached to the head, offers participants the freedom to move during experiments. This exciting feature paves the way for research opportunities using naturalistic tasks, where participants can walk, or at the very least, move their heads [21, 22]. In addition, OPMs can be assembled to study biomagnetic activity not only in the human brain but also in animal brains or body parts such as the retina, foot muscle, or spine [23–27]. It is worth noting that certain types of OPMs offer reliable brain signal measurements in a wide frequency range, spanning from DC fields to 2 kHz, making them comparable to conventional SQUID systems in this aspect [28, 29]. Lastly, the new system can be in theory combined with transcranial magnetic stimulation (TMS). The integration of TMS with OPM-MEG will enable direct investigation of brain connectivity by stimulating a specific region of the brain and measuring the resulting response in another region.

This multimodal approach in the future will enhance our understanding of brain dynamics and facilitate comprehensive brain function and connectivity studies.

In conclusion, OPM-MEG provides a wearable, high spatial and temporal resolution, fT-sensitive, and multimodal neuroimaging platform that enables noninvasive and dynamic exploration of brain activity. Due to its relatively low cost and reduced running and maintenance expenses, the OPM-MEG system has the potential to be a more accessible and practical option for widespread use compared to current MEG systems.

So far I outlined the advantages that OPM-MEG theoretically presents for brain imaging. However, being nascent technology not all of them are realized by the time of writing this thesis. While OPM sensors have demonstrated an increase in the amplitude of measured brain signals, their noise floor (7-10 $\mathrm{fT}/\sqrt{\mathrm{Hz}}$) remains higher than that of the SQUID-MEG system (2-5 $\mathrm{fT}/\sqrt{\mathrm{Hz}}$) [30], resulting in a comparable signal-to-noise ratio (SNR) for both systems [4, 10]. For example, the amplitude of audio evoked field (M100) in [31] measured by 15 dual-axis OPMs is around 500 fT, whereas measured by SQUID-MEG system is around 100 fT. However, the average value of SNR for all subjects was for the OPM-MEG system 11.1 dB, and for the SQUID-MEG system 13.8 dB. Noisy OPM measurements lead to similar spatial resolution between two systems [32]. In practice, both hardware and software for OPM-MEG should be improved and optimized in order to take advantage of all that the OPM-MEG system can offer.

The work presented in this thesis focuses on optimizing various aspects of the OPM-MEG system. To provide a comprehensive overview, I will now summarize the key areas where ongoing research efforts are aimed at integrating the findings of this thesis into a broader context.

The main challenge lies in reducing the noise floor in the OPM-MEG system. This task consists of three parts: to reduce the noise of the individual sensor, to eliminate the cross-talk when sensors are arranged in an array, i.e. the distortion of measurement at one sensor due to the presence of another sensor, and, lastly, to compensate for artefacts from ambient magnetic field fluctuations [4, 33]. The first part is a purely technical exercise that involves optimizing sensor parameters like the vapour cell shape and size, atomic density number, prolonging the interaction

between laser light and atoms (multipass cells) [34], etc., which is discussed in Chapter 4 of this thesis. It also involves building or using the electronics like lock-in amplifier, and current drivers for the nulling coils as noiseless as possible [35, 36]. The second engineering challenge in OPM-MEG systems is the issue of crosstalk when neighbouring sensors are offsetting each other and perturbing each other sensing axis. Self-shielded zeroing coils employed in commercial sensors have significantly reduced cross-talk from 8% to 0.5%, however, there is still potential for further improvement with the more precise alignment of coils [37]. Finally, the issue with the ambient field can be can be tackled through multiple approaches. One solution involves incorporating an array of reference sensors or synthetic gradiometers, both of which require sophisticated data processing techniques [35, 38]. Alternatively, the development of sensors (magnetometers or intrinsic gradiometer) designed to withstand background fields is underway in certain research labs [39–43]. Chapter 3 of this thesis is dedicated to the design of such resilient sensors published in [44].

Another challenge of the OPM sensors design lies in improving their dynamic range, i.e. the range of magnetic fields that OPMs can tolerate [11, 45, 46]. Even 4 years ago the magnetic field fluctuations in the order of 1.5 nT could render commercial OPMs inoperable due to their limited dynamic range [47]. To address this issue, a closed feedback loop operation mode was introduced to increase the dynamic range from 1 nT to 10 nT [48]. Nevertheless, these sensors cannot be combined with other brain imaging modalities. This is still an extremely low magnetic field compared to Earth magnetic field, therefore the "OPM-optimized" magnetic shielding rooms (MSR) were designed to create an environment where the allowed dynamic range will not be exceeded [49]. Utilizing active shielding with magnetic source reconstruction [50, 51] is an alternative approach to address the dynamic range issue without directly enhancing the dynamic range of the sensors themselves.

Although the shielded room and closed loop system provide significant noise reduction, external interference cannot be completely removed by the hardware solutions. The OPM-MEG signal still contains various artefacts that require correction including low-frequency movement artefacts (<6 Hz), urban traffic noise, vibrations (0-40 Hz), line noise (50 Hz), and high-

frequency interference from equipment inside the shielded room (120 Hz) [4, 10, 36]. Recently a lot of attention has been allocated to designing signal processing strategies aimed at reducing noise in MSR [35, 52, 53]. The majority of algorithms use models of the ambient field in MSR along with a co-registration system to accurately locate all the sensors to remove the background field from the data via regression or other generalized linear approaches [54–56]. The summary of algorithms reducing interference can be found in [35]. Co-registration system to localize the sensors presents a technical challenge it has to be accurate while also ensuring a relatively fast processing time to avoid prolonging the duration of the experiment. The simulation shows that errors in sensor orientation $5° - 15°$ results in 4.8-14.7% errors in reconstructed topography, i.e. $l2$-norm of difference in the fields generated by each source at the location of each sensor in an unperturbed array and a mis-coregistered array [10, 57, 58]. Algorithms to reduce background magnetic interference in the recorded data are a highly complex modeling task, and thus there is a significant demand for further research and development in this area. For example, signal space separation algorithms that separate magnetic signals originating inside and outside the helmet, which are discussed in Chapter 5 in detail and commonly used to denoise SQUID-MEG data are also being explored for OPM-MEG. However, due to the smaller sensor count and, therefore, the lack of spatial oversampling, further development is required to adapt these algorithms effectively for OPM-MEG.

Another issue that arises from ambient field time fluctuation is cross-axis projection error (CAPE) where small remnant static magnetic fields along perpendicular directions to the sensing axis, not violating the dynamic range criteria, can introduce significant error terms in OPM's output signal [48, 59]. CAPE also manifests itself when OPM is being tilled or moved due to the spatially varying remnant fields inside an MSR. A recent approach to addressing this issue involves the implementation of dynamic nulling coils in all three directions using a reference array. While this method eliminates CAPE, it introduces extra noise to the system [48].

The issue of spatially varying remnant fields inside MSR becomes crucial when designing a mobile OPM-MEG system where participants can freely move. For example, $4°$ rotation in a 30 nT field would be sufficient to prevent the OPM from working. Specially created biplanar coils

were constructed to maintain a homogeneous remnant field of approximately 200 pT within a defined space of 0.4 m^3 [50, 60], allowing participants to move inside this region without introducing significant artefacts in the data. This type of dynamic active shielding has enabled studies like human writing or participants playing ping-pong while recording brain signals [60, 61]. In addition to active shielding the interference algorithms tailored to experiments with movement are required to get meaningful data [53, 62]. Consequently, challenges related to motion capture systems and detailed field mapping inside the MSR arise as well [21, 55, 63]. Moreover, the development of real-time correction methods without using dynamic shielding, as demonstrated in [55], shows promise for OPM-MEG systems with improved motion tolerance and reduced reliance on passive shielding, which will make OPM-MEG even more logistically accessible.

The new OPM-MEG system is facing similar challenges and questions that were addressed during the development of SQUID MEG [64, 65]. Chapters 4 and 5 of this thesis delve into some of these questions, specifically focusing on the number of sensors needed for a good performance. The optimal sensor arrangement in OPM-MEG systems is still open discussion [66], although studies have demonstrated that rigid helmets outperform flexible ones [32]. There are a lot of studies modelling the new system to find optimal sensor arrangement, however, there is not yet a unified solution. Furthermore, existing data processing algorithms, such as beamforming analysis or multivariate pattern analysis, need to be adapted and optimized to suit on-scalp OPM-MEG for functional neuroimaging [52, 58, 67]. This is because the measurement techniques employed by SQUID and current OPM systems differ, with SQUIDs mostly utilizing gradiometers and OPMs utilizing magnetometers. Chapter 5 provides a more comprehensive exploration and analysis of this issue.

In summary, OPM-MEG represents a promising emerging technology that offers neuroscientists a unique noninvasive means of observing brain activity. Even at present, OPM-MEG exhibits significant advantages over existing techniques, and although technical challenges persist, there seem to be no fundamental barriers to further advancements and improvements in the field.

1.2 Thesis outline

The original purpose of this thesis was experimental work to design OPM sensors compatible with TMS, because of COVID-19 pandemic and almost a year of no experimental work, the focus shifted towards optimizing different aspects of the OPM-MEG system. Here I will outline each chapter. A substantial portion of this thesis contains material that has been published in academic journals, presented at conferences, or posted on preprint servers. The text of these works has, on occasion, been adjusted to provide the thesis with a coherent narrative.

The structure of the thesis is as follows:

Chapter 2: General principles of optically-pumped magnetometers

This chapter introduces the theory underlying the operational principles of different types of optically pumped magnetometers (OPMs): those based on the spin-exchange relaxation-free regime (SERF-OPM), nonlinear magneto-optical rotation (NMOR-OPM), free-induction decay regime (FID-OPM), and OPMs utilizing ^{4}He. The chapter highlights the respective strengths and limitations of sensor designs in the context of their application for magnetoencephalography.

Chapter 3: Development of NMOR OPM sensor for MEG experiment

The review in the introduction (Chapter 1) emphasizes the need to improve OPM sensors intrinsic dynamic range and noise resilience. The chapter details the experimental work of developing and utilizing NMOR-OPM that is resilient to ambient magnetic fields. We demonstrate the detection of auditory evoked fields in an environment with a background magnetic field of 70 nT. Results from this chapter are published in **"Detection of human auditory evoked brain signals with a resilient nonlinear optically pumped magnetometer." by Kowalczyk A. U., Bezsudnova Y., Jensen O., and Barontini G.** [44]. The experimental work and the data collection and analysis were done by Anna U. Kowalczyk and myself under the supervision of Giovanni Barontini and Ole Jensen.

Chapter 4: Model to optimize OPM-MEG system design for MEG applications

The literature review in the introduction (Chapter 1) indicates the lack of sensor design optimization for MEG applications. Chapter 4 is dedicated to the development of a modelling toolkit, accessible at the GitHub repository "OPM-model", aimed at optimizing sensor designs taking into account environmental noise conditions. The primary objective was to find the optimal sensing volume of NMOR and SERF OPM sensors for different levels of environmental noise in order to design vapour cells for the next generation of sensors. The result of this work is published in **"Optimising the sensing volume of OPM sensors for MEG source reconstruction" by Bezsudnova Y., Koponen L. M., Barontini G., Jensen O., and Kowalczyk A. U.** [8] and presented by myself at multiple conferences (MEGUK2021, WOPM2021, WOPM2022 [68], BIOMAG2022). Mathematical model design, programming, data analysis, and writing were done by myself with the assistance provided by Lari M. Koponen and under the supervision of Anna U. Kowalczyk, Giovanni Barontini, and Ole Jensen.

Chapter 5: Design considerations for an array of magnetometers optimized for MVPA

The next two chapters lay the foundation for an experiment to test the hypothesis that OPM-MEG systems can offer significant advantages in experiments designed for multivariate pattern analysis, a frequently employed technique in cognitive neuroscience.

This chapter discusses the design considerations for an array of magnetometers (in future OPM-MEG) when utilized in the aforementioned experiments. In particular, the chapter addresses appropriate noise reduction techniques for magnetometers and determining the optimal number of sensors for effective multivariate pattern analysis (MVPA). The results of this study were presented as a poster at the WOPM2023 conference and have been submitted for publication in the Journal of Neuroscience Methods **"Optimizing magnetometers arrays and pre-processing pipelines for multivariate pattern analysis" by Bezsudnova Y. and Jensen O.** (published on bioRxiv) [69] Data collection, analysis, and writing were done by myself under Ole Jensen supervision.

Chapter 6: Semantic representations for words and pictures studied with SQUID-MEG

Chapter 6 presents the findings of a neuroscience experiment conducted using a conventional SQUID MEG system, aimed at investigating semantic representation from different modality stimuli (written words and pictures) using multivariate pattern analysis. The MEG study results were presented at the conference CCN2023 and have been submitted for publication in the Journal of Cognitive Neuroscience **"Spatiotemporal properties of common semantic categories for words and pictures" by Bezsudnova Y., Quinn A.J., and Jensen O.** (published on bioRxiv) [70] The Method development, data collection, data analysis, and interpretation are done by myself under Ole Jensen supervision. Andrew Quinn provided helped with the statistical analysis.

Chapter 7: Conclusion and future research

Chapter 7 brings together the insights gained from all the previous chapters, summarizing what was learned and pointing out what are future research possibilities.

Chapter 2

General principles of optically-pumped magnetometers

Optically pumped magnetometers (OPMs) rely on the Larmor spin precession of optically polarized paramagnetic atoms in the magnetic field to be measured. A general schematic of an optical atomic magnetometer is shown in Fig 2.1. Three main processes take place in an atomic magnetometer simultaneously, however, for simplicity, I will describe them as though they happened in three sequential steps. First, the process of optical pumping is employed. The light source denoted as a pump is used to create a population difference between Zeeman sublevels, which leads to the alignment of atomic spins or polarization of the atoms. This alignment then evolves in the presence of an external field to be measured. Finally, the resulting atomic alignment is measured by observing its impact on a second light beam known as the probe [11, 71]. Various atomic magnetometer setups are available. For example, one configuration can have two separate beams as pump and probe beams or another involves combining the pump and probe beams into a single beam. The detection can be based on either the absorption of probe light or changes in its polarization [72].

In this chapter, I will introduce the theoretical framework and concepts required to describe the working principle of OPM based on nonlinear magneto-optical rotation (NMOR), i.e. light-intensity-dependent rotation of a polarization plane of linearly polarized light upon its

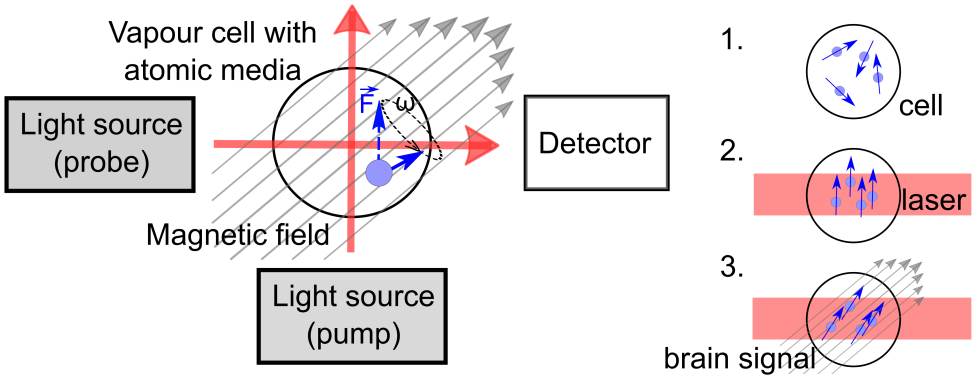

Figure 2.1: A general scheme of an optically pumped magnetometer. The pump light generates an aligned state (2), and the atomic polarization evolves in response to an external magnetic field with Larmor frequency ω (3). The resulting state is detected by observing the altered properties of the probe light.

propagation through a medium placed in a magnetic field [73].

The chapter begins with a basic overview of the atomic energy structure before describing techniques for polarizing alkali atoms and measuring their alignment direction. Then the effects that limit the spin-polarization coherence lifetime are discussed. Furthermore, the fundamental limit of magnetometer sensitivity is explained. Finally, different types of optically pumped magnetometers are presented and their characteristics are discussed.

Prior to delving into these topics, I will clarify the terminology used and outline the approach I will employ to present complex concepts effectively.

Each atomic energy level corresponds to a given projection of an atomic angular momentum. The overall energy state (superposition of population of all the energy levels) of the atom is related to a specific spatial orientation of its angular momentum [74, 75]. Atomic alignment of a media or, in other words, its polarization occurs when the angular momentum of the atoms is not distributed isotropically (optical anisotropy of the media) [76]. This atomic alignment can be described in terms of atoms angular momentum and density matrix or in terms of their spins and polarization of the media. Instead of a numerical expression of the density matrix [77], I will use its pictorial presentation used in [73, 78, 79] to illustrate the dynamics of the light-atom interaction that is used to create atomic alignment. The mathematical description

can be found in [73, 80–82]. In this representation, the distance, r, of a specific point on the surface corresponds to the probability of finding the maximum projection of the density matrix in that direction. To visualize the entire surface in three-dimensional space, the density matrix is rotated to align the quantization axis with a specific direction. Then, the state is projected onto this direction to create the surface plot.

$$r(\theta, \alpha) = R^{-1}(\alpha, \theta, 0)\rho R(\alpha, \theta, 0) \mid_{FF}, \tag{2.1}$$

where $|_{FF}$ is the projection with the highest m and $R(\alpha, \theta, 0)$, where m is the magnetic quantum number and $R(\alpha, \theta, 0)$ is the quantum mechanical rotation operator in spherical coordinates, θ is the azimuthal angle and α the polar angle.

For example, an unpolarized atom with all ground state sublevels equally populated is represented by centred around the origin sphere.

2.1 Theory of NMOR

2.1.1 Atomic Energy Levels

The core component of any OPM sensor is the vapour cell that contains an atomic gas with a specific three-level atomic energy structure called Λ system (Fig 2.2 A) [73]. Alkali metal atoms such as Cesium (Cs), Rubidium (Rb) and Helium (He) have approximated Λ system in their energy structure [83]. Since the sensors presented in Chapter 3 utilizes the ^{87}Rb D1 transition, all the relevant numerical values will be provided specifically for this atom.

The energy structure of ^{87}Rb is shown in (Fig 2.2 B) [84]. Λ system is based on D1 transition $5S_{1/2}$ $F = 2$ (ground state) $\rightarrow$ $5P_{1/2}$ $F = 1$ (excited state) of a hyperfine structure, where F denoted total angular momenta of a state. In the presence of an external magnetic field two split Zeeman levels of ground state $m_F = -1, 1$ denoted as $|+\rangle$ and $|-\rangle$ and excited state form required Λ system [85]. m_F is the magnetic quantum number determining projections of the angular momenta on a quantization axis. Note that without a magnetic field, all Zeeman levels

have the same ground state energy level (degenerated levels).

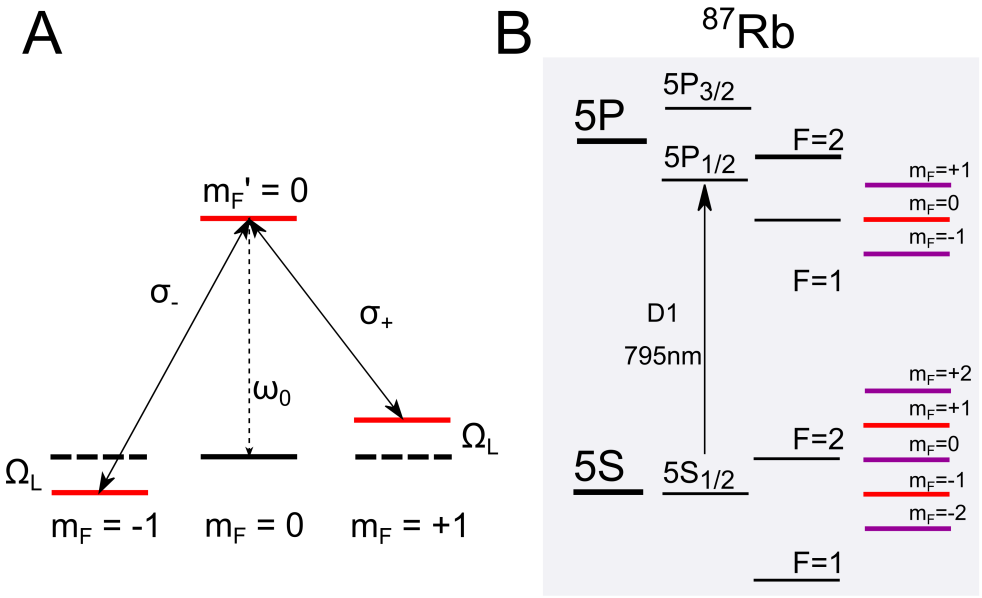

Figure 2.2: A: Two-level atomic system interacting with linearly polarized light. A nonzero magnetic field oriented along the quantization axis splits magnetic sublevels in the ground state by Ω_L. In this case, each circular component of the linearly polarized light undergoes different dispersion in a medium, which results in rotation of the polarization plane. B: Energy-level structure ^{87}Rb D1 line (not to scale). Energy levels forming the Λ structure involved in NMOR OPM are highlighted in red, and the energy levels involved in the relaxation are shown in purple.

2.1.2 Optical pumping

Optical pumping (OP) is the process by which angular momentum is transferred from light to the atoms [76, 77, 86, 87]. In NMOR configuration linearly polarized light is used to pump the atoms to an aligned state [88–90].

Let's consider y-polarized light tuned to D1-transition (λ = 795 nm). Linearly polarized light can be presented as a sum of left σ^- and right σ^+ circular polarized lights. Due to quantum selective rules σ^- component will excite election from $m_F = -1$ to $m_F^{'} = 0$, while σ^+ component will excite election from $m_F = 1$ to $m_F^{'} = 0$. Consequently, a linearly polarized light creates quantum coherences (a superposition of two states) between Zeeman sublevels $|+\rangle$ and $|-\rangle$. The light-induced state can be written as [88]

$$|y\rangle = -\frac{i}{\sqrt{2}}(\,|+\rangle - |-\rangle)\,, \tag{2.2}$$

The superposition $|y\rangle$ is related to an atomic alignment. The OP process is illustrated in Fig 2.3 A. Before the OP starts, the atoms are in a state of thermodynamic equilibrium, wherein the sublevels of the ground state exhibit equal population (sphere). Light-atom interaction results in redistribution of the atomic population, which results in a peanut-like shape representing Zeeman coherence.

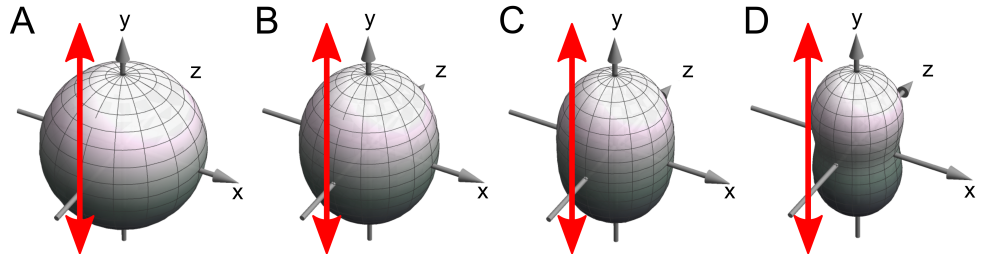

Figure 2.3: Schematic visualization of pumping of an atomic alignment with linearly polarized light. The initially unpolarized sample (A) interacts with linearly polarized light, leading to the redistribution of atomic populations and the creation of Zeeman coherence. Subsequent stages of the pumping process are illustrated in (B), (C), and (D). The final stage is represented by a peanut-like shape corresponding to the state $|y\rangle$. The long axis is related to the axis of the optical anisotropy induced in the medium. The visualization was done using a package written for Mathematica to facilitate density-matrix calculations [80]. The red array shows the direction of polarization.

2.1.3 Evolution stage and detection stage

When external magnetic field B_{ext} introduced the evolution of the state $|y\rangle$ is given by [73, 90]

$$|\phi(t)\rangle = -\frac{i}{\sqrt{2}}(\,|+\rangle e^{i\Omega_L t} - |-\rangle e^{-i\Omega_L t})\,, \tag{2.3}$$

where $|\phi(t)\rangle$ is the quantum state of the system, Ω_L is Larmor frequency. From Eq. 2.4 it is seen that the initial state $|y\rangle$ rotates with Larmor frequency in the presence of the external magnetic field. In other words, atomic alignment starts pressing with Ω_L along the axis determined by the magnetic field (Fig 2.4). Note that $|\phi(\varphi + \pi/\Omega_L)\rangle = |\phi(\varphi)\rangle$, therefore each half of the Larmor

period, the quantum state of the system replicates itself.

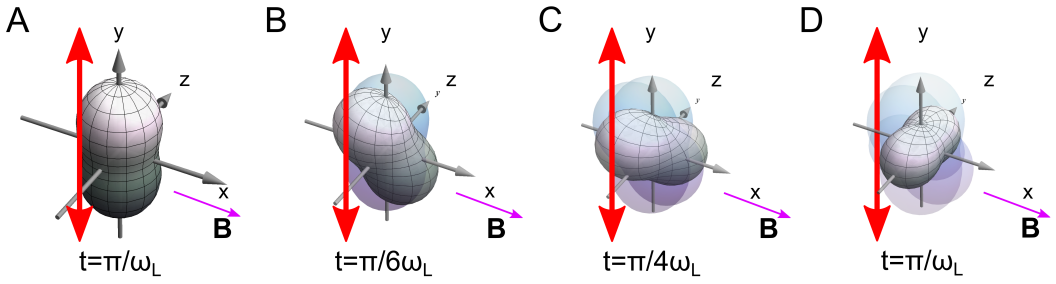

Figure 2.4: Schematic visualization of the time evolution of the medium under interaction with continuous light. Pumping, rotation, and relaxation of the atomic alignment are three processes which take place simultaneously. Rotation from the previous pumping + relaxation is shown as blue fade imprints. The visualization was done using a package written for Mathematica to facilitate density-matrix calculations [80]. The red array indicates the direction of polarization, while the purple arrow represents the direction of the external magnetic field.

Optical rotation known as the Macaluso-Corbino effect is employed to measure the external magnetic field [91]. The external magnetic field is determined through Larmor frequency, extracted from the probe light's polarization plane rotation.

$$B_{ext} = \frac{1}{\gamma}\Omega_L, \tag{2.4}$$

where $\gamma = g_e\mu_B/\hbar$ is a gyromagnetic ratio - the ratio of particle or system's magnetic moment to its angular momentum, g_e is Lande factor, μ_B is the Bohr magneton. $\hbar$ is reduced Planck constant.

The overall phenomena described here in stages in sections 2.1.2, 2.1.3 is referred to as NMOR because it is an effect that media that is altered by an external magnetic field has on polarized light propagating through it [73, 90, 92, 93]. Nonlinearity comes from that effect being dependent on the intensity of pumping light [94, 95].

2.1.4 Zero-field resonance and high-field resonances

While the above discussion is conceptually accurate, the effect of continuous optical pumping and relaxation processes is left out. Continuous pumping constantly turns the atomic alignment

from rotating to the initial state $|y\rangle$. The relaxation process such as repopulation of the ground states or Zeeman coherence relaxation reduces the number of atoms aligned. The combined effects of rotation, continuous pumping, and relaxation result in the generation of a net anisotropy within the medium shown as the fade imprints in Fig 2.4. However, this equilibrium anisotropy appears only when the balance of Larmor presession with relaxation mechanisms is achieved.

If the pump light intensity is too high, the pumping process can completely destroy NMOR, by immediately restoring the rotating alignment back to its initial state. If external magnetic is strong so that Ω_L is faster than the relaxation rate Γ, each atom will contribute to net polarization over its entire precession cycle and the macroscopic alignment will also be completely destroyed (averaged out). Only in case when $\Omega_L \leq \Gamma$ each particle would not be able to complete the whole precession cycle before relaxing, therefore some residual net anisotropy would be maintained. This effect is called zero-field NMOR and allows to measure external magnetic field of less than a couple nT.

However, if the pumping occurs in synchrony with Larmor presession, the quantum state of newly pumped atoms will be in phase with atoms from previous cycles. Therefore all atoms precess in unison maintaining macroscopic atomic alignment even in the case when $\Omega_L \gg \Gamma$. This synchronization occurs when modulation frequency $\Omega_m = 2\Omega_L$. As a result polarization plane of probe light is modulated with $2\Omega_L$. This method is known as synchronous optically pumping or optically driven spin precession [72, 82, 95, 96].

2.1.5 The Magnetometer Response

When using synchronous pumping the modulated polarization of probe light can be measured by using phase-sensitive detection. An example of in-phase and quadrature components of the NMOR signal is shown in Fig 2.6. In addition to zero-field resonance, two high-field resonances are observed at $B_{ext} = \pm\Omega_m/2\gamma$, which corresponds to $\Omega_m = 2\Omega_L$ [72, 82, 95–97]. The NMOR signals are observed when the mismatch between the Larmor frequency and half of the modulation frequency does not exceed the relaxation rate of the atomic alignment.

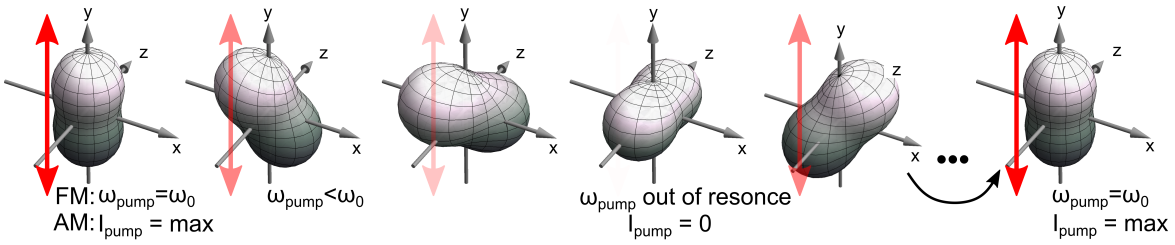

Figure 2.5: Schematic visualization of the synchronous pumping of atoms. Two techniques can be employed to modulate the pumping rate of atoms. Pumping light intensity can be modulated, which effectively switches on and off the pumping process with $2\Omega_L$ frequency - amplitude modulated approach (AM). Or pumping light can be going in and out of the resonant frequency required to excite the atoms - frequency modulated approach (FM). In that case frequency of the pumping light is scanned over one wing of a Doppler-broadened atomic transition with $2\Omega_L$ frequency. The visualization was done using a package written for Mathematica to facilitate density-matrix calculations [80].

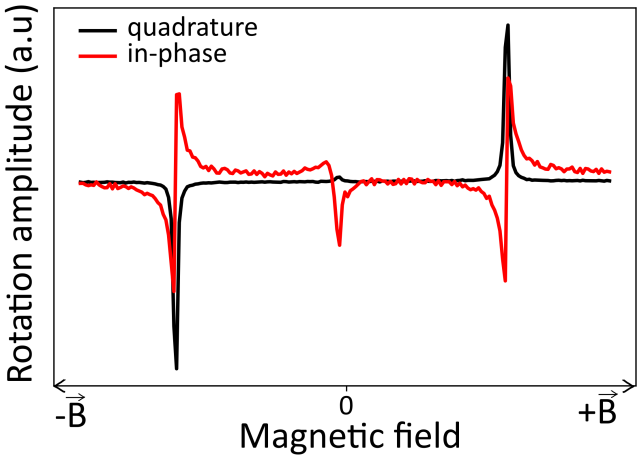

Figure 2.6: In-phase (red) and quadrature (black) components of the typical NMOR signal recorded. The central peak is the zero-field resonance that arises due to the nonlinear Faraday effect without optical pumping, while two resonances on the sides are high-field resonances associated with synchronous pumping.

2.1.6 Spin Relaxation

The sensitivity of the OPM is fundamentally limited by atomic-shot noise and photon-shot noise [72, 98–100].

Atomic-shot noise limit originates from fluctuations in the number of atoms that contribute to the signal.

$$\delta B_{\mathrm{at}} = \frac{1}{\gamma}\sqrt{\frac{\Gamma}{nV}}\,, \tag{2.5}$$

where Γ is the half-width at half maximum of the NMOR resonance or relaxation rate, and n is the atomic density.

Photon-shot noise, on the other hand, refers to the statistical fluctuations in the number of photons detected or measured in a given time interval.

$$\delta B_{ph} = \left(\frac{d\tilde{\phi}}{dB}\right)^{-1} \delta\tilde{\phi} \tag{2.6}$$

where $\tilde{\phi} = 1/(2\sqrt{N_{ph}})$ is the photon-shot-noise-projected sensitivity of the optical measurement, N_{ph} is the number of photons in the light beam per unit of time. In case of NMOR configuration δB_{ph} is given by

$$\delta B_{ph} = \left(\frac{d\tilde{\phi}}{d\Omega_m}\frac{d\Omega_m}{dB}\right)\delta\tilde{\phi} \tag{2.7}$$

$$\frac{d\tilde{\phi}}{d\Omega_M} \approx \frac{A_N}{\gamma} \tag{2.8}$$

$$\delta B_{ph} = \frac{\Gamma}{2\gamma A_N}\frac{1}{\sqrt{N_{ph}}} \tag{2.9}$$

where A_N is the amplitude of the NMOR signal.

Photon-shot noise is the leading contribution to the sensitivity of the NMOR sensor [95]. From Eq. 2.8 it becomes apparent that in practice when optimizing the sensor one has to achieve the largest possible ratio between the amplitude of the resonance and the width of the resonance to make the most sensitive sensor. Intrinsic sensitivity of any type of optically pumped magnetometer δB_i is given by [99]

$$\delta B_i = \sqrt{(\delta B_{\mathrm{at}})^2 + (\delta B_{\mathrm{ph}})^2}\,, \tag{2.10}$$

The distinction between different types of OPMs lies in the methods used to increase the

relaxation time, which ultimately leads to improved magnetometer sensitivity.

Both δB_{at} and δB_{ph} depend on the width of the resonance Γ, which is the inverse of the spin relaxation time [72]. The sum of several relaxation rates determines the width of the resonance [99, 101]:

$$\Gamma = R_{se} + R_{wall} + R_{light} + R_{noise} \tag{2.11}$$

where R_{se} is the spin-exchange collision relaxation rate, R_{wall} is the wall collision relaxation rate, R_{light} is the light-induced relaxation rate, and R_{noise} is the relaxation rate induced by external field fluctuation. Equations for each of these processes depend on the specific configuration of the OPM sensor will be discussed in the details in Chapter 4. As an example, a table-top NMOR sensor using the ^{87}Rb D2 line with a light intensity of > 5 mW/cm^2 achieved a photon noise-limited sensitivity of approximately 3×10^{-16} T/$\sqrt{\text{Hz}}$ [102]. Another implementation on an optical table with hot ^{87}Rb vapour gas atomic shot noise limit can be as low as $\approx 4.9 \times 10^{-16}$ T/$\sqrt{\text{Hz}}$ [103].

2.2 Types of OPMs

In this section, I will discuss the advantages, and disadvantages of various types of OPMs that are commonly employed in MEG. I have selected four types of sensors for discussion, two of which, namely SERF and ^{4}He, are commercially available (QuSpin Zero-Field Magnetometer; FieldLine Mag4Health). The NMOR-OPM sensor is the main focus of this dissertation, while the fourth sensor, FID, has demonstrated remarkable performance by operating without any shielding [104]. The summary of the sensitivity, advantages, and challenges of the sensors mentioned above can be found in Table 2.1. Other magnetometers, such as the Mx, Mz magnetometers that measure x or z components of the magnetic moment by observing the absorption of a transverse light beam during magnetic resonances [105–108], radio-frequency magnetometers that measure oscillating magnetic fields by applying a weak oscillating radio-frequency field transverse to the measured field [109–111]), double-resonance magnetometers [112, 113], co-magnetometry that uses two different atoms in the cell [114, 115] or novel solid-state fluxgate

magnetometer [116] and magnetometers based on nitrogen-vacancy centres in diamonds [117, 118] which have comparable performance to the discussed sensors, are not within the scope of this discussion. Their working principle can be found in [33, 47, 71, 72].

The key difference between types of OPM sensors is how in each of them the effect of the spin relaxation is reduced, which in turn defines their strengths and weaknesses.

2.2.1 Nonlinear magneto-optical rotation based OPM

In NMOR OPM lifetime of ground state Zeeman coherence is longer than coherence-destroying collisions, therefore the main mechanism of the relaxation is due to spin-destruction collisions with the wall. In order to increase the coherence lifetime, the number of such collisions should be reduced. It can be done either by filling the vapour cell with the noble buffer gas so that alkali atoms do not freely travel through the cell, or by coating the cell walls with an antirelaxation coating so that spin-depolarization from the interaction with the cell is greatly reduced [119]. After that, the main mechanism of the relaxation is the collision of atoms with themselves resulting in them exchanging spins [101].

One beam simplified scheme of NMOR OPM where the probe and pump light are in one beam is shown in Fig 2.7. Note that the magnetometer measures the magnetic field parallel to the beam.

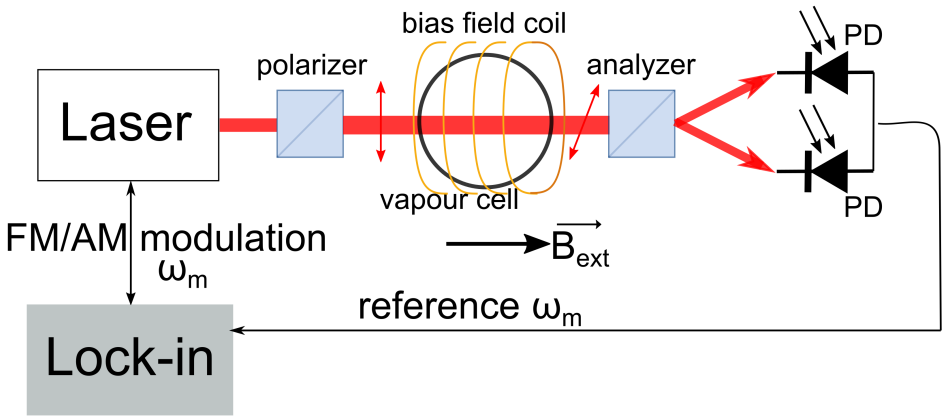

Figure 2.7: Simplified one beam scheme of NMOR OPM using linearly polarized light [120].

The NMOR-OPM sensor has been successfully implemented in experiments using isotopes such as ^{87}Rb, ^{87}Rb, and Cs [73, 93, 120, 121]. The experimental results have demonstrated a noise floor of approximately 20 fT/$\sqrt{\text{Hz}}$ [44]. The main advantage of this sensor over other types of sensors discussed below is that it can operate in a wide range of magnetic fields up to Earth's magnetic field [89]. Therefore less magnetic shielding discussed in Chapter 1 is needed which significantly lowers the cost of the whole OPM-MEG system. Furthermore, NMOR-OPM can be combined with TMS. This allows us to assess brain connectivity by stimulating one region and measuring the response in another region. Another advantage of the NMOR OPM for MEG applications is that it operates at room temperature. This allows to put the cell directly in contact with the subject scalp without causing any discomfort. However low-density requirements to minimize spin-distraction collision make it harder to miniaturize the sensor, i.e. reducing the sensor's footprint (cross-section area) on the head, while maintaining the appropriate sensitivity to measure brain signals. The upper limit of the bandwidth of the sensor can be larger than 1 kHz and is limited by Larmor frequency, the lower limit of the bandwidth is 3-4 Hz due to technical noises which include polarization drifts, laser power noise, power-supply noise, shield noise, photodiode noise, Johnson noise from bias coils, modulation-frequency instability [81].

2.2.2 Spin-Exchange-Relaxation-Free based OPM

The most common OPM sensor realized commercially is working in a spin-exchange-relaxation-free regime (SERF) [122, 123]. In this regime spin exchange relaxation rate is solved by increasing atomic density so that collisions occur so fast, that atoms spend less time in a particular state between collisions until they coherently precises at a single, slowed-down frequency [98]. Therefore, this regime has a smaller bandwidth than NMOR-OPM [47]. Also, a buffer gas cell is used to suppress the wall collision relaxation rate. These sensors are limited by spin-destruction collisions, hence the extensive use of Rb and K with their smaller collisional cross-sections in comparison to Cs [39]. The standard noise floor of commercial magnetometers is around 7-10 fT/$\sqrt{\text{Hz}}$, which is smaller than NMOR-OPM. To date, the highest demonstrated sensitivity is 0.16 fT/$\sqrt{\text{Hz}}$ at 40 Hz in the gradiometer mode using two 0.45 cm^3 volumes in one cell [124].

Another implementation using two 42-pass volumes (0.66 cm^3) in one big cell reported the noise less than 1 $fT/\sqrt{Hz}$ in the range 10–150 Hz, with a minimum of 0.54 $fT/\sqrt{Hz}$ in the range 28–45 Hz [103].

The optical scheme of the commercial SERF sensor in the single-beam configuration is shown in Fig. 2.8.

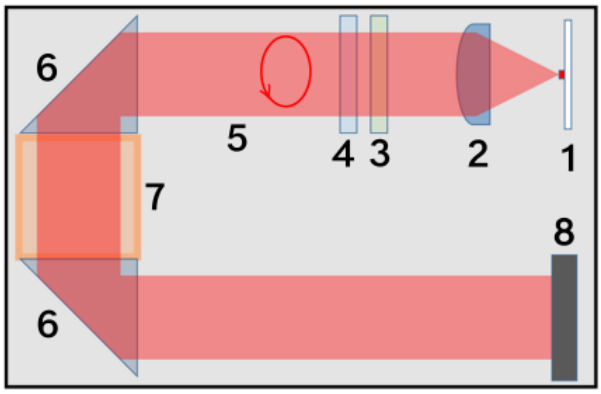

Figure 2.8: Simplified scheme of the SERF QuSpin OPM adapted from [122]. (1) 795nm laser; (2) Collimating lens; (3) Linear polarizer; (4) Circular polarizer; (5) Light beam; (6) Reflecting prisms; (7) vapour cell; (8) Photodiode (Coils not shown) to measure the change in light intensity.

SERF-OPM measures the magnetic external field in the orthogonal direction of the pump beam. The detailed working principle of the SERF-OPM can be found in [72, 98]. The sensor is using circularly polarized light to pump the atoms. Due to continuous absorption, the light-coupled Zeeman sublevel becomes depleted, leading to the transparency of the vapour to the laser light. When the external magnetic field is introduced, atomic alignment undergoes Larmor precession and atoms can again absorb laser light, causing a drop in light intensity at the photodetector, which is used to calculate the external magnetic field. The modulation of the magnetic field in the transverse direction is employed to address the symmetric nature of the Lorentzian function, which is centred around zero.

SERF-OPM utilizes zero-field resonance, which reduces the dynamic range (i.e., the range of field an OPM can tolerate) of the sensors to ~3 nT [4]. Utilizing closed-loop operation mode, whereby sensors are operated in a continuous feedback loop, the dynamic range is increased to ~10 nT [125]. This is the main disadvantage of this type of OPM. To solve

this issue different methods of magnetic shielding briefly discussed in Chapter 1 are designed. An additional challenge associated with SERF-OPM is a hot vapour cell with temperature $\sim$ 150°C – 240°C. These cells require maintaining some distance from the participant's head (6 mm in the commercial sensors). Commercial the SERF-OPM has bandwidth around 100 Hz, however in [126] authors increased it to 10 kHz, sacrificing the sensitivity to 30 fT/$\sqrt{\text{Hz}}$. The lower boundary, where sensitivity exceeds 15 fT/$\sqrt{\text{Hz}}$, is reported to be 3 Hz [127]. The bandwidth of SERF is smaller the for NMOR because to suppress If NMOR sensors are still quite bulky ($3 \times 3 \times 11$ cm^3), SERF sensors can operate with microfabricated vapour cell [101, 128], therefore can be miniaturized to the lego brick size ($\approx 4 \times 15 \times 8$ mm^3). Overall SERF OPM stands out as the most sensitive sensor of the OPMs discussed here.

2.2.3 Free-induction-decay OPM

Although theoretically, NMOR-OPM can operate in Earth's magnetic field without any shielding, this has yet to be demonstrated experimentally. On the other hand, free-induction-decay OPM (FID) has been shown to measure audio-evoked fields outside of laboratory settings [104]. These measurements were conducted with sensors arranged into a synthetic gradiometer configuration, each magnetometer had sensitivity $\approx$ 35 fT/$\sqrt{\text{Hz}}$, and the gradiometer had sensitivity $\approx$ 16 fT/$\sqrt{\text{Hz}}$ between 26 and 115 Hz.

Free-induction-decay magnetometer can utilise the same optical pumping principle as either SERF-OPMs and NMOR OPM using circularly or linear polarized light, but instead of continuously pumping the atoms, FID employs a single pulse or synchronous pumping [81, 129–131]. In the period of pumping switched off the probe light is used to detect the dynamic of Zeeman ground state coherence precession induced by an external magnetic field. An external magnetic field is inferred from the oscillation of the polarization plane of the probe light. This magnetometer infers the value of a magnetic external field from the time domain of the read-out signal as opposed to techniques that employ lock-in amplifiers. The pumping scheme and the resulting signal are shown in Fig 2.9.

Typically, magnetometers utilize cells filled with either Rb or Cs atoms along with a buffer

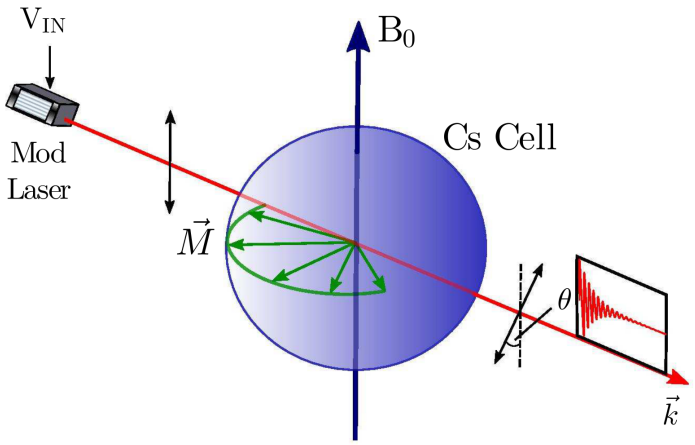

Figure 2.9: Simplified scheme of the FID OPM from [39]. The laser is modulated to alter the absorption coefficient with a strong atom-light interaction building up spin polarization during the pump phase. The interaction strength is then lowered and the time-dependent optical rotation angle is monitored.

gas. These cells are heated to $\approx$ 100°C. Therefore the distance has to be maintained between the cell and the participant's head. The sensor can operate with microfabricated cells and hence can be miniaturized to the sizes of commercial SERF sensors, however, they lose in sensitivity. One implementation with micro-electromechanical systems (MEMS) vapour cells showed 238 $\mathrm{fT}/\sqrt{\mathrm{Hz}}$ within the bandwidth of 10 to 500 Hz [132]. The magnetometer bandwidth is limited to half the repetition rate of the sensor (i.e. the rate of the pumping pulse), also referred to as the driving frequency $f_d = 1/T$, in accordance with the Nyquist theorem. The main advantage of this magnetometer after being able to operate without shielding is that they do not require individual calibration. Therefore assembling them into the gradiometers or putting them together in the array is very easy. FID sensors have a simpler design compared to OPM utilizing lock-in amplifiers. Unlike driven architectures, which are susceptible to systematic errors stemming from auxiliary instrumentation, FID sensors do not experience issues related to heading error, drift over time caused by technical noise, or AC Stark effect, which can result in a characteristic shift in the Larmor frequency [129]. All these issues can be solved in other OPMs but they require additional engineering solutions. Note, that FID OPMs are inherently scalar sensors, contrary to other OPMs discussed here, and do not provide information regarding the field

orientation.

2.2.4 ^{4}He OPM

Another commercial OPM-MEG system uses OPM sensors based on metastable helium-4 atoms (^{4}He) [29]. This sensor is based on zero-field parametric resonance which uses radio-frequency (RF) magnetic fields for modulating the photo-detection signals. The metastable level is generated through the application of a high-frequency discharge. Linearly polarized continuous light used as pump light creates a quadrupole magnetic moment of the atomic ensemble of ^{4}He metastable level. Quadrupole magnetic moment aligns along one of the polarizations of $\overrightarrow{E}_{pump}$, which makes the external magnetic field propagating along the pumping beam to be traversed to the alignment [16, 133–135]. Hence this external field can induce an alignment rotation, and therefore light absorption, which is then measured. One of the advantages of the ^{4}He OPM is that it can detect all three directions of the external magnetic field using only one beam. SERF and NMOR OPM can also be constructed into a tri-axial mode, however, it requires at least two laser beams and the sensors slightly lose their sensitivity. Three-axis parametric resonance magnetometer measures an arbitrarily oriented B_{ext} using two RF fields perpendicular to $\overrightarrow{E}_{pump}$ with different frequencies. These two RF fields modulate the magnetic moments of the atoms so that in the probe light spectrum these frequencies will be used to infer external magnetic field value. The principle is shown in Fig 2.10.

The sensitivity of the commercial sensor is $approx$ 43 fT/$\sqrt{\text{Hz}}$. The important advantage is these sensors is their dynamic range is ±250 nT [136]. ^{4}He sensor has a comparable footprint to the commercial SERF sensors. The primary advantage of this sensor is its ability to measure low-frequency brain activity due to its wide bandwidth, ranging from DC to 2 kHz.

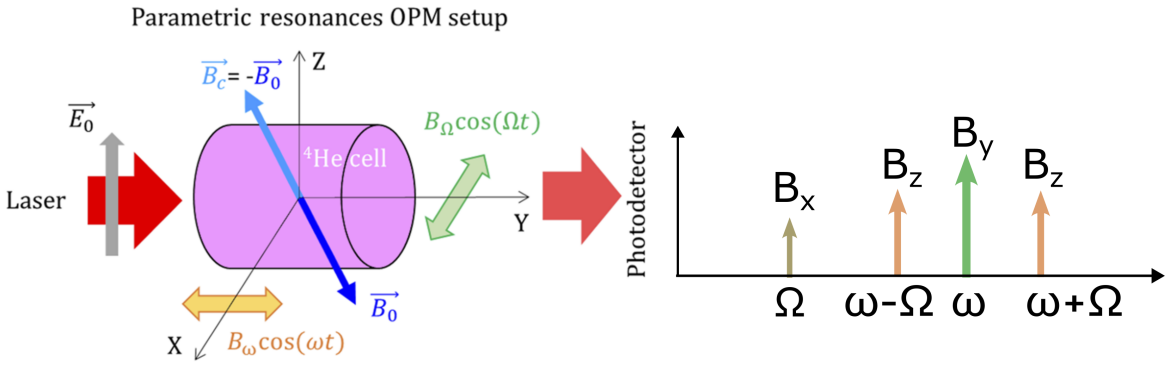

Figure 2.10: Simplified scheme of the ^{4}He OPM main elements of the parametric resonance magnetometer architecture and the frequency component of output signal adapted from [16, 133]

Technique	Sensitivity ($fT/\sqrt{Hz}$)	Advantages	Challenges
NMOR OPM	15 cell 4x4x4cm^3 [81]	large dynamic range room temperature operability can be combined with TMS	big footprint coregistration denoising algorithms
SERF OPM	7-10 cell 0.2x0.3x0.3cm^3 [127]	small footprint triaxial mode low noise floor	low dynamic range requires heating use buffer gas cell bandwidth coregistration denoising algorithms
FID OPM	35 cell 0.8x0.8x1,2cm^3 [104]	large dynamic range no lock-in amplifier can work without a feedback loop no light shift error large bandwidth	measurement dead time big footprint coregistration denoising algorithms
He^4 OPM	<43 cell 1x1x1cm^3 [136]	large dynamic range single beam triaxial mode room temperature operability no CAPE no low-frequency noise large bandwidth	measurement dynamic range big footprint coregistration denoising algorithms
SQUID	3-4 [4]	the lowest noise floor developed algorithms to analyse data no CAPE or cross-talk	liquid helium far from the scalp rigid helmet

Table 2.1: Various types of OPMs commonly employed in MEG, their sensitivity, and their advantages and challenges.

Chapter 3

Development of NMOR OPM sensor for MEG experiment

This chapter incorporates content from the paper titled "Detection of human auditory evoked brain signals with a resilient nonlinear optically pumped magnetometer" authored by Anna U. Kowalczyk, Yulia Bezsudnova, Ole Jensen, and Giovanni Barontini, and published in NeuroImage (2021). My contribution involved experimental design, conducting experiments, collecting and analyzing data, and creating figures. While portions of the material in this chapter remain unchanged from the paper, others have been adapted to suit the context of this thesis.

One way to make OPMs more effective for MEG applications is to extend their dynamic range, as current commercial sensors are limited to ±1.5 nT. There are a few solutions proposed to address this limitation, such as adding nulling coils to the sensors or using them in closed-loop mode. In this chapter, I introduce a complementary approach for MEG using an OPM sensor designed to withstand ambient magnetic fields without the need for extra peripheral hardware. This OPM sensor utilizes the NMOR technique, which, in theory, offers an extended dynamic range encompassing geomagnetic fields. In this study, we successfully identified auditory evoked fields (AEF) within a background field of 70 nT using NMOR OPM. We show comparable performance between our sensor and conventional SQUID sensors. Additionally, we demonstrated our sensor's ability to detect modulations in brain oscillations within the alpha

band.

3.1 Introduction

The majority of commercially available sensors used in laboratories worldwide are SERF sensors, which rely on zero-field resonance. These sensors are capable of measuring only magnetic fields that induce precession with a Larmor frequency (Ω_L) slower than the relaxation rate (Γ) of the atoms in their vapour cell ($\Omega_L \leq \Gamma$). Therefore these sensors have a very limited intrinsic dynamic range ± 1.5 nT [137]. Introducing the closed-loop mode, where dynamic negative feedback is applied to the measurement-axis field coils to maintain a zero field at the vapour cell, leads to an increased dynamic range of up to ±5 nT [48]. However, the static field within our typical commercial MSR is 30-40 nT with gradients of ≈ 10 nT/m [48]. As a result, to operate zero-field sensors, it is necessary to either implement adaptive external field nulling coils [138, 139] or use high-performance shielded rooms [49]. Implementing these solutions is both hardware-intensive and costly, which reduces the cost benefits associated with an on-scalp OPM-MEG system. In this study, we developed an OPM sensor that can operate in a high background field (≥ 70 nT) environment without the need for extra peripheral hardware. Our OPM sensor is based on the NMOR technique [95, 120, 140] described in detail in Chapter 2. Though the fundamental sensitivity limit for NMOR OPM sensors is in general higher than SERF OPM sensors [8], the actual sensitivity which accounts for all external interferences that cannot be eliminated is usually constrained by technical noise sources [36]. Thus, given the current state of the OPM-MEG system (including OPM sensors, electronics, and magnetic shielding), the difference in fundamental sensitivity limits between NMOR OPM and SERF OPM does not necessarily translate into lower NMOR performance. However, the NMOR sensors offer the advantages of requiring less shielding and providing a greater dynamic range. Additionally, NMOR OPM sensors equipped with anti-relaxation coated cells operate at room temperature, while SERF sensors with buffer gas cells require heating to temperatures exceeding $100°C$. This allows the former to be placed directly on the head without ventilation issues when assembled

in an array. In contrast, SERF sensors require extra insulation spacing ≈ 6 mm and special care when arranged in an array configuration.

In this study, we demonstrate the detection of auditory evoked fields in an environment with a background magnetic field of 70 nT. We benchmark our sensor with a commercial SQUID sensor, also demonstrating the possibility of measuring stimulus evoked modulations in oscillatory brain activity.

3.2 Sensor design

A schematic representation of the sensors is shown in Fig. 3.1. The sensor system comprises two modules: the sensor head, which contains only optical and non-magnetizable components, and an external module housing all the electronic components positioned outside the magnetically shielded room. These modules are connected by a 5 m umbilical cable, which contains optical fiber, which delivers the light to the sensor, a shielded coaxial cable, which brings the sensor output outside the MSR, and a copper wire which delivers DC currents to the sensor head. This modular arrangement effectively reduces the magnetic artefacts from the electronics but also enables a single laser to drive several sensor heads. Additionally, this setup enables the combination of the sensor with TMS, because powerful magnetic field pulses of TMS could not damage the laser and electronic components since they are located outside the sensor head.

In the external module outside the MSR, the laser light is provided by a Toptica DL Pro diode laser at 795 nm. We employed two techniques to synchronously pump atoms: amplitude modulation (AM), which switches the pumping process on and off at a frequency of $2\Omega_L$, and frequency modulation (FM), where the pumping light's frequency is scanned over one wing of a Doppler-broadened atomic transition with a frequency of $2\Omega_L$ effectively going in and out of the resonant frequency required to excite the atoms. AM NMOR was implemented by using an acousto-optic modulator (AOM). The unmodulated laser light double passed through AOM driven by an 80-MHz radio-frequency signal, achieving 100% sinusoidal depth modulation of the first-order beam. FM NMOR was implemented by directly modulating the injection current

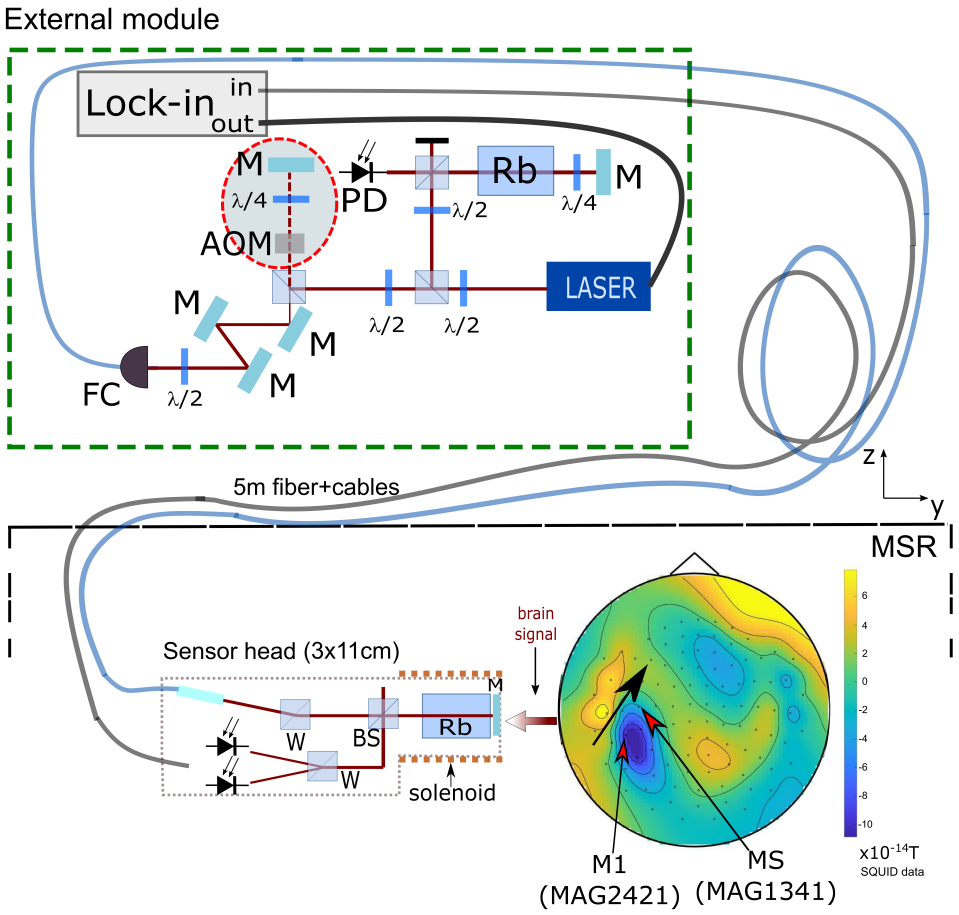

Figure 3.1: Schematic representation (not to scale) of our NMOR OPM modular system. The external module (the dashed green box) includes a laser and the optics for fiber coupling, the electronics (not shown) and the lock-in amplifier. The part of the scheme used to modulate amplitude for AM approach of synchronous pumping is shown in a red dashed circle. When the scheme is used in frequency modulation (FM) mode that part of the scheme is blocked off. In FM approach the output of the lock-in amplifier is used to modulate the frequency of the laser. M indicates the mirrors, PD the photodiodes and FC the fiber coupling. AOM is acousto-optic modulator. The external module is connected to the sensor head through an umbilical that contains an optical fiber that delivers the light (blue line), a shielded coaxial cable that carries the output of the sensor and a wire to set the bias field in the sensor (black line). The all-optical sensor head and a participant are both positioned inside the magnetically shielded room (MSR), marked as a black dashed line. BS indicates the 90/10 beam splitter and W the Wollaston prisms. The contour map illustrates the auditory evoked response measured at 100 ms by the whole-head SQUID system (magnetometers). The black arrow indicates the radiating dipole. The inset on the top right shows a 3D rendering of the sensor head.

of the laser diode. The sinusoidal modulation signal, with an amplitude of around $\approx$ 1 GHz, is generated by a lock-in amplifier (Zurich Instruments MFLI). 10% of the laser radiation is directed to the absorption spectroscopy scheme for frequency referencing, while the rest of

the light suitably attenuated is transmitted to the sensor head through a 5-meter polarization-maintaining (PM) optical fiber. The pigtailed GRIN lens glass collimator produces a beam waist of 0.5 mm at the opposite end. Intensity control before the fiber is achieved using a rotated half-wave plate and a Wollaston prism.

The sensor head output is transmitted back to the external module via a 5 m SMA cable to a transimpedance amplifier (Koheron PD01). This amplifier both magnifies the signal and reduces dark currents by biasing the photodiodes without voltage. Afterwards, the signal is digitized using the built-in analogue-to-digital converter in the lock-in amplifier, boasting a 16-bit resolution and a 60 MSa/s conversion rate. Subsequently, the digitized signal is demodulated at the modulation frequency Ω_m.

All the preparation experiments were conducted in three layers of cylindrical mu-metal shielding. In these experiments, we used bias coils to simulate the external magnetic signal. The experiment with the subject was conducted in the magnetically shielded room MSR (2 layers of mu-metal and 1 layer of aluminium with the residual magnetic field measured upon installation to be $\approx$4 nT). The room is built for conventional MEG experiments and has an MEGIN TRIUX system installed inside, together with a cryocooler. The cryocooler cold-head makes for a challenging environment as it produces spurious magnetic fields and magnetic field gradients inside the MSR. At a 2 m distance, where we operate our NMOR OPM, the background magnetic field is $\geq$ 70 nT and the magnetic field gradient can be up to 240 nT/m. Note that zero-field OPM sensors are not able to work in such an environment without an extra compensation system [138, 141]. As mentioned in section 3.2.1 the high bias field makes NMOR sensors resilient to the ambient field and, moreover, NMOR sensors are insensitive to transverse gradients. Therefore, we oriented our sensor to have the smallest gradients in the direction of the measurement. In our MSR, we have measured slow variations from 50 pT to 1 nT per hour, and sudden jumps of up to 3 nT

3.2.1 Sensor head

A schematic representation of the sensor head is given in Fig. 3.1. The images of the actual sensor are shown in Appendix A. Inside the sensor head, we use a single beam to pump and probe the atoms. The light passes through the Wollaston prism to extract one linear polarization and then through a 90/10 non-polarizing beam-splitting cube. 90% of the incident power is reflected and sent to a photodiode, whose output can be used in a feedback loop to compensate for polarization fluctuations induced by the optical fiber. The remaining 10% is sent to the atomic vapour cell, which has a paraffin coating on the walls. A retro-reflected mirror is fixed on the other end. The cell is a 2 cm long cylinder with a 1.8 cm diameter base and is placed inside a 3 cm diameter solenoid that provides a constant bias magnetic field along the radial y direction (see Fig. 3.1). The double-passing scheme is employed to extend the atom-light interaction time by a factor of two. On the way back, the beam passes again the 90/10 cube and the rotation angle is analysed using a balanced polarimeter. This comprises a Wollaston prism mounted at 45 with respect to the incident light polarization and two low-noise photodiodes in a ceramic assembly (Hamamatsu S1337-33BQ) connected in series. In this configuration, the photocurrents cancel each other when they are equal. Including all these elements, the current sensor head is a cylinder with a base area of 3 cm diameter and length of 11 cm. The sensor sensing axis was placed to be radial to the subject head.

Bias field

The bias field is used to control the "carrier" Larmor frequency Ω_L^0 at which the atomic alignment rotates in the absence of any brain signal. To improve the resilience of the sensor, this field should be significantly larger than any background field. This ensures that Ω_L^0 is stable and minimally perturbed by the ambient field perturbations. This way every component of the background field that is not parallel to the bias field is strongly suppressed [142]. Our sensor is therefore designed to measure magnetic fields along y direction. In our working conditions, the bias field is typically in the range of 100-150 nT and is generated using an ultra-low noise current supply (HighFinesse BCS 20 mA). This bias field overcomes the residual field inside

the MSR, which is typically between 40 and 100 nT.

Paraffin coated vapour cell

We decided to use an anti-relaxation coated vapour cell containing ^{87}Rb atoms mainly due to its room temperature operability. The paraffin coating on the walls enables atoms to undergo up to 10,000 collisions without depolarization, resulting in a four-order reduction in spin depolarization due to wall interactions [143]. This is because the paraffin coating contains no free electron spins and has lower adsorption energy than bare glass, reducing the time atoms spend adsorbed on its surface compared to the glass surface. An alternative method to address spin destruction due to collisions with the cell walls is to employ a buffer gas cell, which restricts the movement of atoms within the cell. However, utilizing a surface coating offers several advantages, such as no need to increase the cell temperature, lower laser power needs, larger optical signals, reduced susceptibility to magnetic-field gradients, and a lower collision rate with other atoms and molecules within the cell [119]. With the use of a paraffine-coated cell, the main mechanism of spin relaxation in NMOR becomes spin-exchange when atoms collide with each other.

3.2.2 Sensor operation modes

Our sensor operates in two modes "unlocked" and "tracking". In the unlocked mode, we obtain a dispersive and an absorptive curve at the in-phase and quadrature outputs of the lock-in amplifier shown in Fig 2.6 and in Chapter 2. We use the unlocked mode to optimize the NMOR OPM performance. In the tracking mode, we can track the changes of the external magnetic field in real-time. In this mode, the signal provided by the balanced photodiodes is fed directly to the laser current modulator using a phase-locked loop (PLL) of the lock-in amplifier. PLL is a closed-loop negative-feedback control system that maintains the constant difference between phases of two periodic signals (polarimeter output and laser current modulator). The output parameter of the PLL is the modulation frequency, which we record together with the frequency shift (difference between the initial locking frequency and a "tracked" one) using the digital acquisition (DAQ) module incorporated in the lock-in amplifier. Any change in the magnetic

field due to brain activity is immediately sensed by the atoms and reflected in a change of their Larmor frequency and thus modulation frequency $\Omega_m = 2\Omega_L = 2g_e\mu_B B/\hbar$. In other words, the atoms themselves set the frequency determined by the magnetic field in real-time [144]. In the tracking mode, our sensor can have up to 1 kHz bandwidth. In case of sudden external magnetic field jumps larger than our OPM resonance width of 25 Hz (2 nT) the sensor unlocks, PLL loop breaks. These are rare events, and the sensor can be readily re-locked without any further calibration. The dynamic range of the sensor is quite large and we measured slow drifts with amplitude up to 100 nT.

3.3 Participant and experimental paradigm

A healthy male subject, aged 35, was recruited for this study, which was conducted at the Centre for Human Brain Health at the University of Birmingham, United Kingdom. The research protocol received approval by Ethical Review Committee at the University of Birmingham. The participant was provided with information about the experimental procedure during both the SQUID and OPM experiments.

We recorded auditory ERFs in two sessions: one using a conventional SQUID-based MEG system and one using our NMOR OPM. Sessions were conducted on separate days. During the SQUID session, signals were continuously recorded using a 306 sensor MEGIN TRIUX system. The data were filtered by 330 Hz low-pass and 0.1 Hz high-pass filters and then sampled at 1 kHz. During the OPM session, a single sensor OPM recording was obtained. The data of the NMOR OPM session were recorded using the DAQ module integrated with the lock-in amplifier and down-sampled to 1.35 kSa/s (from 60 MSa/s). The length of each trace was set to 970 ms.

We used an oddball paradigm to keep the participant's attention. During both sessions, the subject was presented with two 100 ms tones of respectively 1 kHz (75% of the trials) and 1.04 kHz(25% of the trials) and the inter-stimulus interval was randomly varied from 811 to 840 ms. The sound was generated using a SOUNDPixx MRI-compatible audio system and was delivered to the right ear of the participant using air tubes and disposable earpieces. The subject was not

required to respond but was asked to concentrate on the tones throughout the experiment and was instructed to remain still for the duration of the experiment. We recorded a total of 300 SQUID-MEG trials. During the SQUID session, the subject was seated while in the NMOR OPM session, the subject was lying in the supine position, with the head comfortably supported. For the NMOR OPM measurements, the recording area was identified using the data obtained in the SQUID session. We identified the MEGIN-MEG sensors with the strongest magnetic field response and placed the OPM sensor approximately in the same location. The sensor was fixed to the bed using non-magnetic materials. We recorded a total of 450 traces in the NMOR OPM session.

3.3.1 Data analysis

One of the main challenges of operating a single OPM sensor in the MSR is to deal with the drifts of the background magnetic field. To minimize the effect of such drifts, we removed traces where the external magnetic field drifted more than 1.5 pT per second, resulting in 200 usable trials. This was done because such drifts exceed the expected magnitude of the brain signal. The auditory event-related fields were calculated by applying a 35 Hz low-pass filter, averaging the trials from all the tones, and subtracting the 100 ms baseline interval.

We selected two SQUID sensors to show with results from OPM session. First, we selected for comparison the magnetometer that measured the strongest ERF. It is labelled as $M1$ in Fig. 3.1. In addition, the SQUID magnetometer that has the most similar response to the one measured by NMOR OPM is also shown here. The similarity was assessed by computing the Pearson correlation between SQUID sensors ERF and OPM ERF. The SQUID magnetometer with the highest correlation coefficient is chosen. It is labelled as MS in Fig. 3.1. Note that since there is no direct mapping of the placement of the OPM sensor to SQUID channels, the comparison between OPM response and $M1$, MS is constrained.

SQUID data was analysed using the same criterion as the OPM session to minimize the effect of drifts in the magnetic field i.e., removing the traces with drifts higher than 1.5 pT/s, we obtained 200 trials from the SQUIDs sensors. The traces were low-pass filtered at 35 Hz and

then averaged. A 100 ms baseline was subtracted. We did not apply signal-space projections to the $M1$ sensor for a fair comparison of the performance with the OPM data. Conversely, such techniques were applied to the MS sensor to better highlight the shape of the auditory evoked response.

For both sessions, the time-frequency representation of power was calculated per trial using a 300 ms time window sliding with 50 ms time steps. A Hanning taper was applied to each 300 ms time window prior to Fast-Fourier Transformation, after which the power was derived. The baseline was taken from - 60 to - 50 ms before the tone onset.

3.4 Results and discussion

3.4.1 Sensor optimization

We were surprised to observe a significant reduction in AM NMOR sensitivity when moving our sensor from a compact shield to the MSR room. We attributed it to the use of 5m PM fiber that transfers light from the external module to the sensor head. Temperature fluctuations and vibrations were disrupting the modulation of the beam intensity as it traveled through the extended PM fiber, resulting in decreased NMOR sensitivity. In contrast, during the experiment in the compact shield, the umbilical cord was carefully folded and secured near the shield, ensuring that the entire fiber remained in one place.

Fig.3.2 demonstrates the NMOR signal in unlocked mode. The typical NMOR signals can be observed as a function of: the magnetic field (magnetic field domain) or the modulation frequency (modulation frequency domain). The central peak is the zero-field resonance that arises due to the nonlinear Faraday effect without optical pumping. Two resonances on the sides are high-field resonances associated with synchronous pumping. The overall sensitivity of the sensor (σ_a), i.e. the combined contribution of intrinsic sensor sensitivity (σ_i) and the environmental noise, can be calculated by estimating the half-width at half maximum of the NMOR resonance Γ in a modulation frequency domain and the signal-to-noise ratio (SNR) from the square root of the power density spectrum [95] from unlocked mode measurements (Fig. 3.2

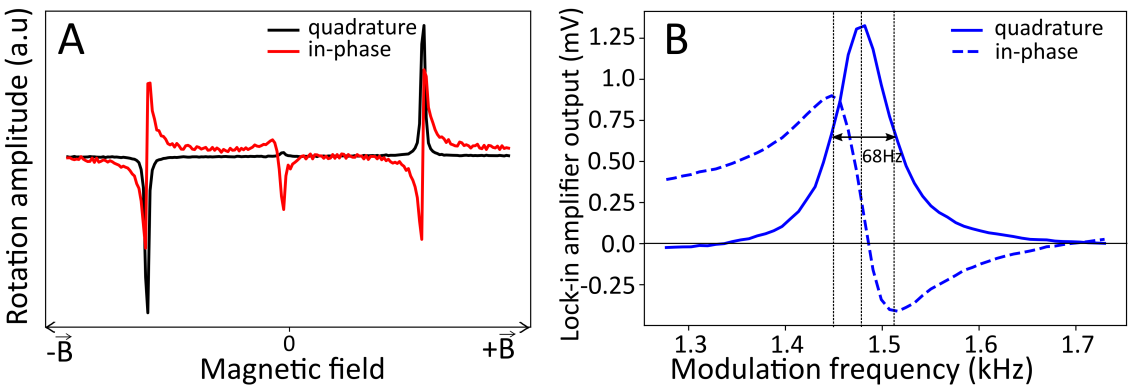

Figure 3.2: A) In-phase (red) and quadrature (black) components of the typical NMOR signal recorded in the magnetic field domain. The central peak is the zero-field resonance that arises due to the nonlinear Faraday effect without optical pumping, while two resonances on the sides are high-field resonances associated with synchronous pumping; B) One of the high-field NMOR resonances recorded in the modulation frequency domain measured with incident light power 7.6μW and red laser detuning 430Hz, which resulted in 68 Hz width resonance. The y-axis is represented in mV, which corresponds to the output of the lock-in demodulator. Calibration is necessary to convert this output into optical rotation amplitude. In-phase and quadrature components are shown in solid and dashed lines respectively.

B) using Eq. 3.1.

$$\sigma_a = \frac{\pi\hbar}{\gamma\mu_B}\frac{\Gamma}{SNR}, \tag{3.1}$$

We fine-tuned our sensor settings such as laser detuning from the D1 line, power of incident light, and modulation frequency while operating within the compact shields. This optimization process involved systematically adjusting each parameter and identifying the configuration that yielded the lowest sensitivity value using Eq. 3.1. These settings remained consistent when the sensor was moved to a noisier environment like the MSR. Our final settings were as follows: the laser frequency was red-detuned by approximately 480 MHz with respect to the $|F = 2\rangle \rightarrow |F' = 1\rangle$ hyperfine transition of the ^{87}Rb D1 line, the power of the incident light was maintained at 7 μW, and Ω_L =1.5 kHz, which corresponds to a 110 nT bias field. For this setup in FM NMOR regime typical value of the full width of the resonance was 40–50 Hz, while the SNR was $\approx$ 20,000, yielding a sensitivity of 70 fT/$\sqrt{\text{Hz}}$. The fundamental sensitivity limit of our sensor set by photon shot noise yields the intrinsic sensitivity of the sensor $\sigma_i \approx$

24 fT/$\sqrt{\text{Hz}}$ (Eq. 2.6). Comparing the level of intrinsic sensitivity of the sensor and the power spectrum of the room recordings in Fig. 3.3 it is clear that environmental noise is the dominating contribution to the actual sensitivity. In our case, the cryocooler's vibration relative to the fixed sensor was the major noise source. We would therefore expect a much better actual sensitivity in a dedicated MSR. In Fig. 3.3 we also report for comparison the noise spectrum measured with the SQUID magnetometers. Since SQUID sensors are rigidly connected to the cryocooler and have lower intrinsic sensitivity, they exhibit a lower noise floor compared to OPM.

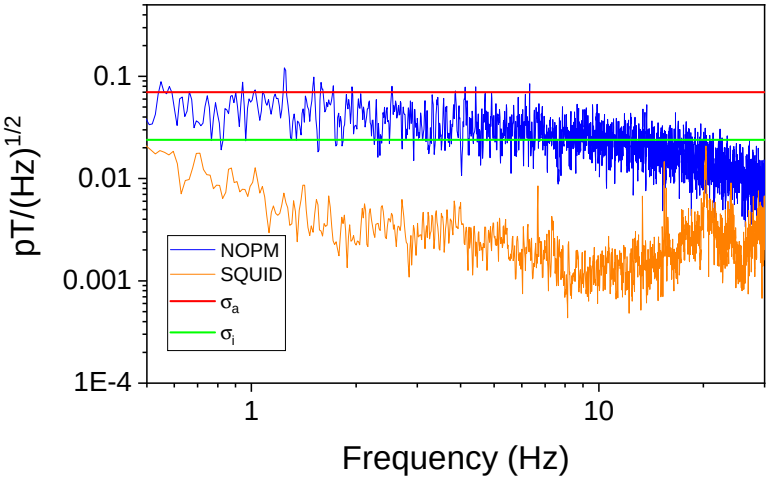

Figure 3.3: Uncorrected noise spectrum of 'empty-room' recordings for the NMOR OPM and SQUID sensors in the frequency range relevant for this work. The horizontal lines are the calculated actual and intrinsic sensitivities of the NMOR OPM sensor σ_a (red) and σ_i (green). For our NMOR OPM, the major noise source at low frequencies (< 10 Hz) is the vibrations of the MEGIN-MEG cryocooler. The SQUID sensors are not affected by such noise as they are rigidly connected to the cryocooler.

3.4.2 Detection of human auditory evoked brain

The core aim of this study was to record auditory evoked fields from a human participant, demonstrating that our OPM sensor can be used for MEG in a noisy shielded room without active field compensation.

Fig. 3.4 shows the event-related field in response to 200 tones for the NMOR OPM and the SQUID sensors respectively. In all three panels, we observe a strong deflection at 100 ms which corresponds to the N100m [145]. We conducted a paired t-test on the OPM signal, comparing

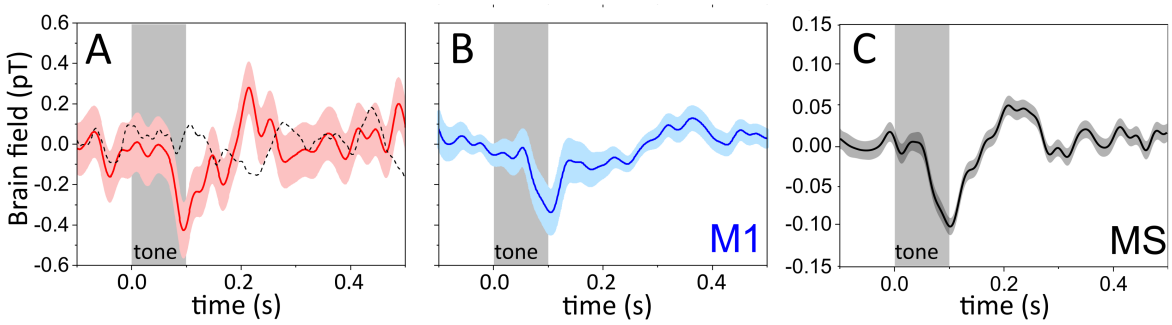

Figure 3.4: A) The auditory event-related field (ERF) measured by the NMOR OPM sensor averaged over 200 trials. Note the strong brain response at 100 ms (the response is significantly larger at 100 ms than the baseline interval; paired t-test p = 0.002) and at 200 ms (also paired t-test, p = 0.002). The shaded area indicates the standard error of the mean. For comparison, we report the trace measured during 'dummy' trials (dashed black line), where no tone was presented to the participant. B) Representative ERF trace of the Triux MEG system. This sensor ($M1$) was chosen for comparison as it provided the strongest response to the ERF. C: A trace from another sensor (MS) of the Triux MEG system chosen for the similitude with the NMOR OPM response. In this case, signal-space projection filters were additionally applied to better highlight the shape of the auditory evoked response. Note the vertical scale is smaller by a factor of 4, as the amplitude of the signal is lower than in the other panels.

the response at 100 ms to the baseline, and found a significant difference (p = 0.002). The OPM response is slightly stronger than the $M1$ response and significantly stronger than that of the MS: 427 fT against 337 fT and 100 fT respectively. This is due to the closer proximity to the scalp. The noise level of the NMOR OPM traces is higher: the average standard error of the mean for the NMOR OPM is ≈130 fT, while for the $M1$ and MS SQUIDs it is ≈60 fT and ≈11 fT respectively. Note however that for MS this performance is obtained using advanced filtering, as explained above, so it cannot be directly compared. The higher noise level in the OPM recordings is mainly due to magnetic field noise coming from the vibrations in relation to the MEGIN-MEG cryocooler. The SQUID sensors are not affected by such noise as they are rigidly connected to the cryocooler. By comparing the signal-to-noise ratio for these traces, i.e., the ratio between the amplitude of the N100m peak and the average standard error of the mean reported above, we obtain ≈3.3 for the NMOR OPM sensor and ≈5.6 for $M1$ SQUID sensor. Therefore our prototype NMOR OPM sensor delivers performance slightly lower but in the same range of those of state-of-the-art SQUIDs.

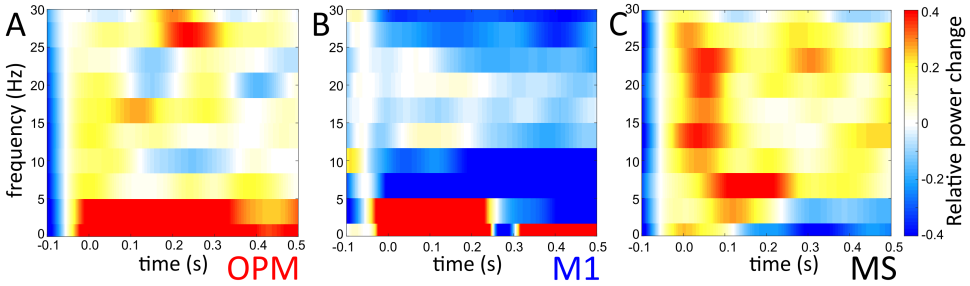

Figure 3.5: Time-frequency representation of power measured by the NMOR OPM sensor (A), $M1$(B) and MS(C) SQUID sensors in response to the tone. The colour scale indicates the relative power modulation. The power estimates were calculated per trial and then averaged. The response is relative to the baseline.

To further investigate the response, we calculated the time-frequency representation (TFR) of power for each trial of the OPM session. These power estimates were then averaged. The results are shown in Fig.3.5 A, and reveal the expected robust depression with respect to the baseline in the alpha band around 10 Hz, a few hundred ms after the tone (t-test for the power for the 10 Hz band in the full 0.15–0.7 s interval, $p \leq 0.05$). MS channel is located too far from the visual cortex and therefore does not show alpha depression (Fig.3.5 C). Note that the comparison between MS and the OPM is constrained.TFR from $M1$ is noisy (Fig.3.5 B) due to the absence of any filtering. However, if SSP or SSS filtering is applied the clear alpha depression can be seen from $M1$ and neighboring channels.

3.5 Conclusion

In this chapter, I showed the design and implementation of a modular OPM sensor based on the NMOR technique with a non-magnetic sensor head. We employed the sensor to detect auditory evoked fields in a human participant and conducted a comparison with state-of-the-art commercial SQUID magnetometers from the MEGIN system. Our NMOR OPM sensor demonstrated comparable performance, even considering the noise generated by the cryocooler. We speculate that in a dedicated, noise-reduced magnetically shielded room (MSR) like the one in [49], our sensor could potentially outperform the SQUIDs due to its closer proximity to the

scalp. Additionally, spectral analyses revealed that our OPM sensor can detect other typical brain response features, such as the reduction in alpha band activity at 10 Hz.

Overall, our NMOR OPM sensor exhibits enhanced noise resilience in comparison to zero-field OPM sensors, enabling its use in noisy MRS for example with a cryogenic cooler inside with uncompensated magnetic fields and thereby simplifying the need for additional peripheral hardware like compensation coils. Though the intrinsic sensitivity is slightly higher but of the same order of magnitude as commercial zero-field sensors, it is sufficient to reliably detect the auditory evoked response. Therefore, the NMOR technique for OPM-MEG systems appears to be a robust solution for enhancing dynamic range and noise resilience in OPM-MEG.

In the future, we plan to reduce the influence of environmental noise by designing an NMOR intrinsic gradiometer. This design will incorporate two cells and a single laser beam. With this setup, we will retain the advantages of the NMOR technique while inherently subtracting the common magnetic field between the two cells, eliminating low-frequency spatial interferences. This will further promote our sensor as a noise-resilient optically pumped magnetometer with a dynamic range extended up to geomagnetic fields.

Chapter 4

Model to optimize OPM-MEG system design for MEG applications

The material in this chapter including text, images and data has been published in the paper: Bezsudnova, Yulia, Lari M. Koponen, Giovanni Barontini, Ole Jensen, and Anna U. Kowalczyk. "Optimising the sensing volume of OPM sensors for MEG source reconstruction." NeuroImage 264 (2022). My contribution as a first author was creating a mathematical model used in the simulation, realizing it in MATLAB, analysing the results, and writing and editing the manuscript. The work was completed with great assistance from Lari M. Koponen in coding and was supervised by Anna U. Kowalczyk, Giovanni Barontini, and Ole Jensen. Most of the material in this chapter remains unchanged from the paper, others have been adapted to suit the context of this thesis.

In this chapter, I present a stand-alone OPM and OPM array model with performance metrics tailored for MEG applications. These models can serve as a toolkit for guiding the design of OPM-MEG systems in real-world environments, taking into account factors such as background brain activity and environmental noise. In this study, we used the toolkit to investigate how the dimensions of the sensing volume (the vapour cell) impact the performance of both individual OPM-MEG sensors and multi-sensor OPM-MEG systems. We demonstrate that the best overall sensitivity and reconstruction accuracy is achieved with cells that are significantly longer and

wider than those of the majority of current commercial OPM sensors. Our work provides useful tools to optimise the cell dimensions of OPM sensors and the number of sensors in an array in a wide range of environments.

4.1 Introduction

Portable and compact OPMs offer new research possibilities inaccessible to conventional SQUID-based MEG systems. For example, OPM-based systems allow studying previously unreachable biomagnetic signals [23–26]. One of the most attractive advantages of the OPMs is the possibility to place them directly on the subject's head, which results in a 5 fold increase of the measured brain signal compared to SQUIDs [6] and consequently increase in spatial resolution of the system [10]. Recent works have studied various aspects of the performance of OPM-MEG systems, trying to unlock their full potential. Investigations focused on quantifying the dependence of neuronal source localisation accuracy on the number of sensors, their layouts [66, 146–148], improvement of information content acquired with multi-axial sensor arrays, [7, 18] or accuracy of sensor positioning needed for precise source reconstruction [32, 57, 66]. Most of these works assumed fixed single-sensor response and noise models that are based on either idealized point-like sensors [6, 14, 18, 149] or sensors with arbitrary noise levels [7].

It is of capital importance to consider that neuromagnetic fields decay with the square of the distance and an OPM sensor registers the signal averaged over its sensitive volume. Therefore, a smaller sensing volume results in higher recorded signal amplitude but also higher recorded brain noise. Furthermore, the size of the sensitive volume affects the intrinsic sensitivity of the sensor. Existing OPMs have cell sizes ranging from $1 \times 2 \times 3$ mm ^{3} in chip-scale sensors [150] to bench-top sensors with 30 mm spherical cells [89]. So far, however, no exhaustive analysis has been carried out to determine the optimal sensing element dimensions for an OPM-MEG system.

In this work, we study how the dimensions of the OPM sensing element, namely its vapour cell, can be optimised depending on residual noise sources. We first concentrate on the opti-

misation of the performance of a stand-alone sensor, which can be useful for the development of prototype sensors. In this case, we determine the optimal dimensions by maximising the signal-to-noise ratio. We then consider arrays of sensors, determining their optimal sensing volume by optimising the ability of the array to localise a source and extract its time course.

4.2 Mathematical model

4.2.1 Model of the external noise

The external magnetic field noise amplitude recorded by the sensors in MEG experiments can be expressed as:

$$\tilde{N} = \sqrt{(\tilde{N}_b)^2 + (\tilde{N}_r)^2}\,, \tag{4.1}$$

where $\tilde{N}_b$ is the detected "brain noise", resulting from the background brain activity and $\tilde{N}_r$ is the residual magnetic field noise that accounts for the components of the environmental noise and sensor's technical noise that cannot be compensated for. The brain noise decreases with the distance from the head, therefore $\tilde{N}_b$ depends on the volume of the cell. The environmental noise originates from stray magnetic fields, thermal currents induced in the magnetically shielded room and vibrations of its walls, nearby electrical equipment, mechanical movement of magnetic or conductive components (e.g. elevators, urban traffic), and electrically active tissues. Such noise, generated by distant sources outside of the head, can be considered as spatially homogeneous [27]. The spatially and temporally correlated components of the environmental noise can be usually removed in data pre-processing by using various filtering methods such as signal space separation [35, 151] or with magnetic field compensation systems. Advanced coils, such as those described in [50], can attenuate the dominant components of the static background field as well as their first-order spatial gradients. Additionally, if used with feedback controllers, very low-frequency magnetic field drifts can be significantly suppressed. However, such compensation can introduce magnetic noise in other frequency bands. In addition, every OPM sensor is subject to technical noise arising from fluctuations in the laser light intensity, frequency and polarization

fluctuations, atomic cell temperature fluctuations, current noise, and other various electronic noises that can affect the magnetometer readout [36]. In our simulations, $\tilde{N}_r$ accounts for every technical and residual noise that cannot be actively or passively compensated. We additionally consider $\tilde{N}_r$ as white noise in the spectral interval 4–100 Hz [152]. In line with state-of-the-art methods like those developed in [31, 35, 153], we assume that the noise below 4 Hz is filtered out, therefore our measurement bandwidth is 5-30 Hz.

In this work, $\tilde{N}_r$ is used as a free parameter with a standard deviation ranging from 0 to 100 fT, similarly to [139].

4.2.2 Model of stand-alone OPM sensor

OPM Sensor Performance Metric for MEG

The performance of any magnetometer can be assessed by its signal-to-noise ratio (SNR),

$$SNR = \frac{S}{\delta\tilde{B}}\,, \tag{4.2}$$

where S is the signal amplitude detected by the sensor and $\delta\tilde{B}$ is the total amplitude of the recorded noise. In a perfectly shielded environment the value of $\delta\tilde{B}$ determines the sensitivity δB of the sensor in a given measurement bandwidth f_{BW}, $\delta B = \delta\tilde{B}/\sqrt{f_{\mathrm{BW}}}$. Note that the sensitivity and the amplitude spectral density have units of $\mathrm{fT}/\sqrt{\mathrm{Hz}}$ and are marked as δB_x. The noise amplitude, i.e. the standard deviation of the noise, in a given measurement bandwidth, has units of fT and is marked with $\delta\tilde{B}_x = \delta B_x \cdot \sqrt{f_{\mathrm{BW}}}$. The same notation applies to N_x and $\tilde{N}_x$. In this work, we assume $f_{\mathrm{BW}} = 25$ Hz as that is sufficient to record oscillatory brain activity in the alpha and beta band.

In real conditions, it is impossible to separate the external magnetic field fluctuations from the intrinsic noise of the sensor. Therefore, $\delta\tilde{B}$ can be expressed as:

$$\delta\tilde{B} = \sqrt{(\delta\tilde{B}_i)^2 + \tilde{N}^2}\,, \tag{4.3}$$

where $\delta\tilde{B}_i$ is OPM intrincis sensitivity and $\tilde{N}$ the external magnetic field noise amplitude.

There are two fundamental noise sources that determine $\delta\tilde{B}_i$ (Eq. 2.10): atomic-shot noise (Eq. 2.5) and photon-shot noise (Eq. 2.6). In this study, we model an NMOR sensor similar to [44], with an anti-relaxation coated vapour cell containing ^{87}Rb atoms and a SERF OPM with a single-beam configuration similar to commercial sensors [122]. The vapour cell contains ^{87}Rb atoms, Ne as a buffer gas, and N_2 as a quenching gas.

Intrinsic noise of NMOR OPM

Without a buffer gas, the atoms can travel freely in the cell and the sensing volume is $V = L \times D^2$ where L is the cell length, D^2 is the cross-section of the cell (Fig. 4.1). For such a sensor, the atomic shot-noise limit (Eq. 2.5) originates from fluctuations of the number of atoms that contribute to the signal and it depends on the finite lifetime of the light-induced atomic polarization [95]. The photon-shot noise (Eq. 2.6) is the leading contribution to the intrinsic noise. The polarization rotation noise per unit bandwidth due to quantum fluctuations is proportional to the number of photons in the probe beam N_{ph} as [95].

Both δB_{at} and δB_{ph} depend on the width of the resonance Γ, which is the inverse of the spin relaxation time [73]. The width of the resonance is determined by the sum of several relaxation rates as shown in Eq. 2.11.

The relaxation rate due to collisions between alkali atoms is given by

$$R_{se} = q(I)\sigma_{se} v_{rel} n \,, \tag{4.4}$$

where $q(I) = (6I+1)/(\pi \times (8I+4)))$ is the nuclear slow-down factor, I the nuclear spin of alkali atom, σ_{se} is the spin-exchange collision cross-section and $v_{rel} = \sqrt{2} v_{th}$ is the average atomic relative velocity with $v_{th} = \sqrt{8 k_B T / m}$, where k_B is the Boltzmann constant, T the temperature of the gas and m the atomic mass.

The wall-collision-induced relaxation rate is given by:

$$R_{wall} = C_w \frac{1}{T_c} , \tag{4.5}$$

where C_w is the probability of electron spin relaxation during the collisions with the coating of the walls and $T_c = 4V/(v_{th}S_{cell})$ with S_{cell} as the surface area of the cell.

The light-induced relaxation rate is caused by the pump light [11] and is due to transitions between Zeeman ground states. This rate is proportional to the average incident light intensity I_{mean}:

$$R_{light} = 2\frac{k_\nu}{\hbar\nu_l} I_{mean} \tag{4.6}$$

where k_ν is the microscopic absorption cross-section, $\hbar$ the reduced Planck constant and ν_l the frequency of the pumping light.

Finally, spatial field fluctuations randomly shift the resonance frequency, resulting in a broadening of the magnetic resonance lines according to

$$R_{noise} = \gamma^2 \left(\Delta B\right)^2 \frac{L}{v_{th}} \tag{4.7}$$

where ΔB is the root mean square of the magnetic field fluctuations over the length of the cell L. For a sensor similar to [44], ΔB is dominated by the bias field applied over the cell and is thus independent of the spatial fluctuations of measured signals.

Intrinsic noise of SERF OPM

For SERF magnetometer [122] atomic shot noise is given by [98]

$$\delta B_{\text{at}} = \frac{4}{\tilde{\gamma^e}}\sqrt{\frac{\Gamma}{nV}} \tag{4.8}$$

where $\tilde{\gamma^e} = \frac{\gamma^e}{2I+1}$ and γ^e is the gyromagnetic ratio of a bare electron. V is the volume corresponding to the intersection of a laser beam with the vapour cell volume $V = L \cdot D^2$, where L is

the cell length, D^2 is the laser beam cross-section area; and the photon shot-noise

$$\delta B_{\mathrm{ph}} = \frac{4\Gamma}{\tilde{\gamma^e}} \sqrt{\frac{1}{N_{\mathrm{ph}}}} \, . \tag{4.9}$$

In the SERF magnetometer, spin-exchange relaxation is suppressed. The residual magnetic width Γ is due to spin-destruction collisions R_{SD}, collisions with the walls R_{wall}, and the interaction with the light R_{pump}. With optimal pumping R_{pump} equals the sum of R_* caused by all other relaxation mechanisms. Overall the relaxation rate in SERF regime is expressed as:

$$\Gamma = R_{SD} + R_{wall} + R_{pump} + R_{noise} \, , \tag{4.10}$$

where the R_{SD} is the relaxation rate due to spin destruction is given by

$$R_{SD} = R_{SD}^{SERF} + R_{SD}^{B} + R_{SD}^{Q} \, . \tag{4.11}$$

Here the first term is due to collisions with other alkali atoms, the second term is due to collisions with buffer gas atoms, and the third term is due to collisions with quenching gas molecules. Each of these three terms can be written as

$$R_{SD}^{*} = \frac{1}{2I+1} n_* v_{rel} \sigma_{SD}^{*} \, , \tag{4.12}$$

where ^{o} denotes relevant atoms, $v_{rel} = \sqrt{8k_BT/(\pi M)}$, $M = (1/m + 1/m')^{-1}$ with m alkali atom mass, m' the relevant atom mass, n_* is relevant atomic density. The wall-collision-induced relaxation rate is given by

$$R_{wall} = D_0 \frac{p_0}{p} \left(\frac{2.4^2}{D^2} + \frac{\pi^2}{L^2} \right) \, , \tag{4.13}$$

where D_0 is the diffusion constant of the alkali atom within the buffer gas, $p_0 = 760$ Torr, p is the buffer gas pressure.

The broadening due to magnetic field fluctuations are the same for SERF and NMOR, thus R_{noise} is obtained from Eq. 4.7.

Table 4.1: Constants and parameters used in the model (1) [154], (2) [73], (3) [101], (4) [11], and (5) [98].

Common			
k_ν	$1.12 \cdot 10^{-23}$ m^2 (1)		
ν_{laser}	377 THz		
P_{laser}	$7 \cdot 10^{-6}$ W		
f_{BW}	25 Hz		
ΔB	1 nT/m		
NMOR OPM (^{87}Rb)		SERF OPM (^{87}Rb)	
γ	$43 \cdot 10^9$ Hz/T	γ^e	$1.7 \cdot 10^{11}$ Hz/T (5)
n	$8.5 \cdot 10^{15}$ m^{-3}	n	$1 \cdot 10^{20}$ m^{-3}
I	3/2	I	3/2
T	295 K	T	450 K
A_{NMOR}	$0.6 \cdot 10^{-3}$ rad	σ_{SD}^{SERF}	$1.6 \cdot 10^{-21}$ m^{-2} (5)
σ_{se}	$2 \cdot 10^{-18}$ m^2 (3)	$\sigma_{sd}^{\mathrm{Ne}}$	$1 \cdot 10^{-28}$ m^{-2} (5)
C_w	10^{-4} (4)	$\sigma_{sd}^{\mathrm{N_2}}$	$1 \cdot 10^{-26}$ m^{-2} (5)
		D_0	$0.2 \cdot 10^{-4}$ m^2/s (5)
		p_{Ne}	600 Torr
		$p_{\mathrm{N_2}}$	20 Torr

Forward model for an OPM sensor

Our signal of interest, S, and brain noise, $\tilde{N}_b$, are due to the magnetic field arising from the neural activity in the brain. This neural activity gives rise to a primary current distribution and we approximate it with a set of equivalent current dipoles (ECDs) inside the brain. We obtain the associated magnetic field from a spherical volume conductor model of the head, identical to the one in [145]. We approximate the signal S with one tangential source ECD and the brain noise with a set of independent, tangential and randomly oriented ECDs [7, 152, 155, 156].

As mentioned, an OPM produces a signal that is proportional to the mean magnetic field measured within the sensing volume [11]. For NMOR sensors, that typically use paraffin-coated cells, this volume is determined by the glass cell volume, while for SERF sensors, that employ buffer gas cells, sensing volume is the intersection between the cell volume and the probe laser

beam. Therefore the signal of interest is

$$S = \frac{1}{V}\int_V \vec{B}_{sECD}(\vec{r}) \cdot \vec{n}\, dV\,, \tag{4.14}$$

where $V = L \times D^2$ is the volume of the vapour cell with length L and the cross-section D^2, $\vec{B}_{sECD}$ is the magnetic field produced by the source ECD, and $\vec{n}$ is the measurement axis of the OPM. Similarly, the brain noise is the net signal generated by a set of randomly oriented dipoles:

$$\tilde{N}_b = \mathrm{RMS}_{100}\left[\sum_j \frac{1}{V}\int_V \vec{B}_{ECD,j}(\vec{r}) \cdot \vec{n}\, dV\right], \tag{4.15}$$

where the index j runs over the dipoles. The noise amplitude is obtained by generating 100 of such sets and calculating the root mean square of the computed sums. The modelled system is shown in Fig.4.1. The head is approximated with a conductive sphere with radius $R_{\mathrm{head}} = 91$ mm and the brain with a concentric sphere with radius $R_{\mathrm{brain}} = 80$ mm. The signal S arises from a single tangential 10 nAm dipole, and $\tilde{N}_b$ from 1000 randomly oriented dipoles (0.2 nAm each). For this model, the forward problem has a closed-form solution [157] and we obtain realistic values for the signal of interest and brain noise.

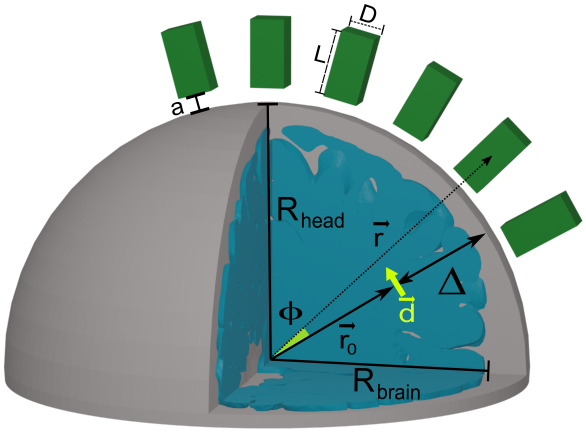

Figure 4.1: The model. The radius of the head is R_{head} and the radius of the brain is R_{brain}. An equivalent current dipole tangential to the head surface is positioned at point $\vec{r}_0$ inside the brain and has a moment $\vec{d}$. The distance between the head surface and the dipole is Δ. A sensor with a rectangular cuboid cell positioned at $\vec{r}$ is measuring a signal S from the dipole. The cuboid has length L in the radial direction and D in both tangential directions and is away from the head by distance a. The angle between $\vec{r}_0$ and $\vec{r}$ is ϕ.

4.2.3 Model of an array of OPM sensors

Metrics to assess the OPM-MEG system performance

We estimate the performance of an OPM-MEG system, consisting of an array of sensors, using its source localisation accuracy and time course reconstruction accuracy.

Localisation accuracy

We define the localisation accuracy for a single dipolar source as the volumetric error

$$\sigma_V = \sqrt{(\sigma_x)^2 + (\sigma_y)^2 + (\sigma_z)^2}, \tag{4.16}$$

where σ_i is the root mean square (RMS) error of the reconstructed dipole position in the direction i [152]. To avoid overfitting due to an exactly ideal forward model, we introduce trial-by-trial inaccuracy to sensor positions and orientations. When measuring the field and the brain noise, each sensor has a uniform random offset (RMS 4 mm) and a uniform random tilt (RMS 9°) from the normal to the head orientation, corresponding to the suggested co-registration accuracy of an OPM-MEG system by [57]. Our procedure in this case is the following:

1. we generate a random tangential ECD in a random position (Δ = 21–26 mm) and 1000 randomly oriented ECDs inside the brain.

2. we compute the signal and brain noise recorded by the inaccurately positioned sensor array (100 sets).

3. we add white residual and intrinsic noise.

4. assuming the ideal sensor locations, we reconstruct a single dipole using a dipole fitting algorithm. For each array of sensors, the localisation procedure was performed for 9 ECD dipole positions, repeated 100 times for different sensor location errors and noise $\tilde{N}$. We do maintain the correct spatial relationship between the sources and the generated brain noise.

Time course reconstruction accuracy

The ability to localise a dipolar source does not reveal the full picture of the performance of an array of sensors, as such reconstruction has very low sensitivity to uncorrelated noise. Thus, to better assess the performance, we also compute the time course prediction error E_{tot}, a metric that estimates the ability of the array to reconstruct the temporal waveform of a dipolar source using a beamformer analysis [158].

As our MEG model includes spatially correlated brain noise, we cannot use the closed-form solution of E_{tot} derived by [18]. Instead we estimate E_{tot} as

$$E_{tot} = \frac{1}{M}\sqrt{\sum_{i=1}^{M}(\hat{q}_i - q_i)^2}\ , \tag{4.17}$$

where $M = 10,000$ is the number of time points, $\hat{q}_i$ is the estimated source magnitude, and q_i is the true source magnitude at time i. Here,

$$\hat{q}_i = \boldsymbol{\omega}^\top \boldsymbol{b}_i\ , \tag{4.18}$$

where $\boldsymbol{\omega}$ is the filter to extract $\hat{q}_i$ from the measurement $\boldsymbol{b}_i$. Given that

$$\boldsymbol{\omega} = \underset{\boldsymbol{\omega}}{\operatorname{argmin}}\ \ E\left(\hat{q}_i^2\right)\ \ \text{while}\ \ \boldsymbol{\omega}^\top \boldsymbol{l} = 1\ , \tag{4.19}$$

where $E(\cdot)$ is the expected value and $\boldsymbol{l}$ is the lead-field of the source. Lead-field is a $M_{sensors}$ x 1 vector of the magnetic signal recorded by each sensor in the array from that source ($\hat{q}_i$), where $M_{sensors}$ is a number of sensors in array. In general, lead-field is a vector ($M_{sensors}$ x 3) that characterizes the distribution of the magnetic field across all the sensors in the array resulting from the unitary ECD placed with a given position and orientated along all three axes (x, y, z).

A closed-form solution is [159]:

$$\boldsymbol{\omega} = \frac{\boldsymbol{l}^\top \mathbf{C}^{-1}}{\boldsymbol{l}^\top \mathbf{C}^{-1}\boldsymbol{l}}\ , \tag{4.20}$$

where C is the data covariance matrix. We use the exact C as the sum of contributions from the source, all of the 1000 noise dipoles, N_r, and δB_i. For each dipole $\mathrm{C}^* = (q^*_{\mathrm{RMS}})^2 \cdot l^* l^{*\top}$, where q^*_{RMS} is the root mean square of the amplitude of the relevant dipole (marked with *) over time. While the contribution from all the other noise sources is given by $\mathrm{C}^* = \mathrm{s} \cdot \mathrm{I}$, where s is a standard deviation of the relevant noise term and I is the identity matrix. To reduce random variability, we show the root-mean-square value of 9 E_{tot} estimates for random source dipoles located 21–26 mm from the head surface. For each source, similarly to [18], we assume that the exact $\boldsymbol{l}$ is known.

Model of an array of OPM-MEG system

We modelled a quasi-uniform array of sensors (sensing axis in the radial direction to the head) over one of the hemispheres of a spherically symmetric head model. In this work, we define the optimum number of sensors as the minimum number of sensors that enable best localisation accuracy. Assuming that each sensor in the array has an identical sensing volume, we perform an exhaustive search over L and D to maximise the source reconstruction accuracy. For these calculations, $\tilde{N}_r$ is set to 25 fT, corresponding to N_r= 5 fT/$\sqrt{\mathrm{Hz}}$. As long as the dimensions of the sensitive volume of each sensor are much smaller than the spacing between adjacent sensors, the spatial sampling of an array of sensors [160] is limited by the sensor spacing and not by the dimensions of the sensitive volume. This greatly simplifies the problem because it is sufficient to optimise the sensitive volume to accurately reconstruct a single ECD, rather than modelling the general case of two or more partially correlated sources.

4.3 Results

4.3.1 Optimal sensing volume for a stand-alone OPM sensor

For both NMOR and SERF sensors, L is the length of the cell along the sensitive direction. For NMOR, D^2 is the cross-section of the cell, whereas, for SERF, D^2 is the cross-section of the laser beam. We impose 0.2 cm $\leqslant L_{opt} \leqslant$ 5 cm and 0.2 cm $\leqslant D_{opt} \leqslant$ 2 cm, to be compatible

with the majority of cell production processes.

We define L_{opt} and D_{opt} as optimal length and width that yield the highest value of SNR at given N_r. Our procedure to find L_{opt} and D_{opt} for a single OPM sensor is the following:

1. we generate a randomly oriented tangential source dipole at a given depth (Δ = 20–45 mm) and adjust the angle between the OPM sensing axis and the dipole ϕ (see Fig. 1) to maximise S.
2. we generate 1000 randomly uniformly oriented and positioned ECDs inside the brain.
3. we add a white residual noise N_r and intrinsic noise $\delta\tilde{B}_i$.
4. we search for the highest SNR scanning the sensor dimensions L and D.

This procedure is repeated for 100 trials. For each set of dimensions, we calculate $\delta\tilde{B}_i$ using the parameters listed in Table 4.1. All computations are performed using the FieldTrip toolbox [161] and custom MATLAB scripts (R2019b, Mathworks, USA).

We have verified that our model reproduces typical values. For an ideal noise-free point-like SQUID sensor placed 40 mm above the scalp, N_r = 5 $fT/\sqrt{\text{Hz}}$, and Δ =2.1 cm, we obtain SNR $\approx$ 1.9, which is within the range of typical MEG data [162].

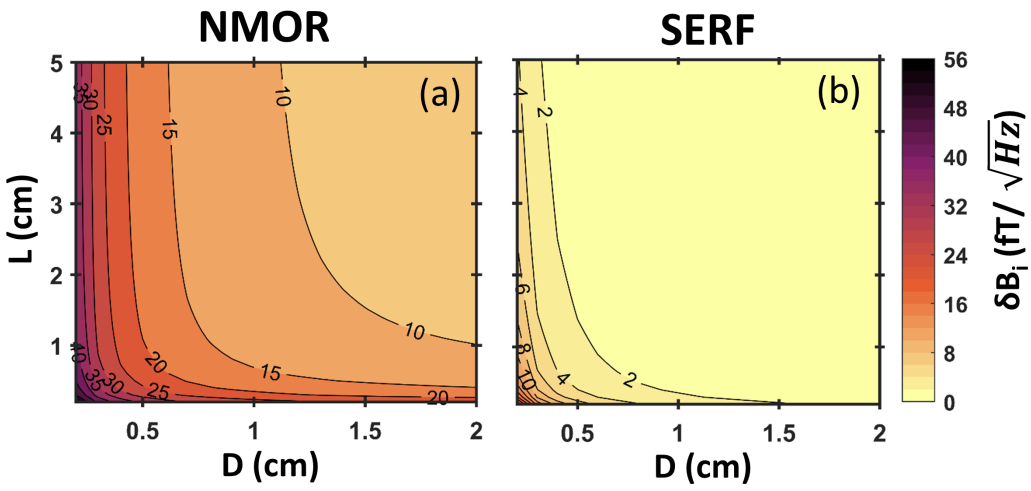

Figure 4.2: OPM intrinsic sensor sensitivity δB_i as a function of L and D of the sensing volume for NMOR (a) and for SERF (b)

Fig 4.2 illustrates how intrinsic sensitivity varies with cell dimensions for NMOR and SERF sensors. In general, both the recorded signal S and the brain noise degrade with L because the sensor is averaging over regions increasingly far from the scalp. The intrinsic sensitivity δB_i is

instead lower for larger sensing volumes. S, δB_i, $\tilde{N_b}$ decrease with different scaling with L and D.

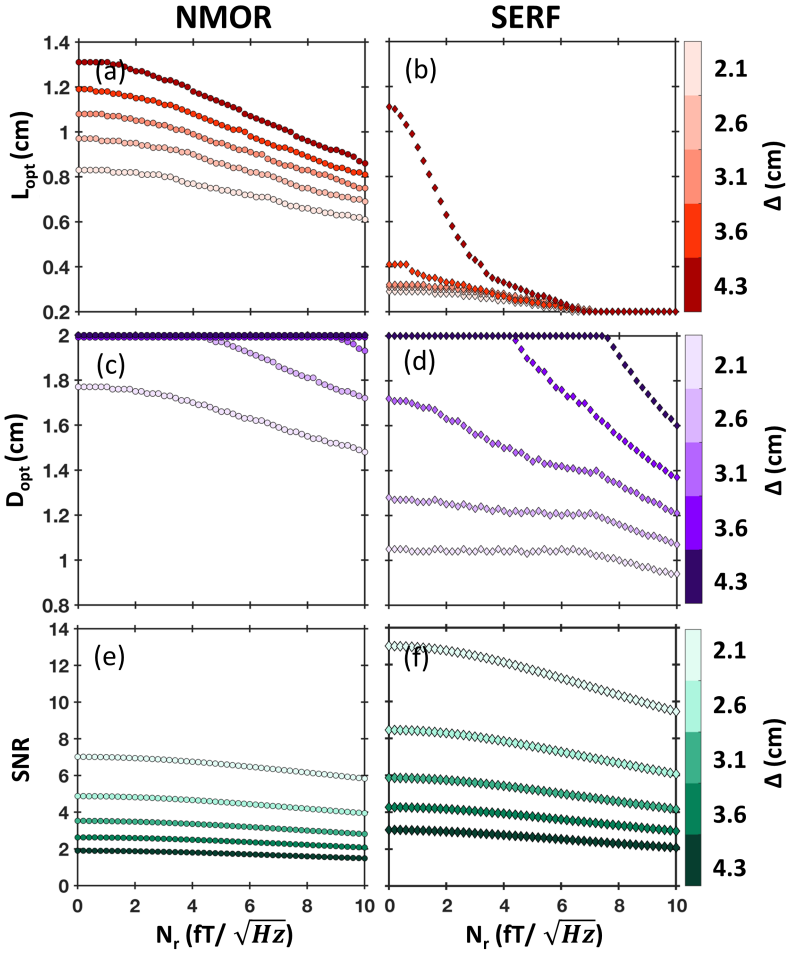

Figure 4.3: Optimal sensing element dimensions for a single OPM sensor calculated for various depths of ECD Δ, f_{BW} =25 Hz. Optimal length L_{opt} for corresponding D_{opt} as a function of residual noise N_r for NMOR sensor (a) and for SERF sensor (b); optimal diameter D_{opt} for corresponding L_{opt} as a function of N_r for NMOR sensor (c) and for SERF sensor (d); SNR for corresponding L_{opt} and D_{opt} for NMOR sensor (e) and for SERF sensor (f).

Fig. 4.3a–d shows the optimal dimensions L_{opt} and D_{opt} as a function of the residual noise N_r for few depths of the ECD Δ. For superficial sources (Δ < 35 mm), as L increases the signal decreases faster than the brain noise, and thus the optimal length varies between 0.6–1.1 cm for NMOR (Fig. 4.3a) and 0.2–0.3 cm for SERF (Fig. 4.3b). Whereas for deeper sources (Δ > 35 mm) the brain noise averages out faster than the signal of interest. Therefore, for the low-noise regime (up to 5 fT/$\sqrt{\mathrm{Hz}}$), the optimal cell length changes faster with N_r for deeper sources than

for the superficial ones. This effect is stronger for the SERF sensor (Fig. 4.3b), which has a lower intrinsic noise level. In the limit of high residual noise (10 fT/$\sqrt{\text{Hz}}$), the optimal sensor length decreases. This is because the residual noise is independent of the cell size.

The magnetic field distribution at a given distance a outside of the head is relatively smooth, i.e., the magnetic field around the optimal sensor location is approximately constant (refer to topographic maps of typical MEG data). Thus, increasing D improves the sensor's sensitivity by reducing δB_i. For example, an increase of D from 0.2 cm to the maximum allowed 2 cm reduces δB_i by 50% for NMOR and by 90% for SERF (Fig. 4.2), while keeping S and $\tilde{N}_b$ are almost constant. Overall, wider sensors ($D > 1$ cm) record higher SNR and better detect deep sources (Fig. 4.3c–d).

In Fig. 4.3e-f we show the signal-to-noise ratio SNR as a function of residual noise N_r for L_{opt} and D_{opt} for the same depths of ECD Δ. For NMOR (SERF) sensors, the best SNR is 7 (13), obtained for superficial sources in low noise environments. This decreases to 1.5 (2) for deep sources and high N_r. The lower intrinsic noise of SERF is a significant advantage in a single sensor arrangement. Note that in our simulations, the gap between the head surface and the sensing volume a is the same for both sensors. In practice, this gap might be a few mm larger for SERF since such a sensor requires hot vapour cells and thermal insulation, which will have a significant effect on SNR.

Fig. 4.3 serves as a guideline for choosing the optimal sensing volume dimensions depending on the experimental conditions if the number of sensors is very limited. Also, it illustrates that L and D have a clear optimal value corresponding to the balance point between how well each sensor is measuring the ECD and how well it is averaging the noise out.

4.3.2 Optimal number of OPM sensors

To evaluate the optimal number of sensors in an array, we carried out two sets of simulations. The first set, marked as $av = 1$ in Fig. 4.4a and Fig. 4.5 rows 1 and 2, is a real-time measurement where simulated data corresponds to a single epoch. The second, marked as $av = 20$ in Fig. 4.4b and Fig. 4.5 rows 3 and 4, simulates data averaged over 20 epochs. The epochs are generated for

each of the 100 noise and sensors location error sets. As we show later, averaging over 20 epochs reduces the noise to the level, delivering almost perfect source localisation with $\sigma_V \leqslant 4$ mm. In Fig. 4.4a–b, we show the localisation accuracy of a dipole placed at Δ=2.1 cm in the presence of residual noise N_r= 5 fT/$\sqrt{\text{Hz}}$ calculated for L_{opt} = 0.7 cm, D_{opt} = 1.7 cm for NMOR sensors, and L_{opt} = 0.2 cm, D_{opt} = 1 cm for SERF sensors. For comparison, we are also showing the localisation accuracy obtained for arrays of SQUID magnetometers. Calculations are performed for both sets, $av = 1$ (Fig. 4.4a) and $av = 20$ (Fig. 4.4b), using the procedure described in section 2.2.1. In this case, the point-like sensors are placed 4 cm from the head surface [6, 152].

To evaluate the optimal number of sensors for a time-course reconstruction, we find the minimum E_{tot} over all the possible sensors dimensions for a given number of sensors, as shown in Fig. 4.4c. In Fig. 3d and e, we report the corresponding L and D. The shaded coloured areas in Fig. 3d–e mark the range of dimensions where E_{tot} is within 5% of this minimum. For NMOR the corresponding D overlaps with the largest possible width for the considered number of sensors in an array. From our results, it emerges that for an on-scalp OPM-MEG system with optimized sensor dimensions, the optimal number of sensors in an array is about 70. This is because this is the minimum number to reach a plateau in both σ_V and E_{tot}, indicating that no significant gain in localisation is achieved by adding more sensors. This number is slightly lower than the 100 sensors required to meet the same criteria for a conventional off-scalp MEG. [152].

4.3.3 Optimal vapour cell dimensions in an array

In Fig. 4.5 we show how the source reconstruction accuracy depends on the sensing volume dimensions in the presence of brain noise for various powers of the residual noise. We perform the calculations for an array of 69 sensors. We chose this number because it is the closest to 70, which allows the algorithm we use to equidistantly space the sensors and cover the whole upper hemisphere [163]. In Fig. 4.5, column A represents a noise-free sensor in a perfect environment $\tilde{N}_r$= 0 fT. Column B shows low-noise regime $\tilde{N}_r$= 25 fT, which represents e.g. N_r = 5 fT/$\sqrt{\text{Hz}}$ at measurement bandwidth of f_{BW} = 25 Hz, conditions we chose to investigate an optimal number

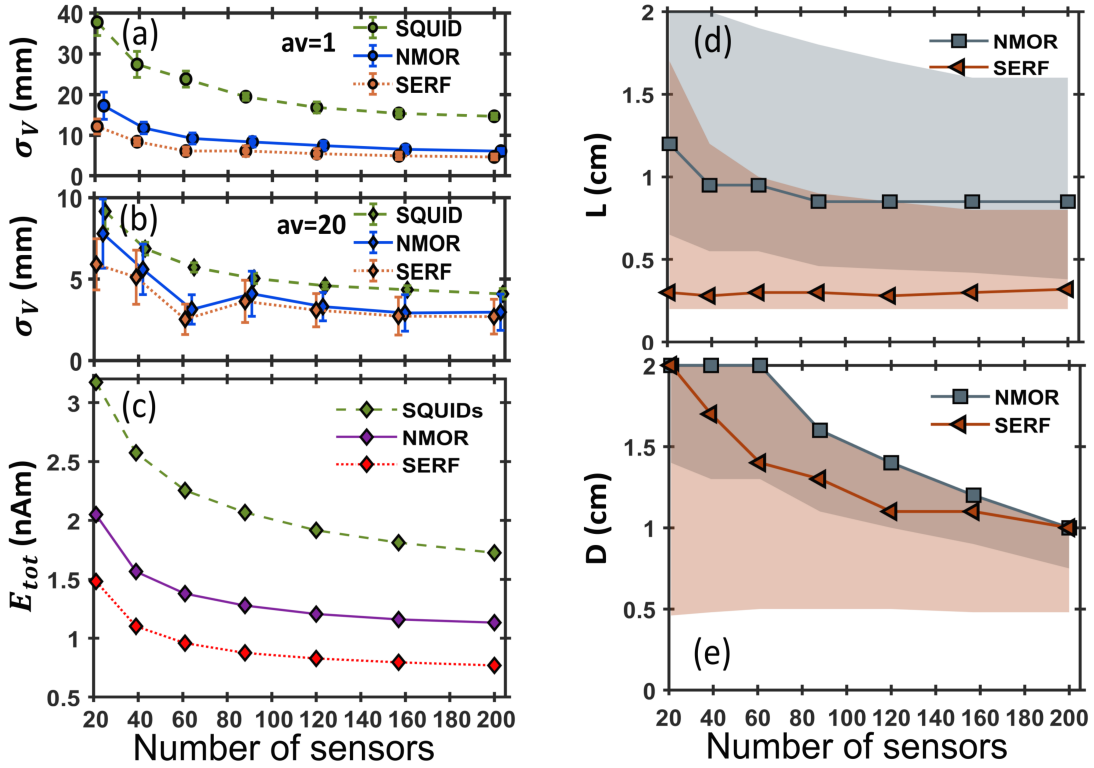

Figure 4.4: Source reconstruction accuracy of a multi-sensor array in the presence of $\tilde{N}_b$ and N_r= 5 fT/$\sqrt{\text{Hz}}$. (a–b) Localisation accuracy σ_V as a function of the number of sensors for three exemplar arrays: Blue colour is for an NMOR OPM array with sensor dimensions set to L = 0.7 cm and D = 1.7 cm, orange colour is for SERF OPM array with sensor dimensions set to L = 0.2 cm and D = 1 cm. Green colour is for SQUID-MEG system with point-like magnetometers 40 mm from the head. (a) Single time-point data av = 1, (b) averaged 20 epochs data av = 20. (c) Minimum time course reconstruction accuracy E_{tot} as a function of the number of sensors in NMOR OPM array (purple), SERF OPM array (yellow) and SQUIDs array (green). (d–e) Respectively: corresponding L and D as a function of the number of sensors. The shaded area (grey - NMOR, red - SERF) marks the range of dimensions over which E_{tot} is within 5% of its minimum.

of sensors discussed in the previous section. Columns C and D with $\tilde{N}_r$= 50 fT and $\tilde{N}_r$= 100 fT respectively represent high residual noise regime.

Fig. 4.5 rows 1 and 2 show how σ_V depends on the sensing volume dimensions in the case of real-time experiments, av=1. In the low residual noise regime (column B), the optimal dimensions are 0.2 cm $\leqslant L_{opt} \leqslant$ 2 cm, 0.7 cm $\leqslant D_{opt} \leqslant$ 1.6 cm for NMOR and 0.2 cm $\leqslant L_{opt} \leqslant$ 4 cm, 0.5 cm $\leqslant D_{opt} \leqslant$ 1.6 cm for SERF. With increasing amplitude of the residual noise (columns C and D), the optimal length decreases while the optimal diameter of the sensor increases. The optimal dimensions in this regime are 0.3 cm $\leqslant L_{opt} \leqslant$ 1 cm, $D_{opt} \geqslant$ 1.2 cm

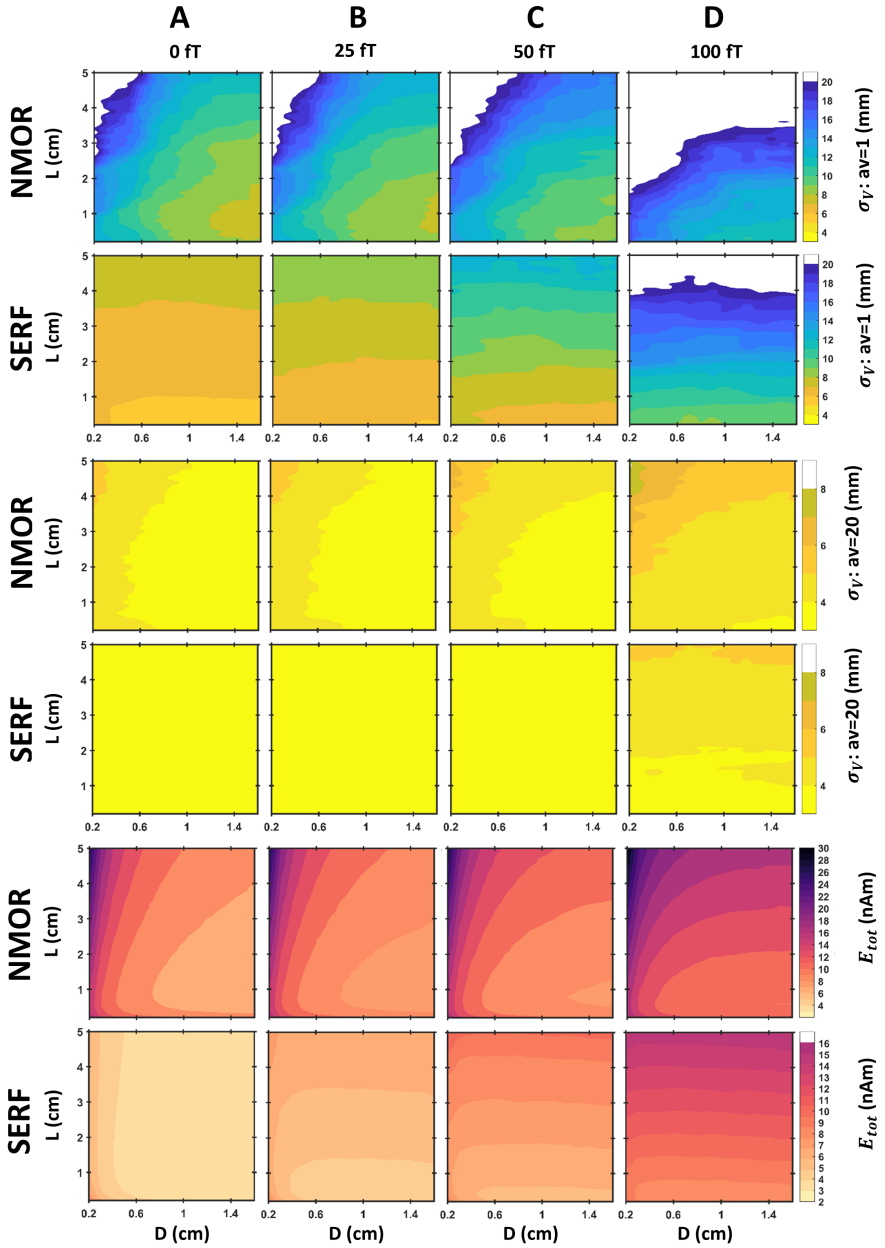

Figure 4.5: Source reconstruction accuracy as a function of L and D in the presence of brain noise $\tilde{N}_b$ with residual noise standard deviation set to $\tilde{N}_r$ =0 fT (column A), $\tilde{N}_r$ =25 fT (column B), $\tilde{N}_r$ =50 fT (column C) and $\tilde{N}_r$ =100 fT (column D). Localisation accuracy σ_V in real-time experiment (av =1) for NMOR (row 1) and SERF (row 2) sensor array. σ_V in an averaged experiment (av =20) for NMOR (row 3) and SERF (row 4) sensor array. Time course reconstruction accuracy E_{tot} for NMOR (row 5) and for SERF sensors array (row 6). White areas in rows 1 and 2 correspond to a failed source localization. Simulations are performed for an array formed by 69 sensors.

for NMOR and 0.2 cm $\leqslant L_{opt} \leqslant$ 0.6 cm, $D_{opt} \geqslant$ 0.5 cm for SERF. The white area indicates regions where the source reconstruction algorithm could not converge and the ECD could not be localised. This happens when SNR$\leqslant$1.

In the av=20 set (Fig. 4.5 rows 3 and 4), D has almost no effect on σ_V in the residual noise limit of 50 fT (columns A–C) for both types of sensors. NMOR arrays with $D > 0.8$ cm and $L <$ 4 cm, as well as all investigated SERF arrays, reach the best localisation accuracy ($\sigma_V \leqslant 4$ mm). The lower limit on the volumetric error is defined by the uncertainty in the sensors location. The geometrical errors are not affected by the dimensions of the sensor. In the high residual noise regime (column D), this limit is achieved only by SERF sensors with $L \leqslant 1$ cm and a narrow range of NMOR sensors ($D > 1$ cm and $L < 0.5$ cm). In all cases, σ_V is better for SERF since it has a lower intrinsic noise level. Considering however sensors with optimal dimensions, the difference in σ_V between SERF and NMOR is significantly reduced. In Fig. 4.5 rows 5 and 6 we show how E_{tot} depends on the sensing volume dimensions. In low noise limit For NMOR arrays, we observe a minimum for sensors with $L \approx 1$ cm and $D \geqslant 0.6$ cm. For SERF arrays, the minimum is obtained for $L \leqslant 1.3$ cm and $D \geqslant 0.4$ cm. For higher residual noise with a standard deviation of 50 fT, E_{tot} is stronger for $D > 1.2$ cm and 0.5 cm $L < 1$ cm in the case of NMOR and for $D > 0.5$ cm and $L < 0.5$ cm in case of SERF. When the residual noise becomes higher than the intrinsic noise level of the sensor, the dependency of σ_V and E_{tot} on the sensor diameter is lifted and the best performance is obtained with the shortest cells.

Our results show that OPM sensors achieve the best performance when the width of their sensing volume is the maximum allowed by the constraint of filling the whole head surface. For both sensor types, the smallest sensors have better localisation accuracy, but relatively weak time-course reconstruction. In summary, NMOR and SERF arrays perform best when their sensing elements have $L_{opt} \approx 0.2$–1 cm and $D_{opt} \geqslant 1$ cm for NMOR $D_{opt} \geqslant 0.6$ cm for SERF. This stands for real-time and averaged data.

4.4 Discussion

In this work, we presented a model to optimise the dimensions of the sensing volume of an OPM sensor for MEG. This optimisation yields the sensing volume that delivers the best performance in a realistic scenario where both residual noise and background brain activity are present. Our model can be used as a toolkit for optimizing the design of optically pumped magnetometers in given experimental conditions. Our results show that the dimensions of the sensing element are a significant parameter to take into account while designing single OPMs or whole-head OPM-MEG systems.

Our simulations demonstrate that the optimal size of a single sensor is similar to the optimal size of a sensor in an array. This can be understood considering that the magnetic field pattern produced by an ECD outside the head features two extrema, whose magnitude and spatial distribution depend on the ECD position and orientation. Usually, only a few sensors in the array cover the area of these maxima. Thus, the sensors required to form an optimal array have dimensions roughly similar to those of a stand-alone sensor. However, even if arrays with very few sensors can record the signal of interest with good SNR, they will not perform well in source reconstruction experiments (as one can extrapolate from Fig 4.4 a–b). To effectively sample the brain signal and avoid the aliasing of noise coming from non-compensated sources, larger arrays are needed. Our simulations show that the optimal number of sensors in an array is around 70. Such an array reaches the best reconstruction accuracy and can directly quantify the topography of the magnetic fields produced in the brain as well as perform analysis of the recorded signals at the sensor level.

It is worth noticing that most of commercial OPM sensors have cubic cells with a side of 0.2-0.3 cm and operate in SERF regime. The intrinsic noise level of commercial sensors is calculated to be around a few $\mathrm{fT}/\sqrt{\mathrm{Hz}}$. The actual sensitivities ($\approx$10 $\mathrm{fT}/\sqrt{\mathrm{Hz}}$) are usually not limited by fundamental noise sources, but rather by technical noise sources [36]. Columns C and D are the closest to representing such conditions in the measurement bandwidth of f_{BW} = 25 Hz or f_{BW} = 100 Hz respectively. According to our model, such sensors work well for reconstructing the location of the ECD in an offline experiment, where there is a number of trials to average

out the noise, but can improve the performance for the time-course of the ECD or in real-time experiments. In the low noise limit the change from 0.2 cm to 1.6 cm in the width of the cell results in a 2-fold increase in the ability to extract the time course and the same increase in localization accuracy for single-trial experiments. Our simulations show that the dimensions of the sensor's sensitive element are an important parameter to consider. Such optimisation has the potential to further improve the gain OPM-MEG systems have over conventional SQUID-MEG. Increasing the width of the cell in the range of diameters investigated in this manuscript has no significant effect on spatial frequency sampling or spatial resolution. [1] Therefore, the main downside of large sensor arrays can be bulkier and heavier helmets are less ideal for wearable MEG systems.

Overall, SERF sensors deliver better performance because they have lower intrinsic noise levels than NMOR sensors in similar conditions. However NMOR sensors can operate in higher magnetic field environments, have higher dynamic range, and are more resilient to external field fluctuations. Furthermore, the vapour cell of the SERF sensor needs to be heated to $> 120^{\circ}$, while NMOR sensors work at room temperature so the cell can be brought even closer to the scalp.

Note, that residual noise $\tilde{N}_r \geqslant 50$ fT eliminates both the advantage of SERF over NMOR and the advantage of large sensing volumes over small sensing volumes in terms of the intrinsic noise level of the sensor. This effect is illustrated in Fig. 4.5 columns C and D. Furthermore, due to averaging the noises out both cell dimensions and the type of OPMs have little influence on localization accuracy (rows 3 and 4).

Our results highlight the role of brain noise, which dominates the residual noise present in a typical magnetically shielded room. Furthermore, we observed that a minimum of about 70 sensors are needed to reach best localisation accuracy independent of the sensor's cell size and sensor type. This result is in line with the earlier hypothesis claiming that the sensor spacing should be comparable to noise correlation distance [152]. Note that without the correlated brain

[1] We have computed the lead-field matrix from 1000 independent dipoles for an array of 69 sensors. For each sensor diameter, we have computed a singular value decomposition of the lead-field matrix and looked at how the total spatial variability of a lead-field is explained by such an array. The difference in the curves calculated for different sensor diameters was negligible in the considered range (2mm to 16 mm).

noise included in the model, the localisation accuracy is constantly improving with an increasing number of sensors [147, 149, 152].

Our model could be expanded to optimise any other parameter that was fixed in our numerical simulations, such as the intensity of the laser beam, the atomic density or the gap between the sensor and the head. In future work, it is also desirable to refine the signal and brain noise models. For example, one could replace the spherical head model with a more realistic brain-shaped model derived from MRI scan. It would be also interesting to investigate arrays of tri-axial sensors that offer better intrinsic cancellation of the external noise sources [18]. However, in this case, a more sophisticated model for external noise is required. Ultimately, an actual recorded noise could be used to refine the optimal sensing volume dimensions.

Chapter 5

Design considerations for an array of magnetometers optimized for MVPA

The material in this chapter including text, images, and data has been published on bioRxiv [69] and submitted for publication in the Journal of Neuroscience Methods "Optimizing magnetometers array and pre-processing pipelines for multivariate pattern analysis" by Yulia Bezsudnova and Ole Jensen. My contribution to the study as a first author was developing methodology, conducting experiments, analysing data, and drafting and editing the manuscript. The research was conducted under the supervision of Ole Jensen. The results were already presented as a poster at the WOPM2023. Some of this material remains largely unchanged, while others have been made more appropriate for the thesis.

Multivariate pattern analysis (MVPA) has proven an excellent tool in cognitive neuroscience for identifying representational-specific neuronal patterns using EEG and MEG. Likewise, it also holds a strong promise when applied to OPM-MEG data. In this chapter, I explore the OPM-MEG system design for MVPA in terms of noise reduction of external sources and the optimal number of sensors for effective MVPA. We found that the use of signal space separation (SSS) aimed at projecting out the noise contributions not generated by the brain, significantly lowered the classification accuracy considering the 102 magnetometers. Therefore, we advise against SSS filters for magnetometers when performing MVPA. Instead, we recommend employing noise

reduction techniques like signal-space projection, independent component analysis (ICA), or third-order gradient noise reduction based on reference sensors to enhance MVPA performance. We also tested how many magnetometers were required for multivariate pattern analysis. We find that classification accuracy did not improve when going beyond 25 sensors, however, this saturation is specific to the classification problem discussed in the chapter.

5.1 Introduction

Multivariate pattern analysis (MVPA) is an established methodology for functional MRI, MEG, and EEG. MVPA operates by classifying the spatial distribution of brain activity associated with representing different object classes or experimental conditions [164–168]. If spatial patterns of brain activation successfully predict condition or stimulus category, it implies the presence of relevant information related to the experimental manipulation within the neuroimaging data. This property facilitates a crucial connection between theory and data. Furthermore, applying MVPA in the context of representational similarity analysis (RSA) allows to fuse the data from BOLD measures obtained from fMRI and electrophysiological data obtained from EEG/MEG, leading to an enhanced understanding of the brain's spatio-temporal properties in relation to neuronal responses [169–173]. Overall, MVPA applied for classification approaches and RSA is a powerful tool for cognitive neuroscience widely used to study object recognition [174–178] or other cognitive brain functions like prediction, spatial navigation, memory and emotions [179–184].

This study lays the groundwork for exploring the potential benefits of utilizing on-scalp optically pumped magnetometer based magnetoencephalography (OPM-MEG) in experiments designed for MVPA.mThere are two main reasons why MVPA stands to benefit from OPM-MEG systems. First, OPMs can be put directly on the subject head and therefore the magnitude of the MEG signal is stronger compared to the signal obtained by SQUID-MEG systems [4, 8]. Second, the sensors can be arranged in an array that better captures the spatial characteristics of the brain signal [7, 18, 147]. As a result, OPM-MEG potentially has higher sensitivity and

better spatial resolution than conventional MEG systems, which is beneficial for MVPA [33]. While OPM-MEG is still in its early stages of development and specific engineering challenges have to be solved, a study conducted by [10] demonstrates the theoretical capability of a dense OPM array to effectively resolve multiple independent electrophysiological sources to a degree currently achievable only using an invasive technique.

Notably, conventional MEG studies typically involve the analysis of gradiometers due to their lower sensitivity to external noise sources [185]; however, the current OPM-MEG systems utilize only magnetometers [61]. Therefore, to pave the way for optimizing MVPA used with OPM-MEG, this study focuses on data obtained from a conventional MEG magnetometer array. Specifically, we explore appropriate noise reduction techniques for magnetometers and investigate the optimal number of sensors required to achieve adequate MVPA performance.

5.2 Methods

5.2.1 Experimental paradigm

In this study, we investigated the time course of the emergence of semantic representations using picture stimuli employing MVPA applied to conventional SQUID MEG data.

Thirty-eight healthy native English adult participants took part in the study. Five participants were excluded due to excessive noise in the data, two participants were excluded due to poor performance (>15% wrong answer), therefore the final data set consists of recordings from thirty-one participants (mean age ± SD = 21.77 ± 3.31; 21 females). The study was conducted at the Centre for Human Brain Health. The University of Birmingham Ethics Committee approved the study. Participants were compensated with credits or a monetary reward.

The stimulus set was composed of 48 objects. The objects were organized as in [186] according to three types of categories, each divided into two divisions: size (big/small), movement (moving/still), and nature (natural/man-made). Each object in the study belonged to each of the dimensions (Fig. 6.1 e.g. a book is small, still, and man-made). The stimulus set was balanced such that each categorical division included one-half of the stimulus set (24 objects).

Hence each set of categories (e.g. big, still, natural) included 6 objects. The selection of categorical divisions in this study was based on previous findings demonstrating reliable neural representations of semantic dimensions across categories [187, 188]. For other purposes not to be analysed here, each object is presented in two modalities: written words and pictures. The size of the images was 400 x 400 pixels. Prior to the object presentation, the fixation cross was shown for 0.5-0.7 s. Each object was presented for 0.6 s. The experiment was divided into 9 blocks where either the succession of words (5 blocks) or images (4 blocks) was presented. After each block, a participant had a break. Each stimulus was present 4 times in a block. We used a two-alternative forced choice task (question trial) that used stimuli from the other modality than the current block. As such a participant had to identify the correct picture during the written words and vice versa. This was designed to maintain participant engagement and to encourage deep processing of stimuli in a cross-modal manner. Note that in each block the question trial was applied for every unique object once and alternative choices were unique as well. The design is shown in Fig. 5.1.

In each block, a randomly selected stimulus was presented on a grey screen at a visual angle of 6°. The stimuli presentation is implemented in Matlab using the Psychophysics Toolbox [189].

5.2.2 MEG recording

MEG data were recorded using a 306-sensor TRIUX Elekta Neuromag system, consisting of 204 orthogonal planar gradiometers and 102 magnetometers, with online band-pass filtering from 0.1 to 330 Hz and a sampling rate of 1000 Hz. Prior to data acquisition, the locations of three bony fiducial points (nasion, left and right preauricular points) were digitized using a Polhemus Fastrack electromagnetic digitizer system. Additionally, four head-position indicator coils (HPI coils) were digitized: two on the left and right mastoid bone and two on the forehead, spaced at least 3 cm apart. To facilitate the spatial co-registration of MEG source analysis with individual structural MRI images, a minimum of 400 extra scalp points were acquired for each participant. Following these preparations, participants were positioned upright with a 60° angle

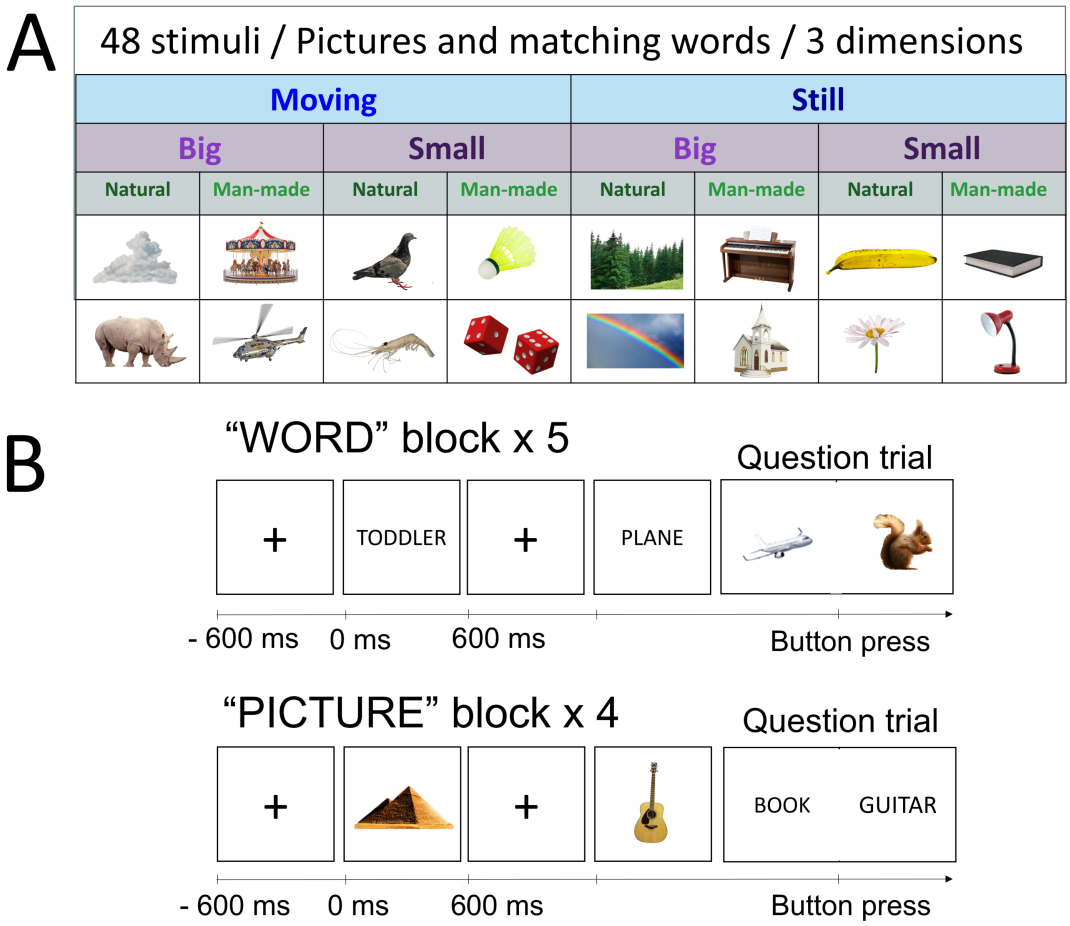

Figure 5.1: Experimental paradigm. A) The stimulus set is comprised of 48 objects which can be divided according to 3 dimensions (”size”: big/small; ”movement”: still/moving; ”nature”: natural/man-made). B) In both image and word blocks, participants were presented with stimuli in random order. In the picture block, participants viewed images of the objects, while in the word block, they read the corresponding words. The task (question trial) was presented randomly every fifth trial on average. Participants were required to identify whether the picture or word corresponded to a previously seen stimulus and press the appropriate button accordingly. When pictures were presented the probe question was presented as a word and vice versa.

backrest under the MEG gantry. To record the horizontal electrooculography (EOG), a pair of electrodes was attached approximately 2.5 cm away from the outer canthus of each eye. To record the vertical EOG, a pair of electrodes was placed above and below the right eye in line with the pupil. The ECG was recorded from a pair of electrodes placed on the left and right collarbone.

5.2.3 Standard data processing pipeline

Only data from viewing picture blocks was used in this study. The data was analyzed using the open-source toolbox MNE Python v0.24.0 [190] following the standards defined in the FLUX Pipeline [191]. The standard MVPA pipeline for a conventional MEG consists of the following steps.

First, blinks and muscle artefacts are annotated using EOG channels and magnetometers' recordings respectively. A semi-automatic detection algorithm was utilized to mark sensors with excessive artefacts (on average 4.5 sensors per participant). Then, the data was low-pass filtered at 100Hz to reduce HPI coils artefacts.

As a next step, conventionally, Signal-Space Separation (SSS) and Maxwell filtering are applied to reduce magnetic artefacts from the environment. The SSS method is a spatial method that transforms electromagnetic multichannel data into uncorrelated basic components, e.g. magnetic multipole moments and reconstructs the data using only those moments originating inside the brain. The origin, e.g. brain-related or external interference signals, of these magnetic field components is defined based on sensor geometry and Maxwell's equations only. All external origin components are dropped such that the signal is reconstructed mainly from the brain-related components [192]. Maxwell filtering is a related procedure that removes the higher-order components of the internal subspace, which are mainly dominated by sensor noise. Typically, Maxwell filtering and SSS are performed together (in MNE-Python they are implemented together in a single function) [190]. From here on, we will refer to this step using the term "SSS filtering" or SSS. While SSS significantly reduces noise from interfering sources, it results in a substantial rank reduction of the data, typically from hundreds of dimensions to a significantly lower number (from about 306 to 65 dimensions for a typical MEGIN system) [151].

As mentioned in the introduction, this study is focused on finding appropriate noise-reduction techniques for magnetometers. The alternative method to SSS filtering to reduce environmental noise is the signal-space projection (SSP) technique [193]. SSP relies on the fact that the magnetic field distributions generated by the sources in the brain have spatial distributions

sufficiently different from those generated by external noise sources. SSP operates by detecting characteristic sensor topographies related to specific artefacts, typically based on a prior principle component analysis of empty room recordings, and subsequently generating spatial projectors to effectively eliminate the influence of these artefact-related topographies from the data [194]. This procedure typically reduces the rank of the data by about 8 components.

The next step in the standard MVPA pipeline is an Independent Component Analysis (ICA) algorithm is applied [195] to remove components associated with cardiac artefacts and eyeblinks. However, we excluded this step in this work to examine how various filtering methods affect classification accuracy.

Then the data is segmented into trials. Trials corresponding to the same stimulus are averaged together to construct "supertrials". This step again increases the signal-to-noise of the data [170, 196].

For this study, we applied a highpass filter of 0.1 Hz and downsampled the data to 500 Hz. Epochs are cropped to 100 ms before stimuli onset and 700 ms after. Each time point was represented as a 306-dimensional vector (channel data). We expanded this vector by adding past 25 ms (12 time points) and future 25 ms (12 time points) of data, resulting in a 306x25 dimensional feature vector representing each time point. This procedure (termed "delayed embedding") resulted in a more information-rich representation of the neural activity associated with a given stimulus by incorporating more time points [197–199]. This feature vector was then used in the classifier. Note that extraction of specific types of sensors happens after supertrials are created.

Multivariate pattern analysis was applied to the pre-processed MEG data to classify the categories of the presented objects. Prior to classification, the data was standardized by removing the mean and scaling to unit variance per sensor. Subsequently, we employed a support vector machine (SVM) [200] from the Python module Scikit-learn [201] to classify the data over time. The classification procedure relied on a 5-fold cross-validation approach, and the performance was quantified using the area under the curve (AUC) metric of a receiver operating characteristic curve (ROC), which measures the classifier discriminative ability. Employing 5-fold cross-

validation enhances the reliability of SVM classifier evaluation by iteratively partitioning the dataset into training and testing sets. Since the whole dataset is used for training and testing, the risk of overfitting or underfitting is reduced. The ROC-AUC metric, employed within each fold, further refines the evaluation by quantifying the classifier's ability to distinguish between two equivalent categories across various decision thresholds. These techniques together produce a reliable and generalizable model for binary classification tasks with an equal number of instances in each category.

5.2.4 Number of channels

We also asked how many magnetometers are needed to get good classification accuracy results. We randomly selected an equally distributed set of N magnetometers from the existing pool of 102 sensors, using the Euclidean distance as a criterion. The data from selected channels are then fitted to the classifier. N was varied from 7 to 102 with step 5.

To explain the minimal number of sensors sufficient for the classification we examined the spatial distribution of the neurophysiological basis of the task-relevant signal by computing the topographical activation patterns back-projected from the classifier weights using the method described in [202]. Activation patterns show how the extracted signal is encoded in the features that are used by the classifier.

5.3 Results

This study was designed to examine appropriate noise reduction methods for magnetometers and determine the optimal number of sensors required to achieve adequate MVPA performance. This investigation sets the groundwork for potential future studies utilizing OPM-MEG system.

The study is based on conventional SQUID-MEG data recorded when participants were looking at pictures of objects from different categories: size (big/small), movement (still/moving), nature (natural/man-made; see Fig. 5.1). We compared the MVPA classification accuracy curves for different pre-processing pipelines. The pipeline labelled as "SSP" employed the SSP

algorithm for noise reduction without the use of any bad channel rejection. The "SSS filter" pipeline used the SSS filter as it is implemented in the MNE Python package [190]. The pipeline labelled as "raw" did not involve any noise reduction algorithms.

Unlike gradiometers, which attenuate noise from distant sources by measuring the spatial gradient, magnetometers measure the absolute magnetic field and thus are highly susceptible to environmental noise. Consequently, the application of SSS filter or SSP filter that reduces external artefacts in the data substantially impacts magnetometer recordings. Fig. 5.2 shows the power spectra of magnetometer data before and after applying SSS and SSP filters, demonstrating a notable reduction of environmental noise particularly in the magnetometers recordings.

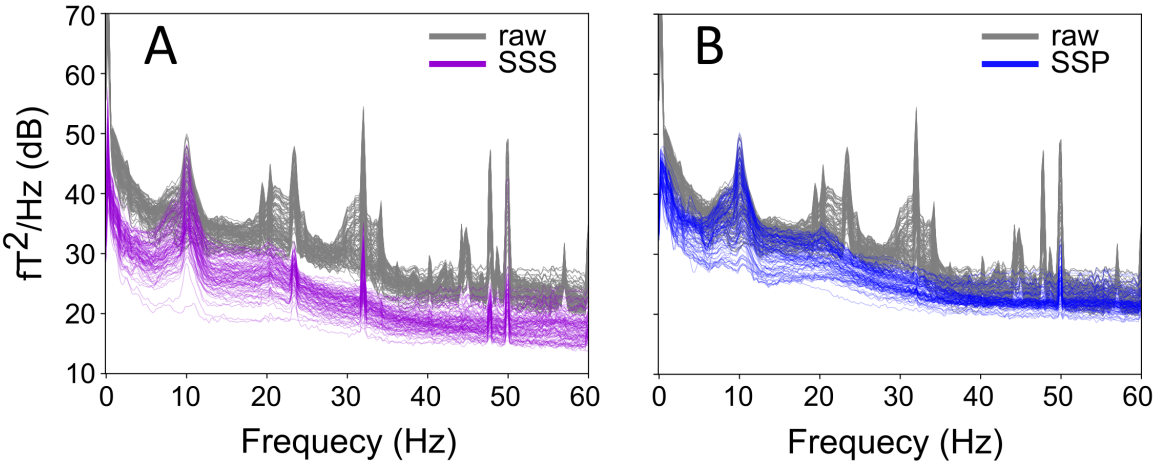

Figure 5.2: Power spectra of the magnetometer data. The grey lines represent the spectra prior to the application of noise reduction algorithms. A) The magenta lines depict data after the application of "SSS". B) The blue lines depict data after application of "SSP".

5.3.1 MaxFilter does not benefit MVPA

Fig 5.3A shows the MVPA classification results as a function of time for the different pre-processing pipelines. We find that the use of the SSS filter significantly reduces the classification accuracy considering the 102 magnetometers, whereas the filter ("raw") and the SSP filter demonstrate similar results. Fig 5.3 B shows the comparison of the area under the curve value for "SSS" and "raw" conditions calculated from 150 ms to 450 ms after stimulus onset for each participant. This time interval is chosen to capture when the brain processes and encodes

relevant information about the object category. It is evident from Fig. 5.3 that for 77% of the participants, classification is higher in the "raw" compared to the "SSS" condition. A paired t-test performed on the averaged classification accuracy (150 – 450 ms) to compare "raw" and "SSS" conditions yields a significant result (t(30) = 3.448, p = 0.002). "SSS" and "SSP" also show significant differences (t(30) = 2.785, p=0.009). A t-test performed on the mean classification accuracy for "raw" and "SSP" conditions within the same time interval is not significant (t(30) = 0.856, p = 0.398).

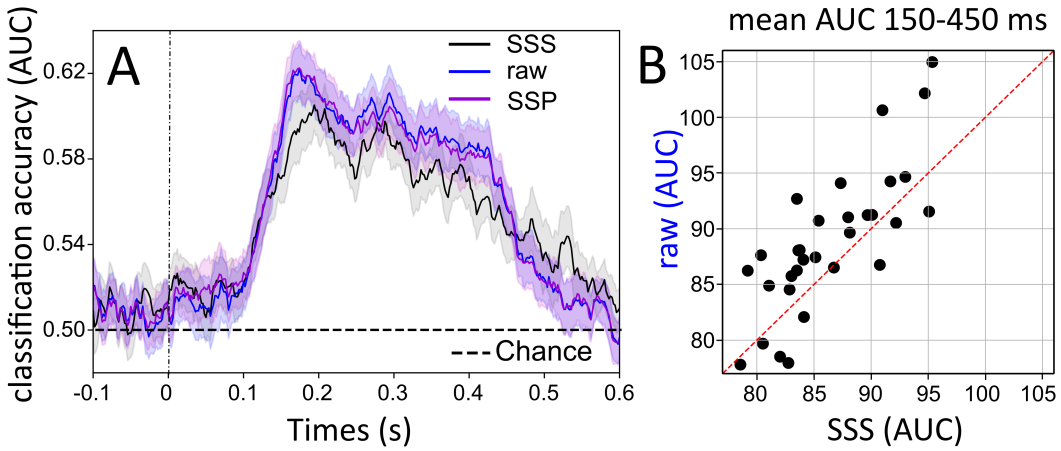

Figure 5.3: A) The time course of object categorization during image presentation for the unfiltered magnetometer ("raw") is shown in blue. The "SSS" filter is shown in black land "SSP" is shown in magenta. The highlighted area reflects the standard deviation error, while a dashed line signifies the chance level; B) Dots on the graph are the averaged AUC (150-450 ms) of the decoding curve for an individual subject. The comparison is made between the "raw" pipeline (y-axis) and the "SSS" pipeline (x-axis).

On the contrary, the application of the SSS filter does not lead to a significant decrease in MVPA classification when utilizing the 204 planar gradiometers (Fig. 5.4A) or all 306 sensors combined (Fig. 5.4B).

5.3.2 Magnetometers and Gradiometers

After optimizing the pre-processing pipeline, we compared the performance of 102 magnetometers and 102 gradiometers (no filter was applied). On each sensor location, one of two planar gradiometers was selected randomly. The results shown in Fig. 5.5 demonstrate similar

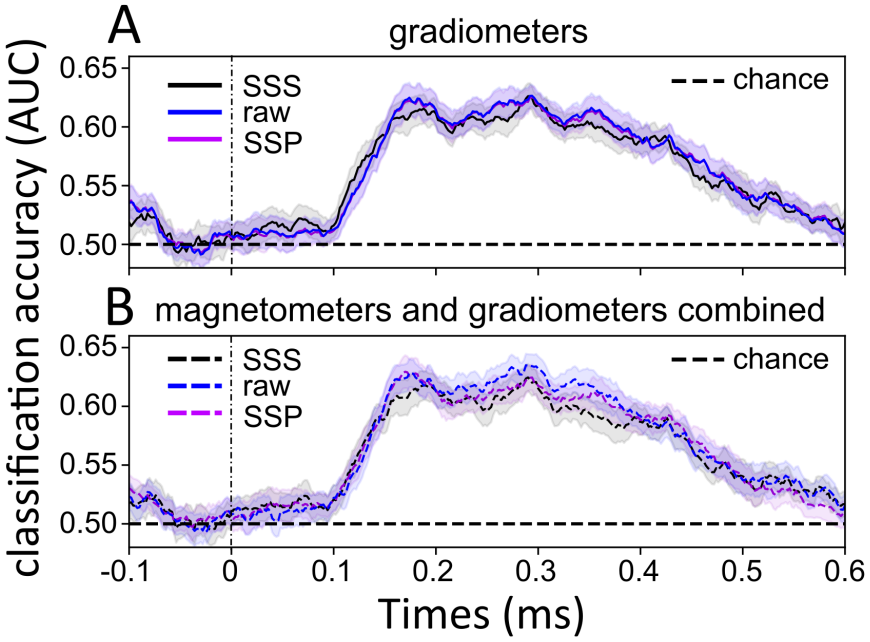

Figure 5.4: The time course of object categorization during image presentation for the unfiltered data ("raw") is shown in blue. The SSS filter is shown in magenta. A) The gradiometers data only. B) The magnetometer and gradiometer data combined. The highlighted area reflects the standard deviation error, while a dashed line signifies the chance level.

performance for two types of sensors. No significant difference was found. The comparison of the AUC also showed no difference in accuracy between magnetometers and gradiometers. We conclude that when optimizing a MEG system for multivariate analysis, gradiometers and magnetometers work equally well.

5.3.3 Number of sensors

Finally, we investigated the impact of the number of sensors on MVPA classification accuracy. We assessed the classification performance using the area under the curve metric across 150 – 450 ms after a stimulus was presented. Fig 5.6 illustrates the relationship between AUC of classification as a function of a number of magnetometers (not using SSP or SSS condition). We observe that classification saturates at about 25 sensors. This saturation is specific to the classification problem discussed, which can be seen from activation patterns in Fig 5.6 B. The activation patterns averaged over 150-450 ms show a simple structure of approximately

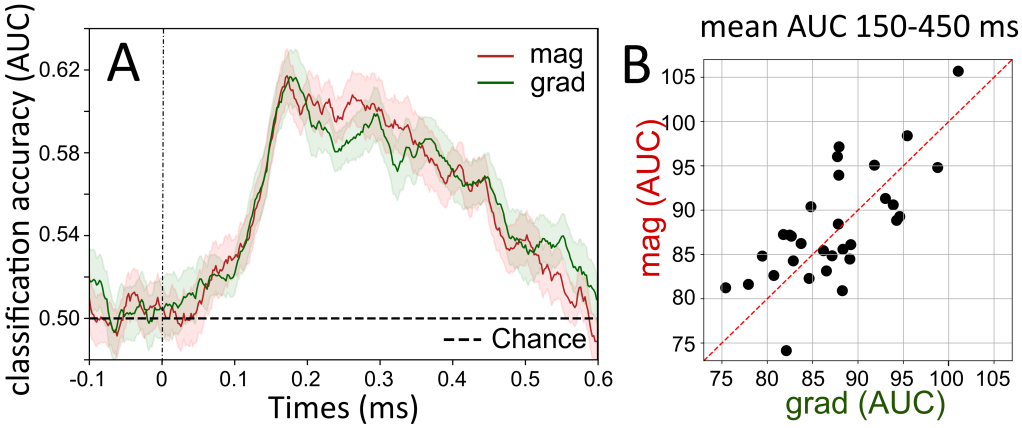

Figure 5.5: A) The time course of object categorization during image presentation for 102 gradiometers (green line) and for 102 magnetometers (red line). The highlighted area reflects the standard deviation error, while a dashed line signifies the chance level. B) Dots on the graph are the averaged AUC (150-450 ms) of the decoding curve for an individual subject. The comparison is made between classification results for magnetometers (y-axis) and gradiometers (x-axis). No difference was observed.

two dipoles that do not need all 102 sensors to characterize its spatial distribution. A similar sensor-level topographical map obtained with a different approach can be seen in [178].

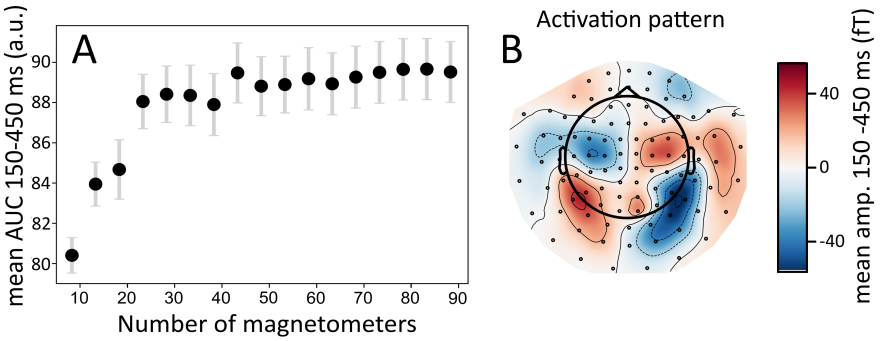

Figure 5.6: A) AUC of the decoding curve over time interval 150-450 ms after stimulus presentation is plotted as a function of the number of sensors in the magnetometer array. B) Topographical activation pattern reconstructed from classifier weights calculated for 102 magnetometers averaged over 150-450 ms after stimulus presentation.

5.4 Discussion

We explored various noise reduction techniques for conventional MEG data in the context of MVPA analysis. The results demonstrate that the use of the SSP filter for denoising or no filter at all yields a significantly higher classification accuracy compared to when using the SSS filter. We also find there are no differences in classification accuracy when comparing a 102-magnetometer array to a 102-gradiometer array. Moreover, we show that employing only 25 magnetometers evenly distributed over the head is sufficient to achieve classification accuracy comparable to a 102-magnetometer array for picture category classification.

Based on our results we do not recommend using SSS filter in OPM-MEG data when conducting MVPA. The implementation of SSS filters results in a significant reduction of the SVM classification accuracy when considering SQUID magnetometers. We attribute this decline in performance to the substantial rank reduction from 306 to ~65 induced by the SSS filtering. This procedure may result in the exclusion of informative data important for classification based on MVPA. Since the classification curves with and without the SSP filter show no significant difference, we can conclude that noise artefacts do not impact classification accuracy in a "raw" condition.

Our results show that only magnetometers are significantly affected by the SSS filter, and we conclude that informative magnetometer data are attenuated by this method. No negative significant effect of SSS filtering was found when considering gradiometers or magnetometers and gradiometers combined (Fig. 5.4). In summary, to optimize noise reduction in MVPA for OPM-MEG system, we recommend considering methods such as SSP. However other approaches such as ICA or 3rd-order gradient noise reduction might also be efficient [185]. Note that 3rd-order gradient noise reduction requires a reference sensor array.

It is interesting that similar MVPA performance is observed between comparing arrays of magnetometers and gradiometers [13, 203]. This could be explained by the fact that with 100 sensors, located 3 cm away from the brain, both gradiometers and magnetometers record sufficient information. As such, choosing between magnetometers and gradiometers does not seem to be a design consideration when optimizing an MEG system for MVPA.

We showed that even with a relatively small number of magnetometers (25) in the array, the MVPA classification accuracy reaches saturation. This plateau can be attributed to the low spatial frequency structure of the activation pattern corresponding to a classifier weight. The fact that a reduction from 102 to 25 sensors results in good classification accuracy considering that the rank reduction from 102 to 65 components by SSS reduced classification accuracy suggests that the SSS filter removed informative data components related to object representation. Based on these findings, we suggest that when designing an OPM-MEG system for picture categorization using MVPA, 25 magnetometers may be sufficient.

5.5 Conclusion

In conclusion, MVPA has emerged as a powerful tool in cognitive neuroscience for detecting representational-specific neural patterns using M/EEG. Its application to OPM-MEG data holds great promise, particularly with the improved spatial coverage provided by the new system and the sensors being close to the head. Here we investigated the design considerations when utilizing OPM-MEG data for MVPA. For the noise reduction algorithm, we do not recommend using SSS, but rather other approaches that do not reduce the rank of the data substantially such as SSP. Also, ICA or 3rd-order gradient noise reduction could be considered. We also recommend recording data from at least 25 equally distributed OPMs when working with image categorization tasks.

Chapter 6

Semantic representations for words and pictures studied with SQUID-MEG

The material in this chapter including text, images, and data has been published on bioRxiv [70] and submitted for publication in the Journal of Cognitive Neuroscience "Spatiotemporal properties of semantic categories common for words and pictures" by Yulia Bezsudnova, Andrew J. Quinn and Ole Jensen. The results were already presented at the Conference on Cognitive Computational Neuroscience 2023 and published in a short paper "Cross-modal semantic activation investigated using multivariate approaches applied to MEG data" by Yulia Bezsudnova, Andrew J. Quinn, Syanah Wynn, and Ole Jensen. My contribution to the study as a first author was developing the methodology, conducting experiments, analysing data, and drafting and editing the manuscript. The research was conducted under the supervision of Ole Jensen, with statistical analysis assistance provided by Andrew Quinn. Some of this material remains largely unchanged, while others have been made more appropriate for the thesis.

In this chapter, I present the findings of an experiment conducted using a conventional SQUID MEG system, aimed at investigating semantic representation from different modality stimuli (written words and pictures) using multivariate pattern analysis. Our results based on SQUID-MEG data provide evidence for a shared semantic representation between words and pictures. When the classifier is trained on words, pictures are classified between 150 - 430

ms from after stimulus onset, and when training on pictures, words are classified between 225 - 430 ms. The topographical map identified using a searchlight approach for cross-modal activation in both directions showed left lateralization confirming the involvement of linguistics representations. These results point to semantic activation of pictorial stimuli occurring at ≈150 ms whereas for words the semantic activation occurs at ≈230 ms.

6.1 Introduction

Humans are capable of recognizing and inferring the semantic category of a presented object regardless of the modality in which it is presented, whether through visual, auditory, or textual means.

A powerful way of studying how the human brain encodes the semantics of objects is to apply multivariate pattern analysis (MVPA) to human electrophysiological responses to stimuli of different conceptual categories [174, 204, 205]. The timing of the transition from visual representations of individual objects to more abstract semantic-type concepts is determined by identifying the time points at which the category of the object can be accurately predicted from the multivariate representation in the MEG and EEG data [175, 206]. However, drawing meaningful conclusions from the above-chance classification using stimuli from a single modality may be limited, as there are often multiple dimensions in which the two conditions differ [179, 207]. For example, one can argue that perceptual information beyond semantic content influences classification outcomes. Furthermore, the temporal dynamic of object recognition may also be influenced by the specific experimental task employed in the study, such as a one-back task, category judgment, or detection task. As such the precise timing of semantic category activation remains an open question [178, 208–213].

Studying brain responses to stimuli from different modalities (e.g. words vs. images) mitigates the criticism related to the influence of perceptual features on classification, as these stimuli do not share common low-level features [214]. Additionally, demonstrating the existence of cross-modal generalization (training a classifier on one modality, classifying another) at

specific time points will provide insights into the ongoing debate about how and when semantic information is encoded. This includes testing the hub-and-spoke theory of semantic representations where the representation first arises in a modality-specific way and later transfers to the amodal hub [215–217]. There is limited research done to investigate the time of cross-modal generalization using M/EEG and the reported time dynamic of cross-modal representation varies [178, 186, 213, 218].

In the MEG study [218] the categorization between famous places (”Big Ben”) and famous people (”Brad Pitt”) is studied for the picture and written word modalities. After each stimulus, participants were asked to perform either a shallow categorization task (Place or Person?) or a deeper semantic task (“Italian or foreign?”). Within the modality (modality-specific) category information robustly appears around 100 ms for pictures and 230 ms for words. The cross-modal (across modality) classification was studied only from words to pictures and revealed three significant clusters separated in time. Specifically, the authors suggest that cross-modal generalization unfolds through a three-stage process and the first shared representations are accessed at 200 ms using words and at 110 ms using pictures. However, brain activity from concepts such as famous places and people used in their paradigm might not generalize to more common objects. Furthermore, any findings of cross-modal representations across modalities could be driven by a shared category-judgment process due to a category-naming task rather than an automatic activation of semantic representations [219].

Another recent MEG study [178] examining generalization between written words and pictures using picture naming and word reading tasks showed different results. Significant decoding (animal vs. tool) activates surprisingly early around 75 ms for pictures, and 95 ms for words. Cross-generalization occurs simultaneously for both modalities around 150 ms. The different time courses of the shared semantic representation between [178] study and [218] study could be attributed to variations in participant tasks and experimental paradigms. Importantly, in [178] a block presentation of categories was utilized to demonstrate cross-modal categorization. This might result in anticipatory effects making the semantic categorization occur earlier. Based on these considerations, the precise timing of the activation of the shared representation should

be reevaluated in experiments where the category order is randomized while explicit category naming is not required.

In this work, we investigated the time course of semantic activation within and across pictural and textual stimulation presented in a randomized order. We analyzed MEG data using MVPA analysis. To further eliminate any anticipatory biases such as the possibility of stronger activation of general motor commands for the tools category we chose to include multiple categories. Finally, we applied a searchlight approach to identify the brain areas involved in the semantic representations.

6.2 Methods

In this chapter, I used the data from the experiment described in Chapter 5, therefore following description of the experimental paradigm is the same. However, here I used the whole dataset, whereas, in the previous chapter, only the data from the picture blocks were analysed. Note that the preprocessing pipeline is also different.

6.2.1 Participants

Thirty-eight healthy adult participants took part in the study. Five participants had to be excluded due to extensive noise (most of ICA components were contaminated with external artefacts) in the data and two participants were excluded due to low accuracy during the task (accuracy less than 85%). Therefore the final sample consisted of 31 participants (mean age ± SD = 21.77 ± 3.31; 21 females). The study was conducted at the Center of Human Brain Health in Birmingham, United Kingdom. All participants were native English speakers with normal or corrected-to-normal vision. The University of Birmingham Ethics Committee approved the study. The participants provided written informed consent and received £15 per hour or course credits as compensation for their participation.

6.2.2 Experimental paradigm

The experimental design (Fig. 6.1) was inspired by the study [186], however, some stimuli were replaced as well as the task for the participant was modified. The stimulus set was composed of 48 objects. Each stimulus was presented as a picture and a written word. The objects were organized according to three dimensions of categories, each separated into two categorical divisions: "size" (big or small), "movement" (moving or still), and "nature" (natural or man-made). Each object in the study belonged to each of the dimensions (e.g. a book is small, still, and man-made). The stimulus set was balanced such that each categorical division included one-half of the stimulus set (24 objects). Hence each set of categories (e.g. big, still, natural) included 6 objects. The selection of categorical divisions in this study was based on previous findings demonstrating reliable neural representations of semantic dimensions across categories [186, 188]. For other purposes not to be analyzed here, each object is presented in two modalities: written words and pictures. The size of the images is 400 x 400 pixels presented on a grey screen at a visual angle of 6°. In the stimuli set for textual modality (font: Arial, bold, 75), we did not control for the lexical properties of the words, which resulted in a mixture of high-frequency and low-frequency words. Additionally, the length of the words was not controlled.

Each object (word or picture) was presented for 0.6 s. Prior to the object presentation, the fixation cross was shown for 0.5-0.7 s. The experiment was divided in 9 blocks where either the succession of words (5 blocks) or images (4 blocks) was presented. The experimental design followed a consistent order, with word blocks always presented first, followed by image blocks, and so on (Fig 6.1B). After each block, a participant had a break. We included an extra word block based on previous reports that indicated a lower signal-to-noise ratio for classification in the textual modality [178, 213]. Each block consisted of 240 trials, with 48 of them being question trials, and lasted for around 6 minutes. Each stimulus was present 4 times in a block: when pictures were presented the probe question was presented as a word and vice versa. As such a participant had to identify the correct picture during the written words and vice versa. This design aimed to keep participants engaged and stimulate deep cross-modal perception without

explicitly addressing the category distinction between stimuli. Note that in each block the probe question was applied for every object once and alternative choices were unique as well.

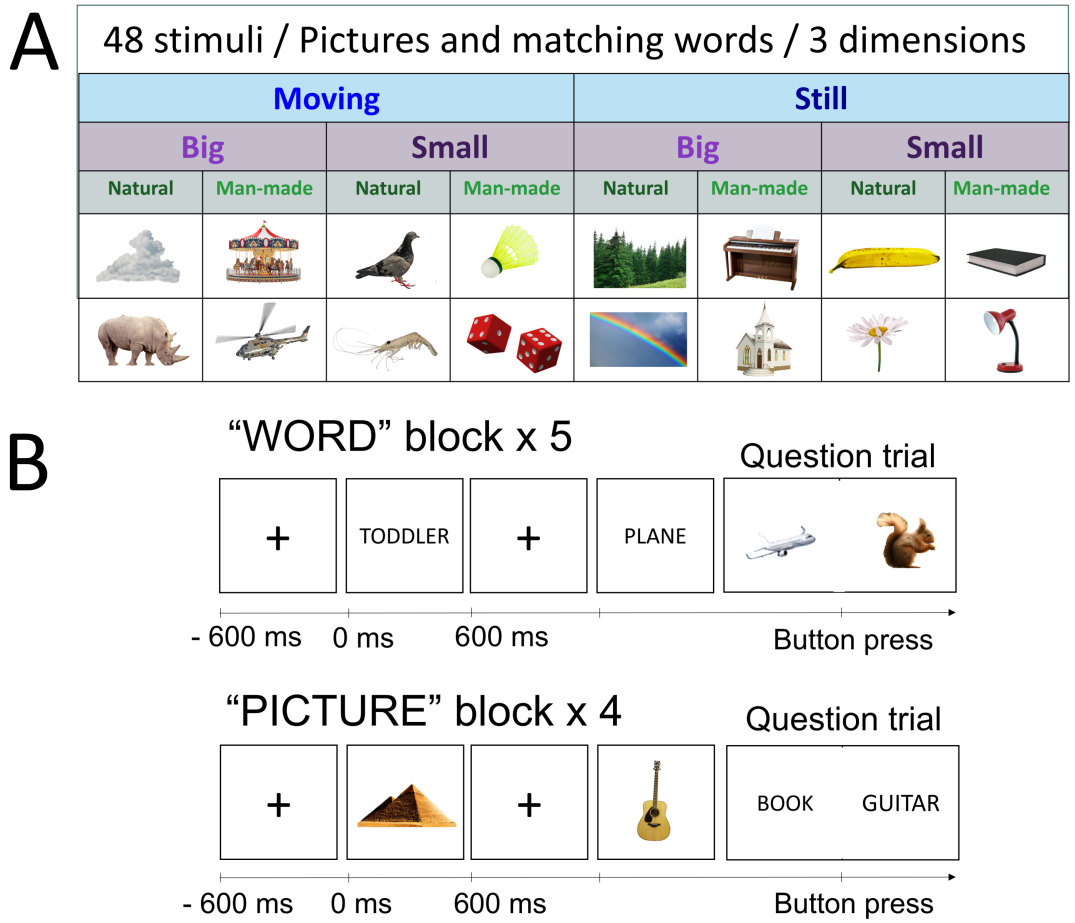

Figure 6.1: Experimental paradigm. A) The stimulus set is comprised of 48 objects which can be divided according to 3 dimensions (”size”: big/small; ”movement”: still/moving; ”nature”: natural/man-made). B) In both image and word blocks, participants were presented with stimuli in random order. In the picture block, participants viewed images of the objects, while in the word block, they read the corresponding words. The task (question trial) was presented randomly every fifth trial on average. Participants were required to identify whether the picture or word corresponded to a previously seen stimulus and press the appropriate button accordingly. When pictures were presented the probe question was presented as a word and vice versa.

The stimuli presentation is implemented in MATLAB using the Psychophysics Toolbox [189].

6.2.3 MEG acquisition

MEG data were recorded using a 306-sensor TRIUX MEGIN Elekta Neuromag system, consisting of 204 orthogonal planar gradiometers and 102 magnetometers, with online band-pass filtering from 0.1 to 330 Hz and a sampling rate of 1000 Hz. Before collecting data, the positions of three anatomical fiducial points (nasion, left preauricular, and right preauricular points) were recorded using a Polhemus Fastrack electromagnetic digitizer system. Furthermore, we recorded the positions of four head-position indicator coils (HPI coils): two placed on the left and right mastoid bone, and two on the forehead, with a minimum separation of 3 cm between each coil. After completing these initial steps, participants were seated in an upright position with a 60° angled backrest within the MEG gantry. Electrodes were fixed about 2.5 cm from the outer canthus of each eye to capture horizontal EOG signals. To record the vertical EOG, a pair of electrodes was placed above and below the right eye in line with the pupil. The ECG signals were captured using a set of electrodes positioned on both the left and right collarbones.

6.2.4 Data preprocessing

The data are analyzed using the open-source toolbox MNE Python v1.4.2 [190] following the standards defined in the FLUX Pipeline [191].

First, blinks and muscle artefacts are annotated using EOG channels and magnetometers recordings respectively. A semi-automatic detection algorithm was utilized to mark sensors with excessive artefacts (on average 4.5 channels per participant). Then, the data was low-pass filtered at 100 Hz to reduce HPI coils artefacts. We did not use signal-space separation (SSS) or Maxwell filtering because, as demonstrated in Chapter 5, they negatively impact classification results. We attribute this decline in performance to the significant rank reduction resulting from SSS filtering [192]. Independent Component Analysis (ICA) algorithm was applied [195] to remove components associated with cardiac artefacts and eyeblinks. The identification process involved analyzing the time courses and topographies of the ICA components. On average, 3 components corresponding to two cardiac-related and one blink-related artefact were identified

and removed for each subject. After ICA the data was segmented into trials. Trials corresponding to the same stimulus were averaged together to construct "supertrials". This step further enhances the SNR of the data [170, 196]. We applied a highpass filter of 0.1 Hz and downsampled the data to 500 Hz. The epochs were time-locked to the onset of the stimuli and were cropped to a time window of 100 ms before the stimuli and 700 ms after the stimuli onset. Each time point was represented as a 306-dimensional vector (channel data). We expanded this vector by including past 25 ms (12 time points) and future 25 ms (12 time points) of data, resulting in a 306x25 dimensional feature vector representing each time point. This procedure (termed "delayed embedding") resulted in a more information-rich representation of the neural activity associated with a given stimulus by incorporating more time points [197–199]. This feature vector was then used in the classifier.

6.2.5 Classification analysis

Multivariate pattern analysis was applied to the pre-processed MEG data to classify the categories of the presented objects [165, 174, 205]. Trials associated with different categories (e.g. moving vs still) and one modality (e.g. words) are labelled accordingly and used as input for the classifier. Prior to classification, the data was standardized by removing the mean and scaling to unit variance per sensor. Subsequently, we employed a support vector machine (SVM) [200] from the Python module Scikit-learn to classify the data over time. The classification procedure relied on a 5-fold cross-validation approach, and the performance was quantified using the area under the curve (AUC) metric, which measures the classifier discriminative ability. This procedure was done separately for each subject.

First, we investigated the classification accuracy with time for each category dimension ("movement", "size", and "nature") averaged across participants for each modality separately. The dimensions where both modalities showed classification accuracy significantly above the chance level were selected for cross-modal analysis. For cross-modal analysis, we also used time-generalized MVPA [184]. We used the classification approach mentioned above with the exception that the classifier was training in one modality at one time point and testing it on

another at a different time point. This procedure was done twice, once with the classifier trained on the words data and tested on the pictures data, and once where it was trained on the pictures data and tested on the words.

In order to explore the spatial distribution of representations across the MEG sensors over time, we employed the searchlight approach on sensor-level data [171, 218]. In this approach, classification was performed on ”patches” which are defined by one sensor (e.g. sensor MEG 1423) and all sensors within a 4 cm radius (e.g. 4 cm from MEG 1423). This typically resulted in 15 sensors (consisting of gradiometers and magnetometers). Therefore the feature vector had dimensions Nx25, where N is the number of sensors in the ”patch” and 25 time points from the delayed-embedding procedure. Patches were created for all possible sensor locations (rim sensors had fewer sensors in the patch). For each channel location the classification accuracy from the relevant ”patch” was averaged over a chosen time interval and this value was plotted on the topographical sensor map.

6.2.6 Statistical analysis

To find significant time points for the modality-specific classification curves and simultaneous cross-generalization, we used a non-parametric one-sampled permutation t-test (one-tailed) against 50% chance level, controlled for multiple comparisons [220, 221] implemented in GLMTools package Python (https://pypi.org/project/glmtools/). Clusters were formed based on direct adjacency in time (the minimum number of vertices in terms of time points in a cluster was set to 2). We set a cluster-forming threshold of 1.7, corresponding to an alpha threshold of 0.05. The mean t-value within each cluster was examined. A cluster was considered significant if its associated p-value was below the alpha threshold.

The same analysis was done for cross-modal time generalization results. Note that in this case the clusters are based on direct adjacency in both axes.

6.3 Results

6.3.1 Within-modality decoding

The category decoding shows significant results for pictures for every categorical dimension ("size", "movement", and "nature") separately. For words, we found the above channel level classification only for dimensions "size" (big/small) and "movement" (still/moving), but not "nature" (natural/man-made). In a previous study [174] this category also exhibited the lowest decoding accuracy when examining pictures, suggesting that it might also be difficult to decode across modalities [178, 186]. Therefore, all the results were derived by averaging the classification results obtained from just two categorical dimensions ("size" and "movement").

The classification accuracies for the picture modality and textual modality are shown in Fig. 6.2. As expected, a classifier that uses brain activity elicited by words showed lower performance compared to picture stimuli. For words, decoding is most pronounced around 240 - 350 ms after stimuli are presented. For pictures, decoding is most pronounced around 155 - 510 ms. These results indicate that semantic activation for words occurs approximately 100 ms later than for pictures. Note that the time estimation might be blurred due to the feature vector including ±25 ms of information, however, the relative relationships between modalities are preserved.

For the time points (300 ± 10 ms) when the decoding accuracy is strongest, we show topographical maps of the classification accuracy using a searchlight approach. The sensors that contributed strongest to the overall accuracy of the picture category are located over bilateral temporal and parietal areas (Fig. 6.3A). For the decoding word category, the informative sensors are located over the left temporal and left frontal parts of the brain (Fig. 6.3B). This localization is in line with prior results using MEG in object decoding [174] and word reading studies [206, 222].

6.3.2 Cross-modal decoding

The simultaneous (trained and tested on the same time points) cross-modal classification between textual and pictural modality is shown in Fig. 6.4. When training on words and testing on

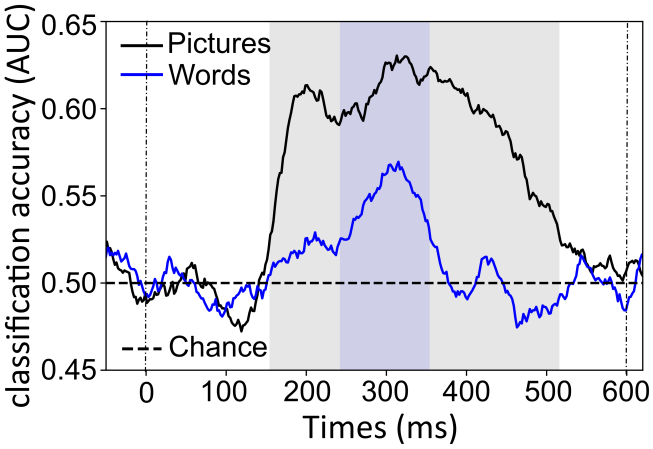

Figure 6.2: The time course of category decoding averaged over two categorical dimensions: "size" (big/small), and "movement" (still/moving). The blue line marks the classification curve for word modality, black line marks the classification curve for picture modality. Significant clusters ($p < 0.05$; controlled for multiple comparisons over time) are shown as highlighted areas accordingly.

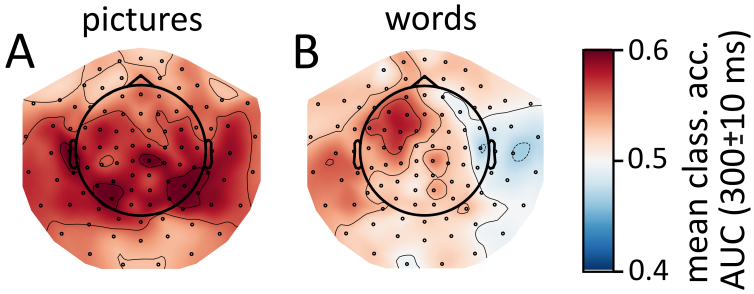

Figure 6.3: Topographical map of category decoding averaged over 300 ± 10 ms created using searchlight MVPA A) decoding categories of pictures, B) decoding categories of words. The colorcode indicates the classification accuracy (AUC) averaged over the time interval 300 ± 10 ms. The classification accuracy is averaged over two category dimensions: "size" (big/small), "movement" (still/moving)

pictures, the significant cluster emerged at 280 to 430 ms. When reversely training on pictures and testing on words, the cluster emerged at 330 to 430 ms.

We further examined time-generalized cross-decoding results (Fig. 6.5).

When training on pictures and testing on words the shared representation occurs between 225 - 430 ms (Fig. 6.5A); when training on words and testing on pictures the shared representation occurs between 150 and 430 ms (Fig. 6.5B). Interestingly, the most pronounced semantic

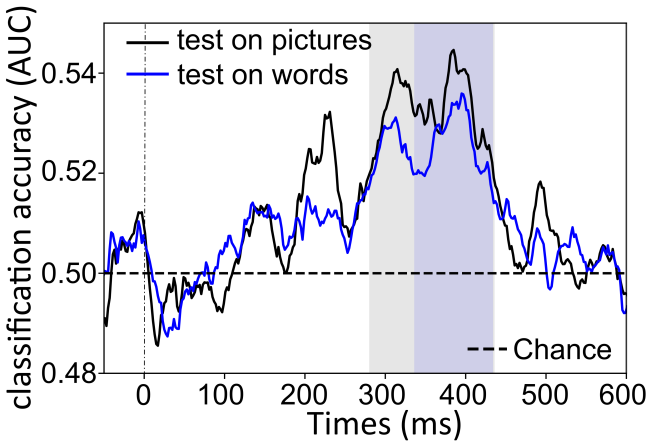

Figure 6.4: The time course of simultaneous (trained and tested on the same time points) cross-modal category decoding averaged over two categorical dimensions: "size" (big/small), and "movement" (still/moving). The blue line marks the classification curve when classifiers were trained on pictures and tested on words, black line marks the classification curve when trained on words and tested on pictures. Significant clusters ($p < 0.05$; controlled for multiple comparisons over time) are shown as highlighted areas accordingly.

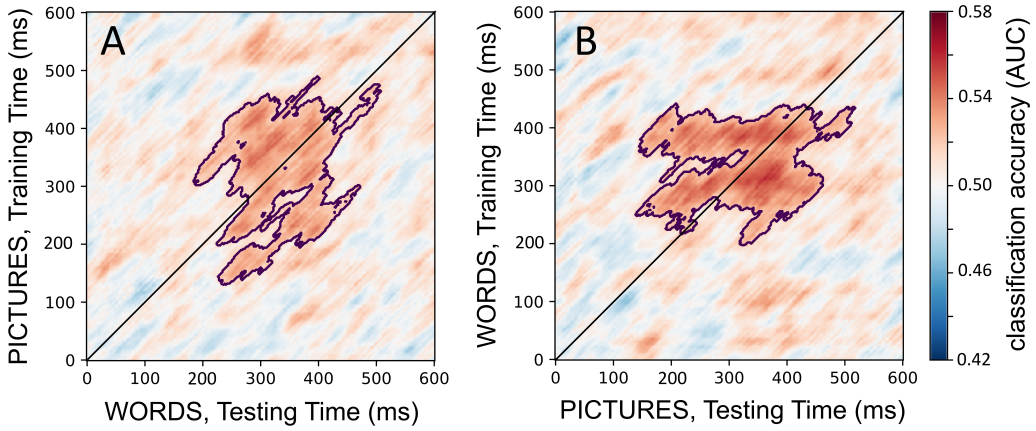

Figure 6.5: Time generalization results for category information, where classifier were A) trained on pictures and tested on words; B) trained on words and tested on pictures. The classification accuracy is averaged over two categorical dimensions: "size" (big/small), and "movement" (still/moving). Significant clusters are highlighted (one-sided permutation test, $p < 0.05$, corrected for multiple comparisons).

decoding across modalities for both words and pictures becomes significant around the same time as the categories are classified within each modality (Fig. 6.2). In sum, when considering the within- and cross-modal results, this point to semantic activation of respectively pictures and words occurs at 150 ms and 230 ms.

As noticed before for all the presented results the time estimation might be blurred (± 25 ms), however, the relative relationships between modalities are preserved.

Next, we show the topographical maps of the decoding accuracy at 400 ± 10 ms to check where the simultaneous cross-modal classification is the most pronounced (Fig. 6.6). We selected the time interval of 400 ± 10 ms because it corresponds to the peak decoding accuracy in Fig. 6.4.

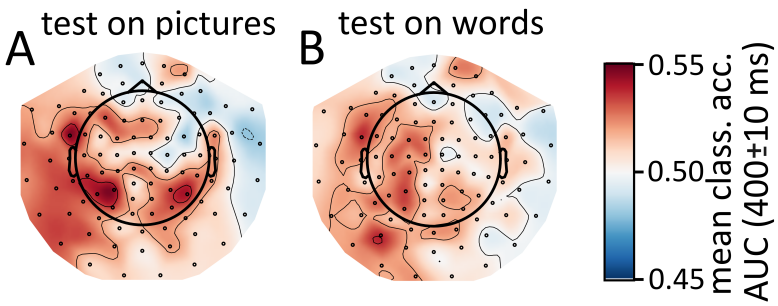

Figure 6.6: Topographical map of cross-modal categorical decoding averaged over 400 ± 10 ms created using searchlight MVPA A) when training on words, testing on pictures modality; B) when training on pictures, testing on words modality. The colorcode indicates the classification accuracy averaged over the time interval 400 ± 10 ms. The classification accuracy is averaged over two categorical dimensions: "size" (big/small), "movement" (still/moving)

These map for simultaneous cross-modal activation in both directions shows more pronounced left lateralization (Fig. 6.6) compared to topographies from within-modality decoding (Fig. 6.3).

6.4 Discussion

In this study, we investigated the temporal dynamics of semantic processing when objects were as pictures and text. We assessed the qualitative similarities between categories elicited for each modality using MVPA analysis on MEG data. The classification shows the most pronounced decoding activation for the pictures starting at 155 ms over the bilateral posterior part of the brain and for words after ≈240 ms over the left temporal and frontal parts of the brain (Fig. 6.3). We show successful cross-modal classification using MEG data (Fig. 6.5). If the classifier is trained

on words, pictures are classified between 150 - 430 ms, and when training on pictures, words are classified between 225 - 430 ms. The topographical map for simultaneous cross-modal activation in both directions (from words to pictures and from pictures to words) reveals strong left lateralization (Fig. 6.6).

Semantic activation for pictures starts around 150 ms, consistent with findings reported in a previous study [186] that employed a similar set of stimuli. The temporal dynamics of representations elicited by words demonstrate a later activation around 240 ms, which is in line with [218] and studies using the N400 paradigm where the N400 response starts to build up at 250 ms [223]. The different timing of picture and word categorization can be explained by the fact that low-level visual features in written words are less informative of semantic categories compared to pictures [214]. Note that decoding onsets of 75 ms for pictures and 95 ms for words acquired in the study [178] is almost 70 ms earlier than what we have demonstrated here. This disparity could likely be attributed to the categorical presentation in blocks as in the study by [178], which facilitates faster category extraction.

Time course of cross-modal decoding (Fig. 6.5) with off-diagonal time points structured as a rectangle suggests the shared semantic representation exhibits some sustained features common to both modalities. Semantic activation when classifying from pictures to words starts around 225 ms, while from words to pictures, it begins approximately at 150 ms. We attribute comparable timing of modality-specific and cross-modal semantic decoding to linguistic activation when viewing both pictures and words due to the task design. Participants had to identify the word that corresponds to the previously seen picture and vice versa, therefore the association between the two modalities was encouraged. This also explains why the topographical maps from cross-modal decoding for both directions (Fig. 6.6) show that the most informative sensors are located over the left regions of the brain, resembling the topographical map of word categorization. Words elicit abstract shared category representations due to their non-representative low-level feature, whereas categorization within pictorial modality is contaminated by perceptual features. Furthermore, the location of most informative sensors may include the left anterior temporal lobe (ATL) as shown with fMRI to be involved in semantic processing across various tasks

and, including cross-modal generalization between written words and corresponding images [216, 224]. These studies support the hub and spoke theory [215] in which the ATL supports shared representations. While our MEG study is inconsistent with the hub and spoke theory for semantic representations, our topographical plots do point to an extended network supporting the semantic encoding going beyond the ATL.

6.5 Conclusion

Our results demonstrate the time course of modality-independent semantic representations isolated from perceptual confounds. Specifically, we examined the time-course of activation of semantic representations common for words and pictures. We found that the semantic activation of words occurs at ≈230 ms. In the future, we will conduct the same experiment with OPM-MEG system to check our hypothesis that the new system can offer significant advantages in experiments designed for multivariate pattern analysis. In the future, we will conduct the same experiment with OPM-MEG system to check our hypothesis that the new system can offer significant advantages in experiments designed for multivariate pattern analysis.

Chapter 7

Conclusion and future research

The purpose of this thesis was to improve the performance of optically pumped magnetometers systems for magnetoencephalography applications. To surpass traditional SQUID systems, the OPM-MEG sensors must possess several key characteristics. It must be able to resist external interference, by having a dynamic range large enough to tolerate typical MSR background field fluctuations, as well as slight movements from the subject. They should also be able to operate at room temperature in order to be placed directly onto the scalp to detect the strongest brain signal and have a bandwidth from DC to 100 Hz. The sensors in the array should have a lower noise floor than spontaneous brain activity. Furthermore, for the best spatial resolution of the system, the sensors in the array must be sufficient in size and in number. Although this is a long list of challenging criteria, possible solutions to most of them have been explored throughout this thesis.

Chapter 1 of this thesis delved deeper into the challenges and existing solutions for OPM-MEG systems. The review highlighted the ongoing demand to improve the dynamic range of OPM sensors. This issue is discussed in Chapter 3 of this thesis where the results from our paper "Detection of human auditory evoked brain signals with a resilient nonlinear optically pumped magnetometer" published in Neuroimage (2020) are presented. We demonstrated that an OPM sensor utilizing nonlinear magneto-optical rotation can exhibit enhanced noise resilience compared to zero-field SERF OPM sensors, which are the majority of commercially available

sensors. The robust noise resilience of the NMOR sensor suggests potential compatibility with a TMS device. Preliminary findings indicate that the developed NMOR OPM sensors can recover from a TMS pulse in less than 25 ms, thereby enabling the measurement of magnetic brain signals immediately after the TMS pulse is delivered. Moreover, we speculate that the ideal OPM-MEG system for MEG applications should rely less on extra peripheral hardware like bi-planar active compensation coils and rather have a broader sensor dynamic range. There is now a trend towards replacing zero-field sensors with other techniques, such as free-induction decay OPMs, to improve system noise resilience, as shown in an increasing number of papers discussed throughout the thesis. However, to make NMOR-OPM sensor better suitable for MEG application the current noise floor needs to be reduced by at least a factor of two. A potential solution could be not to rely on fiber to transfer the light to the cell but rather put the semiconductor laser on the sensor head, which is done in most commercial sensors.

Furthermore, the literature review in Chapter 1, revealed a lack of efforts in sensor design optimization specifically for MEG applications. To enhance further the performance of an array of OPM sensors in MEG applications it is important to consider the specific noise sources present in the experiments, the arrangement of the sensors around the head, the purpose of the experiment, and whether the interest lies in source-level or sensor-level analysis.

In Chapter 4, we considered the optimization of the OPM-MEG system for the experiments relying on source reconstruction. It may seem like the more sensors in the helmet would achieve better localization accuracy, however, our simulation which took the brain noise into account revealed that the best overall sensitivity and reconstruction accuracy is achieved with just 70 sensors in an array. This number allows the use of a wide vapour cell inside each sensor while preserving the reconstruction accuracy of the system. The model used for this study is presented in "Optimising the sensing volume of OPM sensors for MEG source reconstruction." Neuroimage (2022). This work could be expanded to optimise other parameters, such as the intensity of the laser beam, the atomic density, or the gap between the sensor and the head. One interesting implication of the study is the possibility of optimizing the OPM system for localizing deep brain sources — an application that is not readily achievable with conventional

SQUIDs. The single sensor simulation results suggest that larger cells would be more sensitive to deep sources. However, more calculation is needed to understand the optimal size of the cell with respect to the depth of the source for the whole-head system and compute the optimised system resolution.

In Chapter 5, we considered the optimal parameters for the OPM-MEG system for experiments that focus on sensor-level data. For these purposes, we conducted a preliminary study based on the SQUID magnetometer array. We found that no more than 25 sensors are needed to achieve accurate picture categorization. Moreover, we optimized the pre-processing pipeline to fit the magnetometer data showing the traditionally used single-space separation filter has a negative effect on the results. This study also suggests that even with the conventional system pre-processing pipeline can benefit from more fine-tuning of the standard methods that have been developed for the source localisation rather than MVPA analysis.

Additionally, according to the literature review, an OPM array so far has been found to have comparable performance to a SQUID system but does not exceed it. We speculate that in experiments focused on spatial signal distribution at the sensor level, the OPM-MEG may outperform SQUIDs-based MEG. Chapter 6 presented the groundwork for future experiment OPM-MEG experiments that can benefit from the enhanced signal-to-noise of the OPM-MEG system compared to the SQUID MEG system. The study investigated the timing of semantic processing during object recognition. The timing of semantic representations is still a topic of ongoing discussion. Our current results based on SQUID-MEG data already provided the evidence for a shared semantic representation. However, we hypothesize that OPM-on-scalp placement will provide a more accurate and detailed time course of brain activity. This experiment will offer an empirical comparison of the spatial resolution between the OPM-MEG system and the conventional SQUID system.

In summary, the work presented in this thesis lays the foundation for optimising OPM-MEG systems in neuroscience research. Earlier, I provided a brief overview of potential subsequent research for each chapter, highlighting novel applications of the OPM-MEG system compared to conventional approaches. Now, I will describe a few future directions in more detail.

No type of OPM sensor developed for MEG applications has yet reached the noise floor of the SQUIDS. However, theoretically, OPM has the potential to surpass this limit, making it a clear and promising avenue for further exploration. The present sensitivity of the sensors is constrained by technical noise such as polarization drifts, laser power noise, power-supply noise, shield noise, photodiode noise, Johnson noise from bias coils, etc. The majority of commercially available sensors employ a synchronous pumping technique, introducing a trade-off between sensitivity and bandwidth (refer to Chapter 2 and [81] for detailed information). The utilization of phase-sensitive detection to overcome bandwidth limitations not only introduces additional electronic noise and modulation-frequency instability to the system but also results in a linear decrease in the SNR with increasing frequency. A potential and promising solution to address the fluctuating SNR is the utilization of the self-oscillating mode, where the output signal frequency is directly fed back to the input pump-modulation frequency, or through instantaneous phase retrieval. Implementing the latter method in [130] resulted in more than two orders of magnitude higher measurement capability for alternating current magnetic fields in terms of both amplitudes and frequencies.

Optimisation of electronics would leave the environmental noise as a limiting factor for OPM sensitivity. Biomagnetism application implies operating within a large room as opposed to confined μ-metal shields which makes low-frequency environmental noise inevitable. An array of magnetometers can eliminate noise common to all sensors post data collection. However, the incorporation of intrinsic gradiometers not only provides cleaner raw data by attenuating ambient magnetic-field noise making it suitable for applications like brain-computer interfaces. NMOR OPM gradiometer can also facilitate more rapid recovery after a TMS pulse. This advancement could result in an OPM-MEG-TMS system well-suited for precisely investigating brain connectivity. Furthermore, an intrinsic gradiometer would make it possible to work with a smaller number (<100) of sensors in an array, when the denoising algorithm like SSS is not very efficient. A gradiometer is also advantageous for experiments involving participant movement, as it can promptly filter out noise on a walking subject. This could potentially offer a more cost-effective solution compared to an active shield while also expanding the allowable movement

area.

In MEG applications, there is the additional challenge of brain noise contaminating the data, as demonstrated by simulations in Chapter 4. These simulations suggest that the specific shape of the cell can help mitigate this issue. This solution might be particularly advantageous for studying deep sources in the brain, which is one of the most intriguing applications of the OPM-MEG system to explore. Therefore, it would be worthwhile to further explore this direction and experimentally investigate whether, for the localization of deep sources, there is more advantage in averaging out brain noise or more disadvantage in reducing spatial resolution.

Another interesting direction that has remained mostly untouched would be to exploit the flexibility of the placement of OPM sensors to measure signals that are not visible with a rigid SQUID system. For example 1 out of 10 healthy subjects does not have a detectable alpha peak activity. Determining whether this absence is anatomical (resulting from dipoles oriented in a way that SQUID sensors cannot detect) or has a neuronal basis can be addressed by strategically arranging OPM sensors to capture individual lead-fields and utilizing all three axes available in the state-of-the-art OPM system.

References

1. Barratt, E. L., Francis, S. T., Morris, P. G. & Brookes, M. J. Mapping the topological organisation of beta oscillations in motor cortex using MEG. *NeuroImage* **181,** 831–844 (2018).

2. Hedrich, T., Pellegrino, G., Kobayashi, E., Lina, J.-M. & Grova, C. Comparison of the spatial resolution of source imaging techniques in high-density EEG and MEG. *Neuroimage* **157,** 531–544 (2017).

3. Hari, R. *et al.* IFCN-endorsed practical guidelines for clinical magnetoencephalography (MEG). *Clinical Neurophysiology* **129,** 1720–1747 (2018).

4. Brookes, M. J. *et al.* Magnetoencephalography with optically pumped magnetometers (OPM-MEG): the next generation of functional neuroimaging. *Trends in Neurosciences* (2022).

5. Proudfoot, M., Woolrich, M. W., Nobre, A. C. & Turner, M. R. Magnetoencephalography. *Practical neurology* **14,** 336–343 (2014).

6. Boto, E. *et al.* On the potential of a new generation of magnetometers for MEG: a beamformer simulation study. *PloS one* **11,** e0157655 (2016).

7. Iivanainen, J., Stenroos, M. & Parkkonen, L. Measuring MEG closer to the brain: Performance of on-scalp sensor arrays. *NeuroImage* **147,** 542–553 (2017).

8. Bezsudnova, Y., Koponen, L. M., Barontini, G., Jensen, O. & Kowalczyk, A. U. Optimising the sensing volume of OPM sensors for MEG source reconstruction. *NeuroImage* **264,** 119747 (2022).

9. Xia, H., Ben-Amar Baranga, A., Hoffman, D. & Romalis, M. Magnetoencephalography with an atomic magnetometer. *Applied Physics Letters* **89,** 211104 (2006).

10. Nugent, A. C., Andonegui, A. B., Holroyd, T. & Robinson, S. E. On-scalp magnetocorticography with optically pumped magnetometers: Simulated performance in resolving simultaneous sources. *Neuroimage: Reports* **2,** 100093 (2022).

11. Budker, D. & Romalis, M. *Optical magnetometry* **4,** 227–234 (Nature Publishing Group UK London, 2007).

12. Sander, T. *et al.* Magnetoencephalography with a chip-scale atomic magnetometer. *Biomedical optics express* **3,** 981–990 (2012).

13. Wens, V. Exploring the limits of MEG spatial resolution with multipolar expansions. *NeuroImage* **270,** 119953 (2023).

14. Iivanainen, J. *et al.* Spatial sampling of MEG and EEG revisited: From spatial-frequency spectra to model-informed sampling. *arXiv preprint arXiv:2006.02919* (2020).

15. Tierney, T. M. *et al.* Pragmatic spatial sampling for wearable MEG arrays. *Scientific reports* **10,** 21609 (2020).

16. Palacios-Laloy, A., Le Prado, M. & Labyt, E. in *Flexible High Performance Magnetic Field Sensors: On-Scalp Magnetoencephalography and Other Applications* 79–110 (Springer, 2022).

17. Boto, E. *et al.* Triaxial detection of the neuromagnetic field using optically-pumped magnetometry: feasibility and application in children. *NeuroImage* **252,** 119027 (2022).

18. Brookes, M. J. *et al.* Theoretical advantages of a triaxial optically pumped magnetometer magnetoencephalography system. *NeuroImage* **236,** 118025 (2021).

19. Widjaja, E. Wearable Magnetoencephalography: Reality or Science Fiction? *Radiology* **304,** 435–436 (2022).

20. Boto, E. *et al.* A new generation of magnetoencephalography: Room temperature measurements using optically-pumped magnetometers. *NeuroImage* **149,** 404–414 (2017).

21. Seymour, R. A. *et al.* Using OPMs to measure neural activity in standing, mobile participants. *NeuroImage* **244,** 118604 (2021).

22. Roberts, G. *et al.* Towards OPM-MEG in a virtual reality environment. *NeuroImage* **199,** 408–417 (2019).

23. Westner, B. U., Lubell, J. I., Jensen, M., Hokland, S. & Dalal, S. S. Contactless measurements of retinal activity using optically pumped magnetometers. *Neuroimage* **243,** 118528 (2021).

24. Broser, P. J., Middelmann, T., Sometti, D. & Braun, C. Optically pumped magnetometers disclose magnetic field components of the muscular action potential. *Journal of Electromyography and Kinesiology* **56,** 102490 (2021).

25. Mardell, L. C. *et al.* Concurrent spinal and brain imaging with optically pumped magnetometers. *bioRxiv,* 2022–05 (2022).

26. Broser, P. J. *et al.* Optically pumped magnetometers for magneto-myography to study the innervation of the hand. *IEEE Transactions on Neural Systems and Rehabilitation Engineering* **26,** 2226–2230 (2018).

27. Tierney, T. M. *et al.* Mouth magnetoencephalography: A unique perspective on the human hippocampus. *NeuroImage* **225,** 117443 (2021).

28. Zahran, S. *et al.* Performance Analysis of Optically Pumped 4He Magnetometers vs. Conventional SQUIDs: From Adult to Infant Head Models. *Sensors* **22,** 3093 (2022).

29. Gutteling, T. P. *et al.* A new generation of OPM for high dynamic and large bandwidth MEG: the 4He OPMs—first applications in healthy volunteers. *Sensors* **23,** 2801 (2023).

30. Supek, S. & Aine, C. J. *Magnetoencephalography* (Springer, 2016).

31. Marhl, U., Jodko-Władzińska, A., Brühl, R., Sander, T. & Jazbinšek, V. Transforming and comparing data between standard SQUID and OPM-MEG systems. *Plos one* **17,** e0262669 (2022).

32. Hill, R. M. *et al.* Multi-channel whole-head OPM-MEG: Helmet design and a comparison with a conventional system. *NeuroImage* **219,** 116995 (2020).

33. Labyt, E., Sander, T. & Wakai, R. *Flexible High Performance Magnetic Field Sensors: On-Scalp Magnetoencephalography and Other Applications* (Springer Nature, 2022).

34. Li, R., Perrella, C. & Luiten, A. Enhancing the sensitivity of atomic magnetometer with a multi-passed probe light. *Applied Physics Letters* **121** (2022).

35. Seymour, R. A. *et al.* Interference suppression techniques for OPM-based MEG: Opportunities and challenges. *NeuroImage* **247,** 118834 (2022).

36. Krzyzewski, S., Perry, A., Gerginov, V. & Knappe, S. Characterization of noise sources in a microfabricated single-beam zero-field optically-pumped magnetometer. *Journal of Applied Physics* **126** (2019).

37. Nardelli, N., Krzyzewski, S. & Knappe, S. Reducing crosstalk in optically-pumped magnetometer arrays. *Physics in Medicine & Biology* **64,** 21NT03 (2019).

38. Rea, M. *et al.* Precision magnetic field modelling and control for wearable magnetoencephalography. *NeuroImage* **241,** 118401 (2021).

39. Hunter, D. *et al.* Free-induction-decay magnetometer based on a microfabricated Cs vapor cell. *Physical Review Applied* **10,** 014002 (2018).

40. Sheng, D. *et al.* A microfabricated optically-pumped magnetic gradiometer. *Applied physics letters* **110** (2017).

41. Kamada, K., Ito, Y., Ichihara, S., Mizutani, N. & Kobayashi, T. Noise reduction and signal-to-noise ratio improvement of atomic magnetometers with optical gradiometer configurations. *Optics Express* **23,** 6976–6987 (2015).

42. Zhang, R., Mhaskar, R., Smith, K. & Prouty, M. Portable intrinsic gradiometer for ultrasensitive detection of magnetic gradient in unshielded environment. *Applied Physics Letters* **116** (2020).

43. Lucivero, V. *et al.* Femtotesla nearly-quantum-noise-limited pulsed gradiometer at earth-scale fields. *Physical Review Applied* **18,** L021001 (2022).

44. Kowalczyk, A. U., Bezsudnova, Y., Jensen, O. & Barontini, G. Detection of human auditory evoked brain signals with a resilient nonlinear optically pumped magnetometer. *NeuroImage* **226,** 117497 (2021).

45. Guo, Q. *et al.* A high sensitivity closed-loop spin-exchange relaxation-free atomic magnetometer with broad bandwidth. *IEEE Sensors Journal* **21,** 21425–21431 (2021).

46. Wang, K. *et al.* Triaxial closed-loop measurement based on a single-beam zero-field optically pumped magnetometer. *Frontiers in Physics* **10,** 1059487 (2022).

47. Tierney, T. M. *et al.* Optically pumped magnetometers: From quantum origins to multi-channel magnetoencephalography. *NeuroImage* **199,** 598–608 (2019).

48. Robinson, S. E. *et al.* Cross-axis dynamic field compensation of optically pumped magnetometer arrays for MEG. *NeuroImage* **262,** 119559 (2022).

49. Holmes, N. *et al.* A lightweight magnetically shielded room with active shielding. *Scientific Reports* **12,** 13561 (2022).

50. Holmes, N. *et al.* A bi-planar coil system for nulling background magnetic fields in scalp mounted magnetoencephalography. *Neuroimage* **181,** 760–774 (2018).

51. Ding, Z., Huang, Z., Pang, M. & Han, B. Design of bi-planar coil for acquiring near-zero magnetic environment. *IEEE Transactions on Instrumentation and Measurement* **71,** 1–10 (2022).

52. Holmes, N., Bowtell, R., Brookes, M. J. & Taulu, S. An Iterative Implementation of the Signal Space Separation Method for Magnetoencephalography Systems with Low Channel Counts. *Sensors* **23,** 6537 (2023).

53. Tierney, T. M., Mellor, S., O'Neill, G. C., Timms, R. C. & Barnes, G. R. Spherical harmonic based noise rejection and neuronal sampling with multi-axis OPMs. *Neuroimage* **258,** 119338 (2022).

54. Pang, M., Huang, Z., Ding, Z. & Han, B. Co-registration error analysis and array calibration for OPM-MEG system. *IEEE Transactions on Instrumentation and Measurement* **71,** 1–12 (2022).

55. Mellor, S. *et al.* Magnetic field mapping and correction for moving OP-MEG. *IEEE Transactions on Biomedical Engineering* **69,** 528–536 (2021).

56. Pang, M., Huang, Z., Ding, Z. & Han, B. Automatic Sensor Array Calibration and Co-registration for On-Scalp MEG. *IEEE Transactions on Instrumentation and Measurement* (2023).

57. Zetter, R., Iivanainen, J., Stenroos, M. & Parkkonen, L. Requirements for coregistration accuracy in on-scalp MEG. *Brain topography* **31,** 931–948 (2018).

58. An, N. *et al.* Imaging somatosensory cortex responses measured by OPM-MEG: Variational free energy-based spatial smoothing estimation approach. *Iscience* **25** (2022).

59. Borna, A. *et al.* Cross-Axis projection error in optically pumped magnetometers and its implication for magnetoencephalography systems. *Neuroimage* **247,** 118818 (2022).

60. Holmes, N. *et al.* Naturalistic hyperscanning with wearable magnetoencephalography. *Sensors* **23,** 5454 (2023).

61. Rea, M. *et al.* A 90-channel triaxial magnetoencephalography system using optically pumped magnetometers. *Annals of the New York Academy of Sciences* **1517,** 107–124 (2022).

62. Tierney, T. M. *et al.* Modelling optically pumped magnetometer interference in MEG as a spatially homogeneous magnetic field. *NeuroImage* **244,** 118484 (2021).

63. O'Neill, G. C. *et al.* Combining video telemetry and wearable MEG for naturalistic imaging. *bioRxiv,* 2023–08 (2023).

64. Vrba, J. & Robinson, S. E. Signal processing in magnetoencephalography. *Methods* **25,** 249–271 (2001).

65. Vrba, J. Toward Noise-Immune. *Magnetic Source Imaging of the Human Brain,* 203 (2003).

66. Duque-Muñoz, L. *et al.* Data-driven model optimization for optically pumped magnetometer sensor arrays. *Human Brain Mapping* **40,** 4357–4369 (2019).

67. An, N. *et al.* Spatial accuracy evaluation of magnetic source imaging methods on OPM-based MEG. *Iscience* **25,** 105177 (2022).

68. Bezsudnova, Y., Kowalczyk, A., Barontini, G. & Jensen, O. Optimization of the MEG-OPM sensor for environmental conditions.

69. Bezsudnova, Y. & Jensen, O. Optimizing magnetometers arrays and pre-processing pipelines for multivariate pattern analysis. *bioRxiv* (2023).

70. Bezsudnova, Y., Quinn, A. J. & Jensen, O. Spatiotemporal properties of common semantic categories for words and pictures. *bioRxiv* (2023).

71. Kitching, J., Knappe, S. & Donley, E. A. Atomic sensors–a review. *IEEE Sensors Journal* **11,** 1749–1758 (2011).

72. *Optical Magnetometry* (Cambridge University Press, 2013).

73. Pustelny, S. Nonlinear magneto-optical effects. *Jagiellonian University* (2007).

74. Loudon, R. *The quantum theory of light* (OUP Oxford, 2000).

75. Cohen-Tannoudji, C. *Atoms in electromagnetic fields* (World scientific, 1994).

76. Happer, W. Optical pumping. *Reviews of Modern Physics* **44,** 169 (1972).

77. Auzinsh, M., Budker, D. & Rochester, S. Light-induced polarization effects in atoms with partially resolved hyperfine structure and applications to absorption, fluorescence, and nonlinear magneto-optical rotation. *Physical Review A* **80,** 053406 (2009).

78. Rochester, S. & Budker, D. Atomic polarization visualized. *American Journal of Physics* **69,** 450–454 (2001).

79. Milner, V. & Prior, Y. Biaxial spatial orientation of atomic angular momentum. *Physical Review A* **59,** R1738 (1999).

80. Rochester, S. M. *Modeling nonlinear magneto-optical effects in atomic vapors* (University of California, Berkeley, 2010).

81. Wilson, N. M. *Nonlinear Magneto-Optical Rotation in Rubidium Vapour* PhD thesis (2020).

82. Alexandrov, E. B. *et al.* Dynamic effects in nonlinear magneto-optics of atoms and molecules. *JOSA B* **22,** 7–20 (2005).

83. Allen, L. & Eberly, J. H. *Optical resonance and two-level atoms* (Courier Corporation, 1987).

84. Steck, D. A. Quantum and atom optics (2007).

85. Richard, L. Introductory quantum mechanics. *Reading: Addison-Wesley* (2002).

86. Bloom, A. L. Optical pumping. *Scientific American* **203,** 72–81 (1960).

87. Happer, W., Jau, Y.-Y. & Walker, T. *Optically pumped atoms* (John Wiley & Sons, 2010).

88. Pustelny, S. *et al.* Nonlinear magneto-optical rotation with modulated light in tilted magnetic fields. *Physical Review A* **74,** 063420 (2006).

89. Acosta, V. *et al.* Nonlinear magneto-optical rotation with frequency-modulated light in the geophysical field range. *Physical Review A* **73,** 053404 (2006).

90. Budker, D. *et al.* Resonant nonlinear magneto-optical effects in atoms. *Reviews of modern physics* **74,** 1153 (2002).

91. Chen, X., Telegdi, V. & Weis, A. Quantitative study of the nonlinear Macaluso-Corbino (resonant Faraday) effect in Cs. *Optics communications* **74,** 301–305 (1990).

92. Budker, D., Kimball, D., Yashchuk, V. & Zolotorev, M. Nonlinear magneto-optical rotation with frequency-modulated light. *Physical Review A* **65,** 055403 (2002).

93. Schwindt, P., Hollberg, L. & Kitching, J. Self-oscillating rubidium magnetometer using nonlinear magneto-optical rotation. *Review of Scientific Instruments* **76** (2005).

94. Gawlik, W. & Pustelny, S. Nonlinear magneto-optical rotation magnetometers. *High sensitivity magnetometers,* 425–450 (2017).

95. Pustelny, S. *et al.* Magnetometry based on nonlinear magneto-optical rotation with amplitude-modulated light. *Journal of Applied Physics* **103,** 063108 (2008).

96. Bell, W. E. & Bloom, A. L. Optically Driven Spin Precession. *Phys. Rev. Lett.* **6,** 280–281 (1961).

97. Bell, W. E. & Bloom, A. L. Optical detection of magnetic resonance in alkali metal vapor. *Physical Review* **107,** 1559 (1957).

98. Seltzer, S. J. *Developments in alkali-metal atomic magnetometry* PhD thesis (2008).

99. Castagna, N. *et al.* A large sample study of spin relaxation and magnetometric sensitivity of paraffin-coated Cs vapor cells. *Applied Physics B* **96,** 763–772 (2009).

100. Smullin, S., Savukov, I., Vasilakis, G., Ghosh, R. & Romalis, M. Low-noise high-density alkali-metal scalar magnetometer. *Physical Review A* **80,** 033420 (2009).

101. Shah, V., Knappe, S., Schwindt, P. D. & Kitching, J. Subpicotesla atomic magnetometry with a microfabricated vapour cell. *Nature Photonics* **1,** 649–652 (2007).

102. Budker, D., Kimball, D., Rochester, S., Yashchuk, V. & Zolotorev, M. Sensitive magnetometry based on nonlinear magneto-optical rotation. *Physical Review A* **62,** 043403 (2000).

103. Sheng, D., Li, S., Dural, N. & Romalis, M. V. Subfemtotesla scalar atomic magnetometry using multipass cells. *Physical review letters* **110,** 160802 (2013).

104. Limes, M. *et al.* Portable magnetometry for detection of biomagnetism in ambient environments. *Physical Review Applied* **14,** 011002 (2020).

105. Arnold, D., Siegel, S., Grisanti, E., Wrachtrup, J. & Gerhardt, I. A rubidium Mx-magnetometer for measurements on solid state spins. *Review of Scientific Instruments* **88** (2017).

106. Dehmelt, H. Modulation of a light beam by precessing absorbing atoms. *Physical Review* **105,** 1924 (1957).

107. Schultze, V. *et al.* An optically pumped magnetometer working in the light-shift dispersed Mz mode. *Sensors* **17,** 561 (2017).

108. Alexandrov, E. & Vershovskiy, A. Mx and Mz magnetometers. *Optical Magnetometry,* 60–84 (2013).

109. Marmugi, L., Deans, C. & Renzoni, F. Electromagnetic induction imaging with atomic magnetometers: Unlocking the low-conductivity regime. *Applied Physics Letters* **115** (2019).

110. Bevington, P., Gartman, R. & Chalupczak, W. Imaging of material defects with a radio-frequency atomic magnetometer. *Review of Scientific Instruments* **90** (2019).

111. Chalupczak, W., Godun, R., Pustelny, S. & Gawlik, W. Room temperature femtotesla radio-frequency atomic magnetometer. *Applied Physics Letters* **100** (2012).

112. Ingleby, S. J., O'Dwyer, C., Griffin, P. F., Arnold, A. S. & Riis, E. Orientational effects on the amplitude and phase of polarimeter signals in double-resonance atomic magnetometry. *Physical Review A* **96,** 013429 (2017).

113. O'Dwyer, C. *Development of atomic magnetometry towards unshielded sensors* PhD thesis (2020).

114. Kornack, T., Ghosh, R. & Romalis, M. V. Nuclear spin gyroscope based on an atomic comagnetometer. *Physical review letters* **95,** 230801 (2005).

115. Padniuk, M. *et al.* Response of atomic spin-based sensors to magnetic and nonmagnetic perturbations. *Scientific reports* **12,** 324 (2022).

116. Koshev, N. *et al.* Evolution of MEG: A first MEG-feasible fluxgate magnetometer. *Human Brain Mapping* **42,** 4844–4856 (2021).

117. Jensen, K., Kehayias, P. & Budker, D. Magnetometry with nitrogen-vacancy centers in diamond. *High sensitivity magnetometers,* 553–576 (2017).

118. Wickenbrock, A. *et al.* Microwave-free magnetometry with nitrogen-vacancy centers in diamond. *Applied Physics Letters* **109** (2016).

119. Seltzer, S. *et al.* Investigation of antirelaxation coatings for alkali-metal vapor cells using surface science techniques. *The Journal of chemical physics* **133** (2010).

120. Budker, D., Kimball, D. F., Yashchuk, V. V. & Zolotorev, M. Nonlinear magneto-optical rotation with frequency-modulated light. *Phys. Rev. A* **65,** 055403 (5 2002).

121. Ding, Y. *et al. Scalar Potassium Magnetometer Based On Amplitude Modulated Nonlinear Magneto-Optical Rotation* in *2021 Joint Conference of the European Frequency and Time Forum and IEEE International Frequency Control Symposium (EFTF/IFCS)* (2021), 1–2.

122. Savukov, I., Kim, Y., Shah, V. & Boshier, M. High-sensitivity operation of single-beam optically pumped magnetometer in a kHz frequency range. *Measurement Science and Technology* **28,** 035104 (2017).

123. Alem, O. *et al.* An integrated full-head OPM-MEG system based on 128 zero-field sensors. *Frontiers in Neuroscience* **17,** 1190310 (2023).

124. Dang, H. B., Maloof, A. C. & Romalis, M. V. Ultrahigh sensitivity magnetic field and magnetization measurements with an atomic magnetometer. *Applied Physics Letters* **97,** 151110 (2010).

125. Lee, H. J., Shim, J. H., Moon, H. S. & Kim, K. Flat-response spin-exchange relaxation free atomic magnetometer under negative feedback. *Optics express* **22,** 19887–19894 (2014).

126. Yan, Y. *et al.* Three-axis closed-loop optically pumped magnetometer operated in the SERF regime. *Optics Express* **30,** 18300–18309 (2022).

127. *QuSpin Gen3* https://quspin.com/products-qzfm/. Accessed:2023-09-18.

128. Nardelli, N., Perry, A., Krzyzewski, S. & Knappe, S. A conformal array of microfabricated optically-pumped first-order gradiometers for magnetoencephalography. *EPJ Quantum Technology* **7,** 11 (2020).

129. Hunter, D. *Chip-scale atomic magnetometer based on free-induction-decay* PhD thesis (2019).

130. Wilson, N., Perrella, C., Anderson, R., Luiten, A. & Light, P. Wide-bandwidth atomic magnetometry via instantaneous-phase retrieval. *Physical Review Research* **2,** 013213 (2020).

131. Zhang, L., Yang, Y., Zhao, N., He, J. & Wang, J. A Multi-Pass Optically Pumped Rubidium Atomic Magnetometer with Free Induction Decay. *Sensors* **22,** 7598 (2022).

132. Hunter, D. *et al.* Free-induction-decay magnetometer with enhanced optical pumping. *arXiv preprint arXiv:2307.11600* (2023).

133. Bertrand, F. *et al.* A 4He vector zero-field optically pumped magnetometer operated in the Earth-field. *Review of Scientific Instruments* **92** (2021).

134. Labyt, E. *et al.* Magnetoencephalography with optically pumped 4 He magnetometers at ambient temperature. *IEEE transactions on medical imaging* **38,** 90–98 (2018).

135. Fourcault, W. *et al.* Helium-4 magnetometers for room-temperature biomedical imaging: Toward collective operation and photon-noise limited sensitivity. *Optics Express* **29,** 14467–14475 (2021).

136. *Mag4Health sensors* https://brainbox-neuro.com/products/mag4health-he-opm-meg-system. Accessed:2023-09-18.

137. Boto, E. *et al.* Moving magnetoencephalography towards real-world applications with a wearable system. *Nature* **555** (2018).

138. Holmes, N. *et al.* Balanced, bi-planar magnetic field and field gradient coils for field compensation in wearable magnetoencephalography. *Scientific Reports* **9,** 14196 (2019).

139. Iivanainen, J., Zetter, R., Grön, M., Hakkarainen, K. & Parkkonen, L. On-scalp MEG system utilizing an actively shielded array of optically-pumped magnetometers. *NeuroImage* **194,** 244–258. ISSN: 1053-8119 (2019).

140. Kimball, D. F. J., Pustelny, S., Yashchuk, V. V. & Budker, D. in *Optical Magnetometry* (eds Budker, D. & Jackson Kimball, D. F.) 104–124 (Cambridge University Press, 2013).

141. Iivanainen, J., Zetter, R. & Parkkonen, L. Potential of on-scalp MEG: Robust detection of human visual gamma-band responses. *Human Brain Mapping* **41,** 150–161 (2019).

142. Pustelny, S., Kimball, D. J., Rochester, S., Yashchuk, V. & Budker, D. Influence of magnetic-field inhomogeneity on nonlinear magneto-optical resonances. *Physical Review A* **74,** 063406 (2006).

143. Balabas, M., Karaulanov, T., Ledbetter, M. & Budker, D. Polarized alkali-metal vapor with minute-long transverse spin-relaxation time. *Physical review letters* **105,** 070801 (2010).

144. Bloom, A. L. Principles of operation of the rubidium vapor magnetometer. *Applied Optics* **1,** 61–68 (1962).

145. Hämäläinen, M., Hari, R., Ilmoniemi, R., Knuutila, J. & Lounasmaa, O. Magnetoencephalography: Theory, instrumentation, and applications to noninvasive studies of the working human brain. *Rev. Mod. Phys.* **65,** 413 (1993).

146. Riaz, B., Pfeiffer, C. & Schneiderman, J. F. Evaluation of realistic layouts for next generation on-scalp MEG: spatial information density maps. *Scientific reports* **7,** 6974 (2017).

147. Beltrachini, L., von Ellenrieder, N., Eichardt, R. & Haueisen, J. Optimal design of on-scalp electromagnetic sensor arrays for brain source localisation. *Human brain mapping* **42,** 4869–4879 (2021).

148. Pratt, E. J. *et al.* Kernel Flux: a whole-head 432-magnetometer optically-pumped magnetoencephalography (OP-MEG) system for brain activity imaging during natural human experiences. *Proc. of SPIE* **11700** (eds Shahriar, S. M. & Scheuer, J.) 162–179 (2021).

149. Clancy, R. J., Gerginov, V., Alem, O., Becker, S. & Knappe, S. A study of scalar optically-pumped magnetometers for use in magnetoencephalography without shielding. *Physics in Medicine & Biology* **66,** 175030 (2021).

150. Knappe, S., Alem, O., Sheng, D. & Kitching, J. *Microfabricated optically-pumped magnetometers for biomagnetic applications* in *Journal of Physics: Conference Series* **723** (2016), 012055.

151. Taulu, S. & Kajola, M. Presentation of electromagnetic multichannel data: the signal space separation method. *Journal of Applied Physics* **97** (2005).

152. Vrba, J. & Robinson, S. SQUID sensor array configurations for magnetoencephalography applications. *Superconductor Science and Technology* **15,** R51 (2002).

153. Handy, T. C. *Event-related potentials: A methods handbook* (MIT press, 2005).

154. Zhao, M., Zhang, K. & Chen, L.-Q. Determination of the atomic density of rubidium-87. *Chinese Physics B* **24,** 094206 (2015).

155. Kemppainen, P. & Ilmoniemi, R. Channel capacity of multichannel magnetometers. *Advances in biomagnetism,* 635–638 (1989).

156. Marhl, U., Sander, T. & Jazbinšek, V. Simulation study of different OPM-MEG measurement components. *Sensors* **22,** 3184 (2022).

157. Sarvas, J. Basic mathematical and electromagnetic concepts of the biomagnetic inverse problem. *Physics in Medicine & Biology* **32,** 11 (1987).

158. Brookes, M. J. *et al.* Optimising experimental design for MEG beamformer imaging. *Neuroimage* **39,** 1788–1802 (2008).

159. Van Veen, B. D., Van Drongelen, W., Yuchtman, M. & Suzuki, A. Localization of brain electrical activity via linearly constrained minimum variance spatial filtering. *IEEE Transactions on biomedical engineering* **44,** 867–880 (1997).

160. Ahonen, A. I. *et al.* 122-channel SQUID instrument for investigating the magnetic signals from the human brain. *Physica Scripta* **1993,** 198 (1993).

161. Oostenveld, R., Fries, P., Maris, E. & Schoffelen, J.-M. FieldTrip: open source software for advanced analysis of MEG, EEG, and invasive electrophysiological data. *Computational intelligence and neuroscience* **2011,** 1–9 (2011).

162. Jaiswal, A. *et al.* Comparison of beamformer implementations for MEG source localization. *NeuroImage* **216,** 116797 (2020).

163. Deserno, M. How to generate equidistributed points on the surface of a sphere. *If Polymerforshung (Ed.)* **99** (2004).

164. Haxby, J. V. *et al.* Distributed and overlapping representations of faces and objects in ventral temporal cortex. *Science* **293,** 2425–2430 (2001).

165. Haynes, J.-D. & Rees, G. Decoding mental states from brain activity in humans. *Nature reviews neuroscience* **7,** 523–534 (2006).

166. Pereira, F., Mitchell, T. & Botvinick, M. Machine learning classifiers and fMRI: a tutorial overview. *Neuroimage* **45,** S199–S209 (2009).

167. Grootswagers, T., Wardle, S. G. & Carlson, T. A. Decoding dynamic brain patterns from evoked responses: a tutorial on multivariate pattern analysis applied to time series neuroimaging data. *Journal of cognitive neuroscience* **29,** 677–697 (2017).

168. Carlson, T. A., Grootswagers, T. & Robinson, A. K. An introduction to time-resolved decoding analysis for M/EEG. *arXiv preprint arXiv:1905.04820* (2019).

169. Kriegeskorte, N. & Kievit, R. A. Representational geometry: integrating cognition, computation, and the brain. *Trends in cognitive sciences* **17,** 401–412 (2013).

170. Guggenmos, M., Sterzer, P. & Cichy, R. M. Multivariate pattern analysis for MEG: A comparison of dissimilarity measures. *Neuroimage* **173,** 434–447 (2018).

171. Kriegeskorte, N., Mur, M. & Bandettini, P. A. Representational similarity analysis-connecting the branches of systems neuroscience. *Frontiers in systems neuroscience,* 4 (2008).

172. Kriegeskorte, N. Relating population-code representations between man, monkey, and computational models. *Frontiers in Neuroscience* **3,** 879 (2009).

173. Diedrichsen, J. & Kriegeskorte, N. Representational models: A common framework for understanding encoding, pattern-component, and representational-similarity analysis. *PLoS computational biology* **13,** e1005508 (2017).

174. Cichy, R. M., Pantazis, D. & Oliva, A. Resolving human object recognition in space and time. *Nature neuroscience* **17,** 455–462 (2014).

175. Proklova, D., Kaiser, D. & Peelen, M. V. Disentangling representations of object shape and object category in human visual cortex: The animate–inanimate distinction. *Journal of cognitive neuroscience* **28,** 680–692 (2016).

176. Cichy, R. M., Khosla, A., Pantazis, D., Torralba, A. & Oliva, A. Comparison of deep neural networks to spatio-temporal cortical dynamics of human visual object recognition reveals hierarchical correspondence. *Scientific reports* **6,** 27755 (2016).

177. Kaplan, J. T., Man, K. & Greening, S. G. Multivariate cross-classification: applying machine learning techniques to characterize abstraction in neural representations. *Frontiers in human neuroscience* **9,** 151 (2015).

178. Dirani, J. & Pylkkänen, L. The Time Course of Cross-Modal Representations of Conceptual Categories. *NeuroImage,* 120254 (2023).

179. Frisby, S. L., Halai, A. D., Cox, C. R., Ralph, M. A. L. & Rogers, T. T. Decoding semantic representations in mind and brain. *Trends in cognitive sciences* (2023).

180. Harrison, S. A. & Tong, F. Decoding reveals the contents of visual working memory in early visual areas. *Nature* **458,** 632–635 (2009).

181. Kornysheva, K. *et al.* Neural competitive queuing of ordinal structure underlies skilled sequential action. *Neuron* **101,** 1166–1180 (2019).

182. Brown, T. I. *et al.* Prospective representation of navigational goals in the human hippocampus. *Science* **352,** 1323–1326 (2016).

183. Ariani, G., Pruszynski, J. A. & Diedrichsen, J. Motor planning brings human primary somatosensory cortex into action-specific preparatory states. *elife* **11,** e69517 (2022).

184. King, J.-R. & Dehaene, S. Characterizing the dynamics of mental representations: the temporal generalization method. *Trends in cognitive sciences* **18,** 203–210 (2014).

185. Vrba, J. & Robinson, S. The effect of environmental noise on magnetometer-and gradiometer-based MEG systems. *Signal* **1,** 0–5 (2001).

186. Iamshchinina, P., Karapetian, A., Kaiser, D. & Cichy, R. M. Resolving the time course of visual and auditory object categorization. *Journal of Neurophysiology* **127,** 1622–1628 (2022).

187. Huth, A. G., Nishimoto, S., Vu, A. T. & Gallant, J. L. A continuous semantic space describes the representation of thousands of object and action categories across the human brain. *Neuron* **76,** 1210–1224 (2012).

188. Konkle, T. & Caramazza, A. Tripartite organization of the ventral stream by animacy and object size. *Journal of Neuroscience* **33,** 10235–10242 (2013).

189. Brainard, D. H. & Vision, S. The psychophysics toolbox. *Spatial vision* **10,** 433–436 (1997).

190. Gramfort, A. *et al.* MEG and EEG data analysis with MNE-Python. *Frontiers in neuroscience,* 267 (2013).

191. Ferrante, O. *et al.* FLUX: A pipeline for MEG analysis. *NeuroImage* **253,** 119047 (2022).

192. Taulu, S. & Simola, J. Spatiotemporal signal space separation method for rejecting nearby interference in MEG measurements. *Physics in Medicine & Biology* **51,** 1759 (2006).

193. Uusitalo, M. A. & Ilmoniemi, R. J. Signal-space projection method for separating MEG or EEG into components. *Medical and biological engineering and computing* **35,** 135–140 (1997).

194. Haumann, N. T., Parkkonen, L., Kliuchko, M., Vuust, P., Brattico, E., *et al.* Comparing the performance of popular MEG/EEG artifact correction methods in an evoked-response study. *Computational intelligence and neuroscience* **2016** (2016).

195. Hyvärinen, A. & Oja, E. Independent component analysis: algorithms and applications. *Neural networks* **13,** 411–430 (2000).

196. Ashton, K. *et al.* Time-resolved multivariate pattern analysis of infant EEG data: A practical tutorial. *Developmental cognitive neuroscience* **54,** 101094 (2022).

197. Chan, A. M., Halgren, E., Marinkovic, K. & Cash, S. S. Decoding word and category-specific spatiotemporal representations from MEG and EEG. *Neuroimage* **54,** 3028–3039 (2011).

198. Tyler, L. K., Cheung, T. P., Devereux, B. J. & Clarke, A. Syntactic computations in the language network: characterizing dynamic network properties using representational similarity analysis. *Frontiers in psychology* **4,** 271 (2013).

199. Cheng, F. Using Single-Trial Representational Similarity Analysis with EEG to track semantic similarity in emotional word processing. *arXiv preprint arXiv:2110.03529* (2021).

200. Cortes, C. & Vapnik, V. Support-vector networks. *Machine learning* **20,** 273–297 (1995).

201. Pedregosa, F. *et al.* Scikit-learn: Machine learning in Python. *Journal of machine learning research* **12,** 2825–2830 (2011).

202. Haufe, S. *et al.* On the interpretation of weight vectors of linear models in multivariate neuroimaging. *Neuroimage* **87,** 96–110 (2014).

203. Garcés, P., López-Sanz, D., Maestú, F. & Pereda, E. Choice of magnetometers and gradiometers after signal space separation. *Sensors* **17,** 2926 (2017).

204. Groen, I. I., Dekker, T. M., Knapen, T. & Silson, E. H. Visuospatial coding as ubiquitous scaffolding for human cognition. *Trends in Cognitive Sciences* **26,** 81–96 (2022).

205. Carlson, T., Tovar, D. A., Alink, A. & Kriegeskorte, N. Representational dynamics of object vision: the first 1000 ms. *Journal of vision* **13,** 1–1 (2013).

206. Kumar, M., Federmeier, K. D., Fei-Fei, L. & Beck, D. M. Evidence for similar patterns of neural activity elicited by picture-and word-based representations of natural scenes. *Neuroimage* **155,** 422–436 (2017).

207. Peelen, M. & Downing, P. Testing cognitive theories using multivariate pattern analysis of neuroimaging data (2022).

208. Giari, G., Leonardelli, E., Tao, Y., Machado, M. & Fairhall, S. L. Spatiotemporal properties of the neural representation of conceptual content for words and pictures–an MEG study. *Neuroimage* **219,** 116913 (2020).

209. Kaiser, D., Azzalini, D. C. & Peelen, M. V. Shape-independent object category responses revealed by MEG and fMRI decoding. *Journal of neurophysiology* **115,** 2246–2250 (2016).

210. Miozzo, M., Pulvermüller, F. & Hauk, O. Early parallel activation of semantics and phonology in picture naming: Evidence from a multiple linear regression MEG study. *Cerebral Cortex* **25,** 3343–3355 (2015).

211. MacGregor, L. J., Pulvermüller, F., Van Casteren, M. & Shtyrov, Y. Ultra-rapid access to words in the brain. *Nature communications* **3,** 711 (2012).

212. Dirani, J. & Pylkkänen, L. Lexical access in naming and reading: spatiotemporal localization of semantic facilitation and interference using MEG. *Neurobiology of Language* **1,** 185–207 (2020).

213. Simanova, I., Van Gerven, M., Oostenveld, R. & Hagoort, P. Identifying object categories from event-related EEG: toward decoding of conceptual representations. *PloS one* **5,** e14465 (2010).

214. Hauk, O., Davis, M. H., Ford, M., Pulvermüller, F. & Marslen-Wilson, W. D. The time course of visual word recognition as revealed by linear regression analysis of ERP data. *Neuroimage* **30,** 1383–1400 (2006).

215. Ralph, M. A. L., Jefferies, E., Patterson, K. & Rogers, T. T. The neural and computational bases of semantic cognition. *Nature reviews neuroscience* **18,** 42–55 (2017).

216. Humphreys, G. F., Hoffman, P., Visser, M., Binney, R. J. & Lambon Ralph, M. A. Establishing task-and modality-dependent dissociations between the semantic and default mode networks. *Proceedings of the National Academy of Sciences* **112,** 7857–7862 (2015).

217. Pobric, G., Jefferies, E. & Ralph, M. A. L. Anterior temporal lobes mediate semantic representation: mimicking semantic dementia by using rTMS in normal participants. *Proceedings of the National Academy of Sciences* **104,** 20137–20141 (2007).

218. Leonardelli, E., Fait, E. & Fairhall, S. L. Temporal dynamics of access to amodal representations of category-level conceptual information. *Scientific reports* **9,** 239 (2019).

219. Hebart, M. N., Bankson, B. B., Harel, A., Baker, C. I. & Cichy, R. M. The representational dynamics of task and object processing in humans. *Elife* **7,** e32816 (2018).

220. Sassenhagen, J. & Draschkow, D. Cluster-based permutation tests of MEG/EEG data do not establish significance of effect latency or location. *Psychophysiology* **56,** e13335 (2019).

221. Maris, E. & Oostenveld, R. Nonparametric statistical testing of EEG-and MEG-data. *Journal of neuroscience methods* **164,** 177–190 (2007).

222. Santi, A., Friederici, A. D., Makuuchi, M. & Grodzinsky, Y. An fMRI study dissociating distance measures computed by Broca's area in movement processing: clause boundary vs. identity. *Frontiers in psychology* **6,** 654 (2015).

223. Federmeier, K. D. Connecting and considering: Electrophysiology provides insights into comprehension. *Psychophysiology* **59,** e13940 (2022).

224. Branzi, F. M., Humphreys, G. F., Hoffman, P. & Ralph, M. A. L. Revealing the neural networks that extract conceptual gestalts from continuously evolving or changing semantic contexts. *NeuroImage* **220,** 116802 (2020).

Appendix A

NMOR OPM - images

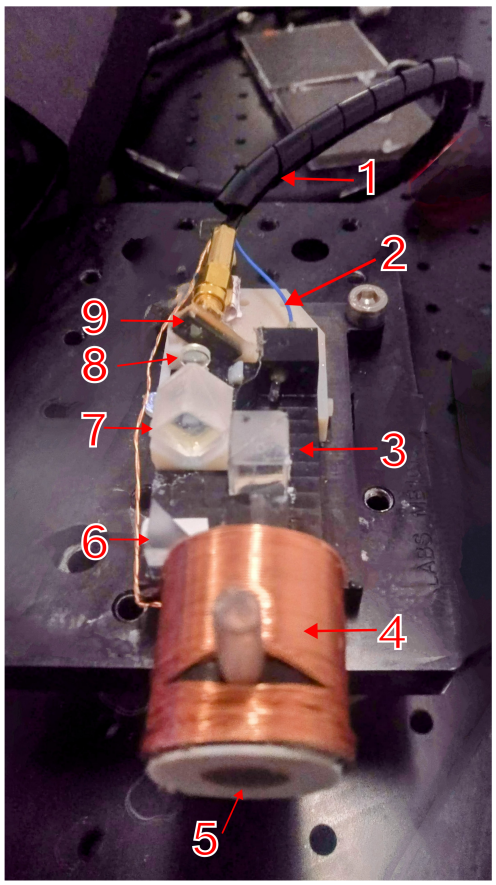

1 - Umbilical cable
2 - Optical fiber
3 - Wollaston prism
4 - Vapoer cell with
solinoid wraped aroung it
5 - Mirror
6 - Mirror
7 - Wollaston prism
8 - Lens
9 - Photodiodes

Figure A.1: Image of the NMOR OPM sensor head described in Chapter 3. 1 - Umbilical cable; 2 - Optical fiber; 3 - Wollaston prism; 4 - Vapour cell with solenoid wrapped around it; 5,6 - Mirror; 7 - Wollaston prism; 8 - Lens; 9 - Photodiodes

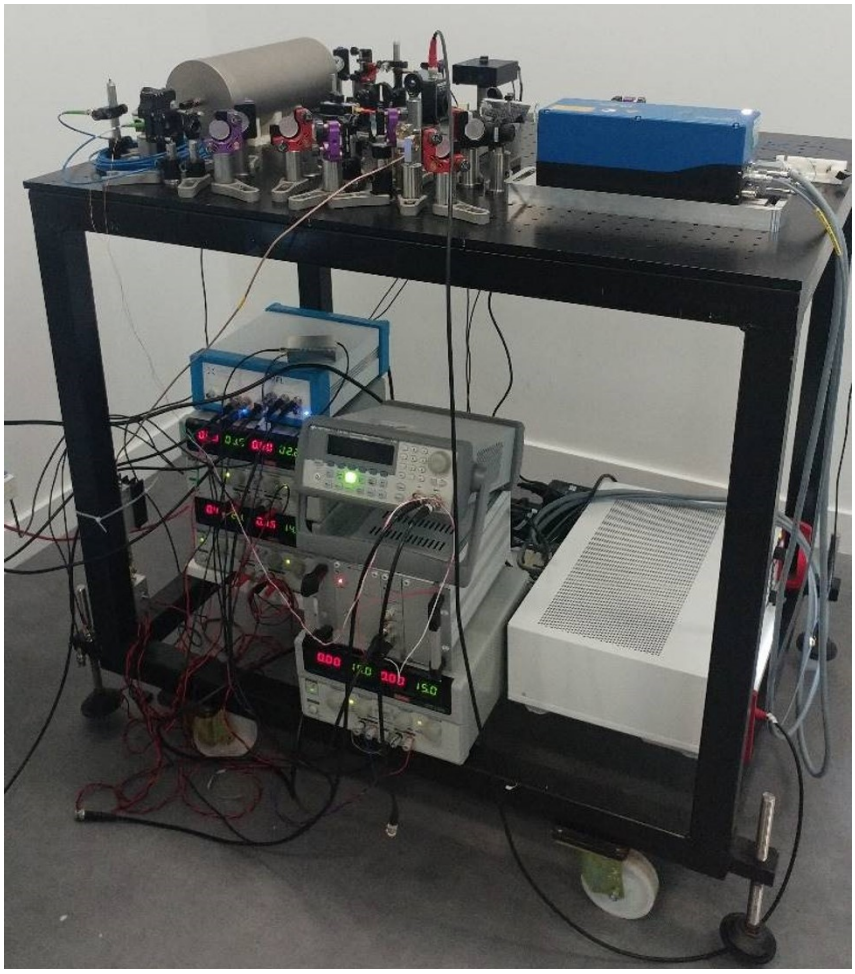

Figure A.2: Image of the NMOR OPM sensor external module described in Chapter 3. All the electronics are located at the bottom of the rack, the optical scheme is located on top of the rack.